Saturation Effects and Thermal Balance in Laser-Cooled Solids

by

Long Cheng

A dissertation submitted in partial fulfillment
of the requirements for the degree of
Doctor of Philosophy
(Electrical and Computer Engineering)
in the University of Michigan
2023

Doctoral Committee:

Professor Stephen C. Rand, Chair
Professor Almantas Galvanauskas
Research Scientist John Nees
Professor Kevin Pipe
Professor David Wehe

Long Cheng
lonche@umich.edu
ORCID iD: 0000-0001-5508-377X

DEDICATION

To my parents
To my wife Yishan

ACKNOWLEDGMENTS

I would like to thank all the people who have guided, supported, and accompanied me during my academic journey at the University of Michigan.

First I would like to thank my advisor Professor Stephen C. Rand, who I feel tremendously lucky to work with. His erudition, scientific understanding, and passion to research have inspired me. He can always come up with great ideas and suggestions to solve the challenges I encountered. He is open to new ideas and allows me to try different approaches. I sincerely appreciate all his guidance and support throughout my doctoral journey.

I would also like to thank Prof. Almantas Galvanauskas, John Nees, Prof. Kevin Pipe, and Prof. David Wehe, for serving on my doctoral committee and for all the constructive feedback they provided. Thank you all for your kind support to my dissertation.

My appreciation goes to my current and former colleagues: Dr. John Whitaker, Laura, Greg, Liz, Theresa, Tuan, Krishnandu, Hengky, Alex, and Ayesheshim. I'd like to thank Laura for all the discussions of ideas and collaborations on the laser cooling project.

I would like to thank our collaborators: Prof. Junior R. Silva, Prof. Luis Andrade and Prof. Sandro Lima from Universidade Estadual de Mato Grosso do Sul for bringing your expertise and supporting our work.

Finally, my deepest thanks to my family. I thank my parents for raising me up with all love and kindness, and for supporting me all the time. Thank my beloved wife Yishan for accompanying the journey of my PhD, and the journey of my life.

TABLE OF CONTENTS

LIST OF FIGURES

FIGURE

LIST OF TABLES

LIST OF ACRONYMS

ASF Anti-Stokes Fluorescence

RBL Radiation-Balanced Laser

RBC Radiation-Balanced Condition

MAT Minimum Achievable Temperature

MFW Mean Fluorescence Wavelength

DLT Differential Luminescence Thermometry

TLS Thermal Lens Spectroscopy

BBR Black-Body Radiation

ABSTRACT

The role of saturation of background absorption by unintended impurities has been investigated for the first time theoretically and experimentally in the context of laser cooling of crystalline solids and the operation of self-cooled or radiation-balanced lasers. In this thesis it is shown that when saturation of the background takes place at an intensity lower than the saturation intensity of dopant ions responsible for cooling, as in Yb^{3+}:$LiYF_4$, cooling efficiency can be improved by using elevated input intensity. With the same input power, the measured cooling efficiency in 10% Yb^{3+}:$LiYF_4$ crystal was doubled at 1020 nm when the beam radius was reduced by a factor of 10, by partially saturating the background impurity absorption. This is effective not only as a post-growth method of enhancing cooling efficiency but offers a new way of reaching lower temperatures than were previously possible with anti-Stokes fluorescent (ASF) refrigeration. Prior to this work, cooling efficiency was thought to be independent of intensity and crystal purification was considered as the only way to improve the cooling efficiency.

It is further demonstrated that background saturation plays a key role in the operation of self-cooled or radiation-balanced lasers. Because radiation-balanced lasers operate under saturated conditions it is essential to include limitations imposed by impurity content of the gain medium. When this is done, quantitative predictions of the required conditions for radiation balance become possible. Laser operation can then be made more efficient and can be extended to new materials which may be relatively impure and uncommon but are well-suited to efficient operation under radiation-balanced conditions by virtue of a special combination of physical characteristics. Radiation-balanced laser operation is achieved in 3% Yb:YAG ($1 \times 1 \times 10$ mm^3) and is found to result in exceptionally uniform temperature distributions using high resolution thermal imagery. Threshold levels, output power, and input power at the radiation balance point are all shown to be in close agreement with theory. This laser achieved 30.5% laser efficiency (agreed with predictions within 2%), which is the highest efficiency level of any self-cooled laser operated to date. Radiation-balanced lasing is also achieved for the first time in the tungstate crystal 2% Yb^{3+}:KYW ($0.9 \times 1.2 \times 10$ cm^3), despite having very high impurity content as the result of being an uncommon gain medium. The achieved laser efficiency was only 2.2%, as the result of non-optimal optical components, high Yb concentration, high impurity content, crystal polish, excitation wavelength, and output coupling. However, this is the first demonstration of an Yb^{3+} radiation-balanced laser

in the tungstate host. Correction of these deficiencies should enable high quality Gaussian output at the 5 W level with 18% efficiency in existing commercial 1% Yb:KYW samples. Even better performance of this new self-cooled laser could result from improved crystal growth efforts.

CHAPTER 1

Introduction

Laser cooling of solids, also called optical refrigeration, is a process by which the thermal energy is removed from a solid material with laser light. The principle of this process is the heat extraction through energy transfer from low entropy incoming light to high entropy outgoing light. Since the laser makes no physical contact with the cooled solid and there are no moving parts, optical refrigeration has the key benefits of being vibration-free, fluid-free, and compact. Thus laser cooling offers advantages for thermal management in many scientific disciplines and technologies.

The primary goal of this thesis was to expand upon the current methodologies of laser cooling of solids and radiation-balanced lasers. New materials and novel techniques to improve upon limitations to cooling and lasing were sought out. The organization of the thesis is outlined in the following paragraphs.

In Chapter 1, an overview of the history of laser cooling of solids is presented. Refrigeration to cryogenic temperatures for the cooling of sensors in space applications and radiation-balanced lasers are noted next. The progress and advances in the field are reported in the last section.

Chapter 2 lays the theoretical foundation for the work presented in this thesis. First, the principles of anti-Stokes fluorescent laser cooling are described. Next, improvements to anti-Stokes fluorescence (ASF) cooling are proposed based on the differing optical saturation of cooling ions and background impurities. Then, the theory of radiation-balanced lasers (RBLs) are detailed. Lastly, the inclusion of the saturable background absorption in current RBL theory is discussed.

Chapter 3 is devoted to the experimental methods utilized in this work. All of the samples studied and the spectroscopic techniques used to measure the absorption and emission spectra of each are presented first. The following section describes the non-contact thermometry methods used in cooling and RBL experiments. Then, the methods of measuring the cooling power and cooling efficiency are presented. The next section introduces the pump locking technique used in RBL experiments, which significantly improves the laser efficiency at radiation-balanced operation. The last section discusses the experimental design of the radiation-balanced laser cavity and laser efficiency for Yb:YAG and Yb:KYW.

The results of cooling experiments are showcased in Chapter 4. The thermal isolation of glass and aerogel supports are explored in the first section. Measurements on Yb:YAG and Yb:KYW are grouped in the next section, and the cooling performance is compared. Next, intensity-dependent measurements in Yb:YLF show an improvement in cooling efficiency through saturation of background impurities. Lastly, radiation-balanced operation in Yb:YAG achieved the highest laser efficiency among all self-cooled laser operated to date and radiation-balanced operation is achieved the first time in the tungstate crystal Yb:KYW.

Finally, Chapter 5 summarizes the significance of the results presented in this thesis. In particular, improvements to the current ASF cooling technique by optical saturation are emphasized and the improvements to the current laser efficiency using the pump locking technique are highlighted. The saturation of background absorption is the only post-growth method for improving ASF cooling performance and is the only experimentally demonstrated theory that includes the background impurity absorption in RBLs. Future directions of this work involving laser cooling to lower minimum achievable temperature and radiation-balanced operation at high power are discussed in the final section.

1.1 History and Background

The idea of laser cooling using anti-Stokes fluorescence was first proposed by Peter Pringsheim in 1929 [1], to cool a fluorescent gas with pumplight of lower photon energy than that of the subsequent fluorescent emission. Disagreement emerged based on entropy, but Landau settled the issue in 1946 [2] by showing that the (fluorescent) light emitted in random directions carries out a much larger entropy than an incident singlemode excitation beam. Subsequently, Kastler suggested that not only gas, but rare-earth ions in the form of solid could be cooled through anti-Stokes fluorescence in 1950 [3]. The invention of the laser in the 1960's with narrow spectral bandwidth and later the purification of materials, especially the development and commercialization of ultra-low-loss high purity glass fibers for long-haul fiber-optic telecommunications, led to the experimental demonstration of optical refrigeration. The first laser cooling of a solid by anti-Stokes fluorescence was observed in 1995 when Epstein achieved a net cooling of 0.3 K below room temperature in Yb^{3+}:ZBLANP glass[4]. Since then, advances in experimental methods and the purification of materials have led to laser cooling in a variety of glasses and crystals doped with ytterbium (Yb^{3+}), thulium (Tm^{3+}), erbium (Er^{3+}), and holmium (Ho^{3+}) which are summarized in Table 1.1. What's more, temperatures in the cryogenic range have been reached [5], the first all-optical cryocooler was demonstrated [6], and radiation-balanced lasers have moved from concept to reality [7, 8, 9, 10]. These advances will be discussed in more details in Section 1.3. Despite the progress that has been made in the field, the purity of laser cooling materials [11] continues to be

a key issue determining cooling efficiency in any given material.

Dopant	Glasses	Crystals
Yb^{3+}	CNBZn [12, 13]	KPC [13, 14]
	BIG [12, 13]	KGW [15, 16]
	ABCYS, $\Delta T = 0.13$ K [17]	YSO, $\Delta T = 1$ K [18]
	Silica, $\Delta T = 6$ K [19]	BYF, $\Delta T = 4$ K [20]
	ZBLAN, $\Delta T = 48$ K [21]	YAG, $\Delta T = 8.9$ K [20]
	ZBLANP, $\Delta T = 92$ K [22]	KYW, $\Delta T = 10$ K [23, 24]
		LLF, $\Delta T = 150$ K [25]
		YLF, $\Delta T = 182$ K [26, 27]
Tm^{3+}	ZBLAN, $\Delta T = 24$ K [28]	YLF, $\Delta T = 14$ K [29]
		BYF, $\Delta T = 23$ K [29]
Tm^{3+}	CNBZn, $\Delta T = 0.5$ K [30]	KPC, $\Delta T = 0.7$ K [30]
Ho^{3+}		KPC, $\Delta T = 3$ K [31]
		BYF, $\Delta T = 3$ K [32]

Table 1.1: Summary of all rare-earth-doped glasses and crystals in which laser-induced cooling has been observed. The maximum temperature drop ΔT reported in the dopant-host combination is given for each material that has shown net cooling. Only local cooling measured by photothermal beam deflection have been reported for the first two rows of hosts for Yb^{3+}.

1.2 Advantages and Applications of Optical Refrigeration

Since optical refrigeration in a solid was achieved in 1995 [4], the main drive for research in this field has been vibration-free cryogenic cooling for space-based technologies [33]. Indeed, laser cooling is the only all-solid-state technique capable of reaching temperatures below 180 K with a fluid-free approach. Hence, its main advantage is the absence of a fluid refrigerant and moving parts, leading to completely vibration-free cooling and a relatively compact device.

The primary alternatives to optical refrigeration are thermoelectric coolers (TECs), which are based on the Peltier effect and mechanical coolers, such as Stirling cycle or pulsed tube technology. There have been a few studies which analyzed the performance of a laser cooler with respect to these other methods [34, 35, 36, 37]. Thermoelectric coolers are only capable of cooling to ~ 180K and mechanical coolers have vibration and reliability issues in present of mechanical systems. Optical refrigerators provide the best solution for applications requiring reliable, vibration-free cooling in the temperature range between 180K and 60K [34].

As mentioned earlier, laser cooling research efforts have largely been focused on space-based technologies. This work is particularly beneficial for the use of infrared (IR) cameras on satellites. The cooled cameras are needed for taking fast or high-resolution images. Satellite-borne systems

put strict constraints on the size, weight, and power usage of on-board instruments. Constraints are even more demanding for micro- and nano-satellites, and increasing any of these parameters can dramatically increase the cost of a mission. Missions can last for many years, and once a satellite has been deployed, repairs to any instrumentation are usually impossible, making high reliability important as well. Based on a specific mission scenario, the analysis in Ref. [37] demonstrated that an optical cooler is more favorable in terms of mass and internal volume than the miniature pulse tube coolers currently used in earth orbit observation satellites. The laser cooler provides less complicated operation (over mechanical coolers), simpler redundant architecture, and is expected to have a similar volume to that of a glass of water. Since the pump laser can be coupled to an optical fiber to power the refrigerator, it has additional flexibility in that the laser control electronics can be placed anywhere on the satellite. Of course, vibration-free cooling is crucial for these cameras which take images over long distances and lengthy exposure times; even small motions can degrade the images. In light of this, completely vibration-less cooling using lasers would be extremely beneficial in overcoming the resolution limitations of current IR cameras [38].

Radiation-balanced lasers (RBLs) have been the next greatest motivation in the field since the first demonstration of optical refrigeration. All lasers generate heat due to the quantum defect and non-radiative decay in the gain medium. This heating leads to thermo-optic distortions which degrade the beam quality, lead to frequency instabilities, broaden the linewidth, and, in the most extreme case, damage the gain medium. This thermal degradation is particularly problematic for high power solid-state lasers. At present time, thin disk lasers and fiber lasers are two solid-state laser technology platforms that can produce a high output power of several kilowatts in a single fundamental Gaussian mode. Thin disk lasers exhibit small thermal distortions due to the small thickness of the disk, which permit rapid thermal transport. The highest output power of thin disk lasers was achieved in 2019, 4 kW with M^2 $<$1.2 [39] (M^2, or beam quality factor, represents the degree of variation of a beam from an ideal Gaussian beam). In addition, a thin-disk laser system consisting of two think-disk laser oscillators and a thin-disk amplifier achieved 10.1 kW output power with M^2 $=$1.76 in 2021 [40]. Fiber lasers have the advantage of reduced thermal distortion because of the large surface to volume ratio. The highest output power of fiber oscillators was achieved in 2021, 6 kW with M^2 $<$1.3 [41]. In addition, an amplified fiber laser system from IPG Photonics delivered 10kW output power in 2009, specified as single mode beam quality. However, the thermal lens in thin disk lasers and the nonlinear effects induced by high intensity (stimulated Raman scattering, stimulated Brillouin scattering, and transverse mode instabilities [42, 43]) in fiber lasers limit the power scaling. The idea to use optical refrigeration via anti-Stokes fluorescence to balance the heat generated by the Stokes-shifted stimulated emission was first proposed by Bowman in 1999 [7]. For radiation-balanced lasers, the thermal lens effect can be eliminated since the heat generated during lasing is compensated by laser refrigeration. What's

more, nonlinear effects are minimized due to the large bulk crystal illuminated by the lights. These advantages make radiation-balanced lasing a promising method to reach high output power with good beam quality.

1.3 Progress and Advances in the Field

After the first experimental demonstration in Yb^{3+}-doped ZBLANP in 1995 [4], a significant milestone was surpassing the $\sim$ 180 K limit of TECs and attaining cooling below the NIST-defined cryogenic temperature of 123 K in Yb:YLF crystal in 2010 [44]. Currently, the lowest temperature ever reported in a solid-state material was achieved in 2019: a 5% Yb:YLF crystal was cooled to 87 K in vacuum [27]. The cooling of highly pure Yb:YLF to cryogenic temperatures paved the way for the first demonstration of an all-solid-state optical cryocooler in 2018 [6], where the HgCdTe sensor of a working Fourier Transform Infrared spectrometer was cooled to 135 K.

In the domain of radiation-balanced lasers (RBLs), shortly after the idea was first proposed in 1999 [7], Bowman also investigated new materials for optical cooling and evaluated their performance for use as RBLs [15]. A figure of merit was defined for predicting radiation-balanced lasing performance by optimizing optical efficiency and laser gain to choose appropriate pump and lasing wavelengths. It was found that the Yb-doped tungstate crystals of $KGd(WO_4)_2$ (KGW) and $KY(WO_4)_2$ (KYW) had by far the highest figure of merits. Bowman demonstrated the first RBL in 2010 using a Yb:YAG rod [8]. An output power of 200 W with a beam quality of M^2 = 1.2 and 26% optical conversion efficiency was achieved. Only two other reports of RBLs have been published since that time - a Yb:YAG disk laser in 2019 [9] and a Yb-doped silica fiber laser in 2021 [10].

Despite many advances in the field, the purity of laser cooling materials [11] continues to be a key issue determining cooling efficiency in any given material. Unintended impurities can absorb pump light or fluorescence, causing heating rather than cooling. To date, the theory of laser cooling has assumed that impurity absorption is a fixed property of a sample once it is grown. Consequently, it has been thought that the only way to improve cooling efficiency was through sample purification. However, this overlooks the possibility that background impurity absorption could be intensity-dependent in a beneficial way.

Also, any limitations from background impurity absorption in laser cooling were assumed to be negligible in the original RBL theory of Bowman. Efforts were made in the past to include parasitic heating in the RBL heat equation [8, 9]. Unfortunately, these inclusions were found to eliminate theoretical solutions for radiation-balance in well-characterized materials that have been operated as RBLs in the lab [45, 46]. As summarized in this Section 2.4, this problem originates from the neglect of saturation effects at the elevated light intensities that circulate inside RBL lasers.

This thesis presents the first observation of background absorption saturation in anti-Stokes fluorescence cooling and demonstrates that under certain conditions this effect can improve the cooling efficiency near room temperature at high pump intensities. Furthermore, an extension of the existing RBL theory to include saturable parasitic heating is proposed which alters the predicted radiation-balance condition significantly. Experimentally it is demonstrated that good agreement can be achieved between the radiation-balanced laser operation in Yb:YAG and Yb:KYW and theoretical predictions which carefully take the role of background impurities into account.

CHAPTER 2

Theory

This chapter outlines the relevant theory related to the work presented in this thesis, and is broken down into four sections as follows. Section 2.1 introduces the process of laser cooling by anti-Stokes fluorescence (ASF) and the associated cooling efficiency. Section 2.2 develops a two-level model for the cooling process and predicts an improvement to the Anti-Stokes Fluorescence (ASF) cooling via optical saturation of background absorption. The current RBL theory based on the two-level model, where background absorption is ignored, and the radiation-balance condition (RBC) are introduced in Section 2.3. It is then argued that background absorption plays a critical role in quantitative predictions of the RBC. Consequently, this chapter ends by presenting a corrected version of RBL theory in Section 2.4, where saturable background absorption is included and shown to alter predicted conditions for radiation-balance significantly.

2.1 Laser Cooling of Solids

The possibility that an object might cool through the ASF process was suggested by Pringsheim in 1929 [1]. For a two-level system with broad ground- and excited-state manifolds (Fig. 2.1), the photons of a pump laser detuned to the "red" (low energy) side of a transition resonance can excite atoms from thermally populated sublevels near the top of the ground state manifold to the bottom of the excited state manifold. Excited atoms then reach thermal equilibrium by absorbing vibrational phonon energy while in the upper state. After acquiring this extra energy from the lattice, excited dopant atoms return to the ground state manifold through spontaneous emission with an emitted photon energy that is higher on average than that of the absorbed photon. Hence, this ASF process reduces the thermal energy of the solid as a whole and leads to refrigeration.

In the following sub-sections, laser cooling of Yb^{3+}-doped materials will be considered in detail. The mean value of emitted photon energy of ASF will be determined and its importance in laser cooling emphasized. Finally, the thermal energy removed by laser refrigeration will be analyzed to derive the cooling power and cooling efficiency.

2.1.1 Anti-Stokes Fluorescence for Yb^{3+} Ions

As mentioned earlier in Section 2.1, ASF cooling involves electronic transitions between ground state and excited state manifolds. In this section, the energy levels of rare-earth-doped materials are introduced and a detailed picture of the ASF cooling process is presented. While the process is outlined for Yb^{3+}-doped materials in general, some details of Yb:KYW will be highlighted.

The un-ionized Ytterbium (Yb, $[Xe]4f^{14}6s^2$) atom has filled outer shells $4f^{14}$ and $6s^2$. When bonding with fluorine (Yb:YLF) or oxygen (Yb:KYW and Yb:YAG) atoms, the Yb atom gives up two $6s^2$ and one of the $4f^{14}$ electrons, leaving a single unoccupied electronic state in the 4f shell, forming the well-known $^2F_{7/2}$ ground state manifold and $^2F_{5/2}$ excited state manifold of the trivalent ion. The crystal field created by the neighboring ions of the host material splits the $(2J+1)$-fold degeneracy of each manifold, leading to $(2J+1)/2$ sub-levels via Stark effect [47]. The remaining factor of 2 in degeneracy is due to Kramers theorem [48], which states that every energy level is at least doubly degenerate if it has half-integer spin. Fig. 2.1 plots the energy levels of trivalent ytterbium (Yb^{3+}, $[Xe]4f^{13}$) in potassium yttrium tungstate (KYW, $KY(WO_4)_2$) crystals [49]. The $^2F_{7/2}$ ground state and $^2F_{5/2}$ excited state manifolds contain 4 and 3 sub-levels, respectively. With this information on the detailed energy levels of Yb^{3+}-doped crystals in hand, the cooling cycle of ASF can now be analyzed.

The forbidden transition between $^2F_{5/2}$ and $^2F_{7/2}$ leads to a long-lived excited state ($\sim$ milliseconds), while the thermalization between sub-levels in each of the manifolds is rapid ($\sim$ picoseconds). During a cooling cycle, the pump, tuned to the low energy side of the absorption peak, lifts the electron from the top of ground state to the bottom of excited state. Excited electrons quickly absorb vibrational energy from the lattice to reach higher sub-levels of the excited state in accord with the Boltzmann distribution. These electrons then decay to the ground state radiatively through 12 different channels, and the average photon energy of fluorescence can be calculated based on the transition strength of each channel. Similar to the excited state, the electrons in different sub-levels of the ground state absorb phonon energy to reach upper sub-levels of the manifold, compensating for the electron depletion caused by the red-detuned pump, thereby maintaining the Boltzmann distribution. Hence, provided the output optical field has higher entropy than the input field, phonon energy is extracted from the crystal radiatively and the temperature of the material decreases. The energy leaving the material is calculated in Section 2.1.2 based on the fluorescence spectrum of the dopant and the cooling power and efficiency are derived in Section 2.1.3.

2.1.2 Mean Fluorescence Wavelength

As presented in Section 2.1.1, energy is removed from Yb-doped materials via radiative decay through 12 different channels. The following analysis shows that emitted energy can nevertheless

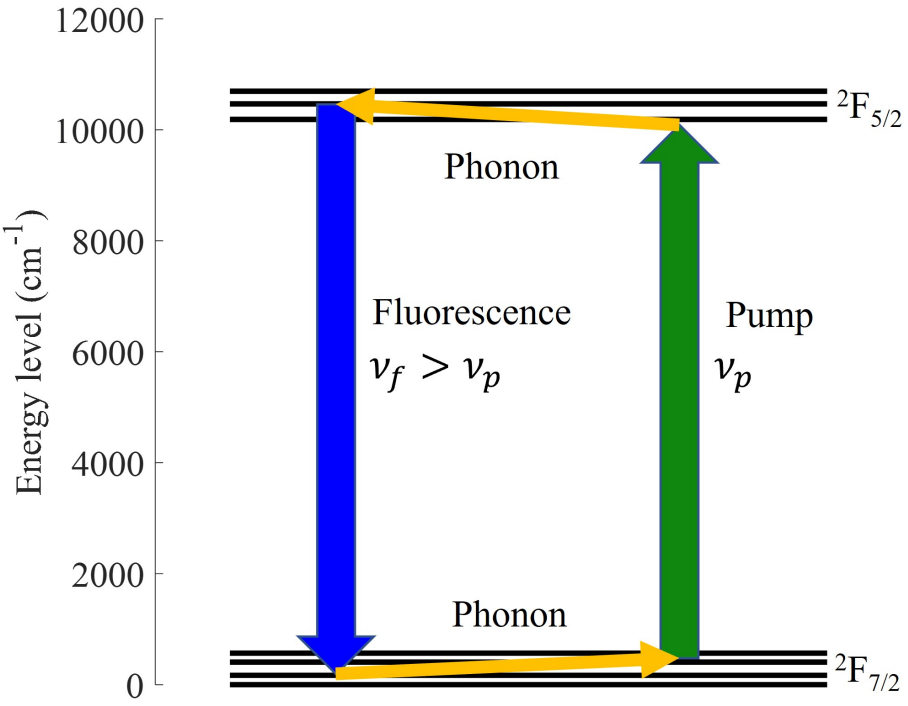

Figure 2.1: Energy levels of Yb:KYW. The emitted fluorescent photon, blue arrow, is more energetic than the absorbed photon, green arrow. The yellow arrows show the phonon-related thermalization process.

be characterized by only a single parameter, namely the mean fluorescence wavelength (MFW).

In ASF cooling, energy leaves the solid through fluorescence, which is equal to the sum of emitted photon energies propagating in all directions. The mean emitted photon energy, $h\nu_f$, is equal to the ratio of emitted photon energies to emitted photon number,

$$h\nu_f = \frac{\sum_{\hat{k},\hat{\sigma}} n(\hat{k},\hat{\sigma}) h\nu}{\sum_{\hat{k},\hat{\sigma}} n(\hat{k},\hat{\sigma})} = \frac{hc}{\lambda_f}, \tag{2.1}$$

where $\hat{k}$, $\hat{\sigma}$ are the wave vector and polarization of emitted photons. The emitted photon number n depends on propagation direction, frequency, and polarization. The Mean Fluorescence Wavelength (MFW) λ_f can be calculated by

$$\lambda_f = \frac{\sum_i \int n_i(\lambda) d\lambda}{\sum_i \int n_i(\lambda) \frac{1}{\lambda} d\lambda} = \frac{\sum_i \int \lambda S_i(\lambda) d\lambda}{\sum_i \int S_i(\lambda) d\lambda}, \tag{2.2}$$

where $S_i(\lambda)$ is the emission spectral density, which equals $\frac{hc}{\lambda} n_i(\lambda)$. The quantum mechanical

summation over wavenumber and polarization $\hat{k}$, $\hat{\sigma}$ in Eq. (2.1) is converted to the experimentally measurable sum of wavelength integrals for the three orthogonal polarizations labeled by index i. Whether the signal from the experimental spectrometer is based on counts n or on intensity $S_i(\lambda)$, the MFW can be calculated from the measured emission spectra at three orthogonal polarizations with Eq. (2.2). Since the mean fluorescence wavelength is an important thermodynamic characteristic of the overall emitted field, it plays a key role in determining the cooling efficiency and cooling power, which are derived next.

2.1.3 Cooling Power and Cooling Efficiency

The cooling power P_c per unit volume is calculated by subtracting the power absorbed by coolant ions and background impurities from the emitted power. This yields

$$\frac{P_c(\lambda)}{V} = \eta_e \eta_{qe} \alpha_r(\lambda) I_0 \frac{\lambda}{\lambda_f} - \alpha_r(\lambda) I_0 - \alpha_b I_0, \tag{2.3}$$

where α_r and α_b are the absorption coefficients of cooling ions and background impurities, respectively. η_{qe} is the internal quantum efficiency. The fluorescence escape efficiency η_e is defined as the ratio of escaped photon number to fluorescent photon number, which is related to the crystal geometry and re-absorption. The first term on the right hand side of Eq. (2.3) is the power density emitted by the crystal, while the last two terms are the power density absorbed by the crystal.

The ASF cooling efficiency is defined as the ratio of cooling power to absorbed power P_{abs}. Hence, it is given by the expression

$$\eta_c = \frac{P_c}{P_{abs}} = \eta_{EQE} \eta_{abs} \frac{\lambda}{\lambda_f} - 1 \tag{2.4}$$

where the external quantum efficiency η_{EQE} is the ratio of escaped photon number to absorbed photon number. This quantity is defined as $\eta_{EQE} = \eta_e \eta_{qe}$. The second factor in Eq. (2.4), namely η_{abs}, is the absorption efficiency given by

$$\eta_{abs} = \frac{\alpha_r(\lambda)}{\alpha_r(\lambda) + \alpha_b}. \tag{2.5}$$

This quantity specifies how much of the power is absorbed by the cooling ions rather than background impurities.

Eq. (2.4) shows the parameters that affect the cooling efficiency and indicates possibilities for maximizing the cooling efficiency. By way of illustration, the cooling efficiency can be enhanced by increasing the external quantum efficiency, absorption efficiency, and pump wavelength or by decreasing the MFW. However, most of the parameters are related. For example, although increas-

ing the doping density of the coolant ion will increase the absorption efficiency, it also decreases the escape efficiency and MFW through fluorescence re-absorption. Hence, evaluations of the trade-offs in these parameters are important to determine how to maximize the cooling efficiency. However, among the relevant parameters, the background absorption coefficient contributes purely to heating and significantly limits the achievable temperature with ASF cooling [34]. The following section will introduce an improvement to ASF cooling which can be realized by reducing the background absorption through optical saturation.

2.2 Saturation in Laser Cooling

As presented in the previous section, the absorption of light by cooling ions and background impurities strongly affects the efficiency of laser cooling by the ASF method, but in opposite ways. At appropriate pump wavelengths, coolant ions with high radiative efficiency contribute to cooling by emitting at a wavelength shorter than that of the absorbed photons on average. Absorption by other impurities causes heating because their transitions are not part of the pump-driven cooling cycle, but rather typically undergo some non-radiative processes that generate heat. In this section, the difference between coolant and background absorption (differential absorption) is analyzed as a function of intensity to reveal that the heatload can be reduced and a lower achievable temperature can be reached in materials where the background impurity absorption saturates at a lower intensity than the cooling ions.

2.2.1 Differential Absorption Saturation

In Section 2.1.3, the expression for cooling efficiency η_c was derived, but the possible dependence of background absorption on intensity was ignored. In this section, the coolant ions and the background impurities will both be modeled as 2-level systems [45, 50, 51] to analyze the theoretical dependence of cooling efficiency on pump light intensity.

The ground and excited state population densities (population per unit volume) of the active ions and background impurities are denoted by N_1, N_2 and N_1', N_2', respectively. Their total densities are therefore given by the sums

$$N_T = N_1 + N_2 \tag{2.6}$$

$$N_T' = N_1' + N_2'. \tag{2.7}$$

The rate equation for the upper state population of the active ion is

$$\frac{dN_2}{dt} = \frac{I_p \lambda_p}{hc} \left[\sigma_a(\lambda_p, T) N_1 - \sigma_e(\lambda_p, T) N_2\right] - \frac{N_2}{\tau_r} - \gamma_{nr} N_2, \tag{2.8}$$

where σ_a and σ_e are the effective absorption and emission cross sections which can be measured directly from instrumentally-corrected optical spectra. These effective cross sections include effects of the Boltzmann distribution and are therefore temperature dependent. τ_r is the radiative lifetime of the active ion. By introducing the fluorescence lifetime, τ_f, which is the inverse sum of the radiative and non-radiative decay rates γ_r and γ_{nr}, the rate equation for the active ion simplifies to:

$$\frac{dN_2}{dt} = \frac{I_p \lambda_p}{hc} \left[\sigma_a(\lambda_p, T)N_1 - \sigma_e(\lambda_p, T)N_2\right] - \frac{N_2}{\tau_f}. \tag{2.9}$$

For the background impurities, primes denote corresponding parameters, and the equation for upper state population is

$$\frac{dN_2'}{dt} = \frac{I_p \lambda_p}{hc} \left[\sigma_a'(\lambda_p, T)N_1' - \sigma_e'(\lambda_p, T)N_2'\right] - \frac{N_2'}{\tau_f'}. \tag{2.10}$$

The net thermal power density H deposited in the medium by incident light fields includes the power density absorbed from the pump as well as that released by radiative and non-radiative relaxation processes. In the calculation of H, the escape efficiency η_e and the internal quantum efficiency $\eta_{QE} = \tau_f/\tau_r$ of active ion fluorescence are taken into account, and background impurities are presumed to contribute only via absorption. Hence H consists of two terms describing net absorption and fluorescent emission by the active ions plus a term for the net absorption by background impurities.

$$H = I_p \left[\sigma_a(\lambda_p, T)N_1 - \sigma_e(\lambda_p, T)N_2\right] - \eta_e \frac{hc}{\lambda_f}\frac{N_2}{\tau_r} + I_p \left[\sigma_a'(\lambda_p, T)N_1' - \sigma_e'(\lambda_p, T)N_2'\right] \tag{2.11}$$

Under steady-state conditions, the level populations have no time dependence. By solving Eq. (2.9) and Eq. (2.10) in this limit, the intensity dependence of the absorption coefficients for the coolant ions and background impurities, respectively, are found to be

$$\alpha_r(I) = \sigma_a(\lambda_p, T)\left[N_1 - \frac{\sigma_e(\lambda_p, T)}{\sigma_a(\lambda_p, T)}N_2\right] = \frac{\alpha_r(0)}{\frac{I_p}{I_r} + 1} \tag{2.12}$$

and

$$\alpha_b(I) = \sigma_a'(\lambda_p, T)\left[N_1' - \frac{\sigma_e'(\lambda_p, T)}{\sigma_a'(\lambda_p, T)}N_2'\right] = \frac{\alpha_b(0)}{\frac{I_p}{I_{sat}'} + 1}, \tag{2.13}$$

where I_r and I_b are the saturation intensities for coolant ions and background impurities, given by

$$I_r = \frac{hc}{\lambda_p \tau_f \left[\sigma_a\left(\lambda_p, T\right) + \sigma_e\left(\lambda_p, T\right)\right]} \tag{2.14}$$

and

$$I_b = \frac{hc}{\lambda_p \tau_f' \left[\sigma_a'\left(\lambda_p, T\right) + \sigma_e'\left(\lambda_p, T\right)\right]}. \tag{2.15}$$

The heat equation can now be written in a form that accounts for saturation effects and non-radiative decay:

$$H = I_p \left[\alpha_r(I) + \alpha_b(I)\right] \left[1 - \eta_{EQE}\eta_{abs}\frac{\lambda_p}{\lambda_f}\right], \tag{2.16}$$

where the intensity-dependent absorption efficiency is

$$\eta_{abs} = \frac{\alpha_r(I)}{\alpha_r(I) + \alpha_b(I)}. \tag{2.17}$$

The final expression for cooling power in the presence of optical saturation of active ions and background impurities is therefore

$$P_c = -P_{abs}\left[1 - \eta_{EQE}\eta_{abs}\frac{\lambda_p}{\lambda_f}\right]. \tag{2.18}$$

Finally, the intensity-dependent cooling efficiency η_c is

$$\eta_c = \frac{P_c}{P_{abs}} = \eta_{EQE}\eta_{abs}\frac{\lambda}{\lambda_f} - 1, \tag{2.19}$$

which is exactly the same with Eq. (2.4), modified to include the intensity-dependent absorption coefficient. Next, the cooling efficiency at different intensities will be considered to show that ASF cooling improves under some conditions when optical saturation is taken into account.

2.2.2 Improved Cooling Efficiency using Optical Saturation

In the previous section, the intensity-dependent cooling efficiency was derived based on the two-level model. Here, the cooling efficiency at different intensities is analyzed to show that the heat-load can be reduced by optical saturation of background absorption.

Fig. 2.2a displays examples of optical spectra from which both the effective cross sections for the 10% Yb^{3+}:$YLiF_4$ crystal studied in our experiments and the mean fluorescence wavelength of 997.6 nm can be derived. Together with a Yb^{3+} fluorescence lifetime of 2.2 ms [52] in this host, these quantities determine the theoretical saturation intensity of Yb^{3+} coolant ions which is plotted versus wavelength in Figure 2.2b using Eq. (2.14).

Surmising that Fe^{3+} is the main background impurity species [53] with a broadband spectrum centered around 1 micron [54], the saturation intensity I_b would be only weakly wavelength-dependent over the range of our experiments, unlike I_r which varies strongly with detuning. Under

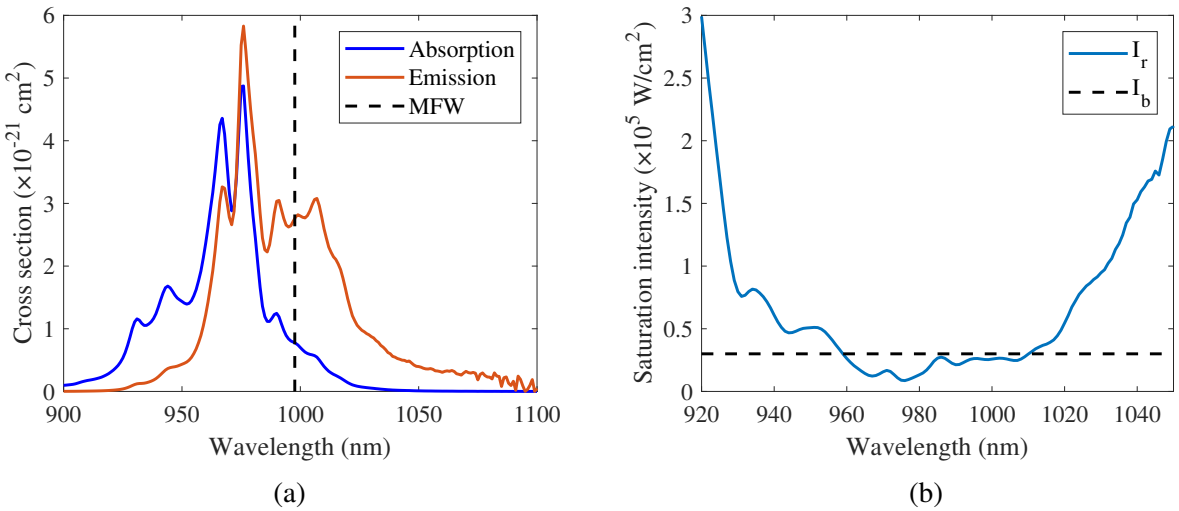

(a) (b)

Figure 2.2: (a) Polarized absorption and emission cross sections of Yb:YLF_4. Both spectra were recorded for E parallel to the 5.1 mm edge of the sample (see Appendix A for the precise orientation of crystal axes). The experimental absorption cross section (blue) was measured with a spectrophotometer. The effective emission cross section was calculated from McCumber theory. As indicated by the dashed line, the polarization-averaged mean fluorescence wavelength was 997.6 nm. (b) Saturation intensities of Yb^{3+} and background absorption are calculated from Eq. (2.14), illustrating different wavelength dependencies. The solid curve (blue) is the saturation intensity I_r of Yb^{3+} while the dashed curve is I_b for background impurities exhibiting an intersection point at $\lambda_{cr} = 1010$ nm on the low energy side of the Yb^{3+} absorption band, where $I_b = I_r(\lambda_{cr}) = 3 \times 10^4$ W/cm^2.

these circumstances, an experimental estimate of I_b can be determined, which is illustrated as the dashed line in Figure 2.2b.

A plot of cooling efficiencies calculated from Eq. (2.19) using the two intensities $I = 3 \times 10^2$ W/cm^2 and $I = 3 \times 10^4$ W/cm^2 is shown in Figure 2.3. At long wavelengths (>1 μm), the cooling efficiency is seen to increase at higher pump intensity. This unusual intensity dependence is readily explained by the background impurities being easier to saturate than coolant ions at large detunings from the Yb^{3+} absorption resonance displayed in Fig. 2.2a. In this range, saturation of background absorption reduces the heatload from impurities relative to the cooling from Yb^{3+} ions, provided $I_b < I_c$. On the other hand, at wavelengths less than ∼1 μm, close to the absorption resonances of Yb^{3+}, the saturation intensity of the coolant ions is lowered by the small detuning and eventually drops below that of the background ($I_c < I_b$). The result is a heightened heatload and reduced cooling efficiency at short wavelengths. Between these opposing limits, there exists an intersection of saturation intensity curves versus wavelength (Fig. 2.2b) on the low energy side of the Yb^{3+} resonance.

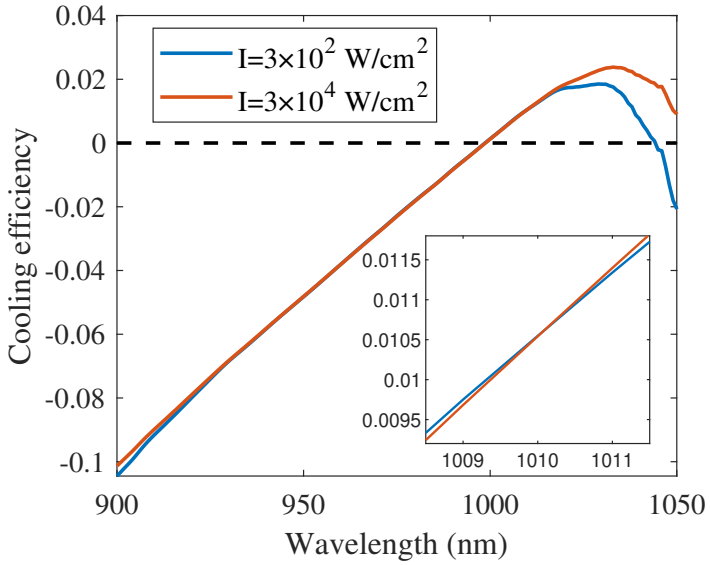

Figure 2.3: Cooling efficiency from Eq. (2.19) versus wavelength at pump intensities differing by two orders of magnitude. Cooling efficiency curves predicted at high and low intensity (red and blue respectively) on the low energy side of 1010 nm where the intersection occurs. A background saturation intensity of 3×10^4 W/cm^2 was estimated from the wavelength $\lambda_{cr} = 1010$ nm of the crossing point (see inset) using Eq. (2.14). Note that in the cooling range, the high intensity cooling efficiency exceeds the low intensity value. For this simulation, the external quantum efficiency was $\eta_{EQE} = 1$ and $\alpha_b(0) = 1 \times 10^{-3}$ cm^{-1}.

While less obvious in Figure 2.3, the same intersection takes place for curves of cooling efficiency at approximately 1010 nm. This intersection point identifies a wavelength λ_{cr} at which the saturation intensities (as well as the cooling efficiencies) of coolant and background ions are equal ($I_c = I_b$). It is important to recognize that the cooling efficiency is independent of intensity at the intersection point. For the curves to cross, the saturation intensities of coolant and background ion must be equal at λ_{cr}, i.e. $I_b = I_r(\lambda_{cr})$. Consequently the denominators in Eqs. (2.12) and (2.13) are the same and cancel in the expression for cooling efficiency. At this intersection point, the saturation intensity of the background can also be determined even when the nature or properties of the background impurities is unknown because it must equal that of the coolant ions. The saturation intensity of background impurities is therefore found by simply inserting λ_{cr} into Eq. (2.14) to find $I_b = I_r(\lambda_{cr})$.

2.2.3 Lower Minimum Achievable Temperature via Background Saturation

The intensity dependence of absorption for cooling ions and impurities theoretically affects the minimum achievable temperature (MAT) in ASF cooling. Figure 2.3 in the previous section

showed an improved cooling efficiency with optical saturation of background absorption at long wavelengths in the case where background impurities saturate at a lower intensity than coolant ions. In this section, the expression for MAT is derived, and it is shown that a lower Minimum Achievable Temperature (MAT) could also be achieved under these conditions.

The phonon sideband absorption is proportional to the average phonon occupation denoted by

$$\langle n(T)\rangle = \left[\exp\left(\frac{\hbar\Omega}{k_B T}\right) - 1\right]^{-1}. \tag{2.20}$$

Hence, the temperature-dependent absorption coefficient of active ions is

$$\alpha_r(T) = \frac{\langle n(T)\rangle}{\langle n(T_0)\rangle}\alpha_r(T_0). \tag{2.21}$$

The effect of saturation on MAT can be analyzed by setting the usual expression for cooling efficiency, Eq. (2.19), equal to zero and solving for temperature with the approximation $\hbar\Omega = h\left(\nu_f - \nu\right) \approx\ k_B T$. The resulting expression for MAT is

$$T_{min} = \hbar\Omega / \left(k_B \log_e\left\{1 + \left(\eta_{EQE}\frac{\lambda}{\lambda_f} - 1\right)\frac{\alpha_r\left(I\right)}{\alpha_b\left(I\right)}\left[\exp\left(\frac{\hbar\Omega}{k_B T_0}\right) - 1\right]\right\}\right). \tag{2.22}$$

In figure 2.4, the saturation intensity depends on wavelength, and its value is calculated using the Yb^{3+} fluorescence lifetime and cross sections in Eq. (2.14). The background saturation intensity was assigned the experimentally measured value (see Section 4.3). Room temperature absorption spectra were also used to prepare the plots, which illustrate important aspects of saturation behavior. Figure 2.4b plots values of T_{min} versus assumed ratios of background and coolant ion saturation intensities and versus wavelength in Yb^{3+}:$LiYF_4$. Note that in Fig. 2.4b if $I_b \gg I_r$, the cooling power saturates before the background heating and no benefit is realized at high pump intensities. When $I_b = I_r$, there is no dependence of net cooling on intensity at all. However, if $I_b < I_r$, the MAT drops substantially with increasing pump intensity. Considering only the temperature dependence of phonon sideband absorption in Yb^{3+}:$LiYF_4$, the curves in Figure 2.4a therefore show theoretically that if the ratio of saturation intensities were $I_r/I_b = 1.58$ as in the experiment, the MAT would drop from roughly 120 K to 100 K in this material by exploiting saturation.

2.3 Radiation-Balanced Lasers

RBLs were first proposed by Bowman in 1999 [7] in which the heat generated during lasing can be compensated by ASF cooling. When the cooling power is exactly equal to the heating power in

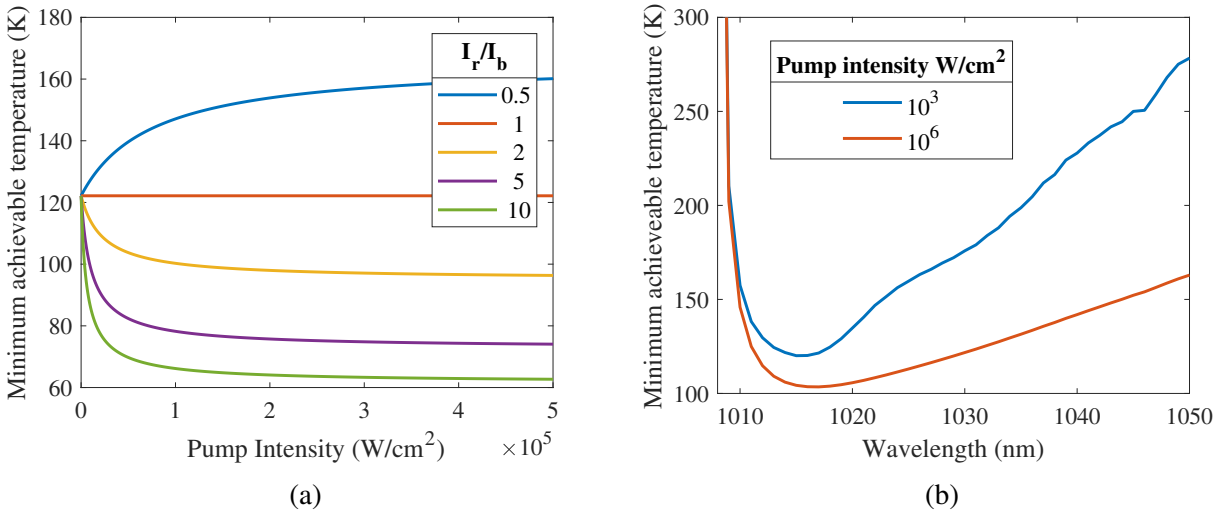

Figure 2.4: (a) Theoretical MAT values at 1017 nm from Eq. (2.22) versus pump intensity for different ratios of coolant to background saturation intensities in 10% Yb^{3+}:$LiYF_4$. The Yb^{3+} saturation intensity was fixed at $I_r = 4.1 \times 10^4$ W/cm^2 (at 1017 nm) and the background value was varied to illustrate different cases. The unsaturated absorption coefficient of coolant ions was 0.296 cm^{-1} at 1017 nm (experimental). (b) Theoretical MAT curves versus wavelength using the experimentally-determined ratio $I_r/I_b = 1.58$ at pump intensities of 10^3 W/cm^2 (blue) and 10^6 W/cm^2 (red). The saturation intensities of Yb^{3+} and background were $I_r = 4.1 \times 10^4$ W/cm^2 (at 1017 nm) and $I_b = 2.6 \times 10^4$ W/cm^2 in the simulation. The mean fluorescence wavelength was $\lambda_{MFW} = 997.6$ nm, the external quantum efficiency was taken to be $\eta_{ext} = 0.99$, and the background absorption coefficient was $\alpha_b = 5 \times 10^{-4}$ cm^{-1} for both plots.

the laser material, the phonon energy generated by the lasing cycle will be absorbed by the cooling cycle, and the net thermal power inside the laser medium is zero, leading to a constant temperature of the gain medium during lasing. Since thermal effects are absent in the laser medium, the output laser light is able to reach a high power with a good beam quality. Fig. 2.5 plots the energy levels of Yb:KYW with the vertical arrows indicating stimulated (red) and spontaneous (blue) transitions in the laser medium. The lasing cycle lifts electrons from the second highest sub-level of the ground state to the lowest sub-level of the excited state, establishing population inversion between top of the ground-state manifold and bottom of the excited-state manifold. This leads to gain inside the medium and amplification of laser light circulating within the laser cavity. In this section, the thermal energy in the laser medium is analyzed to reveal the condition required to reach thermal balance.

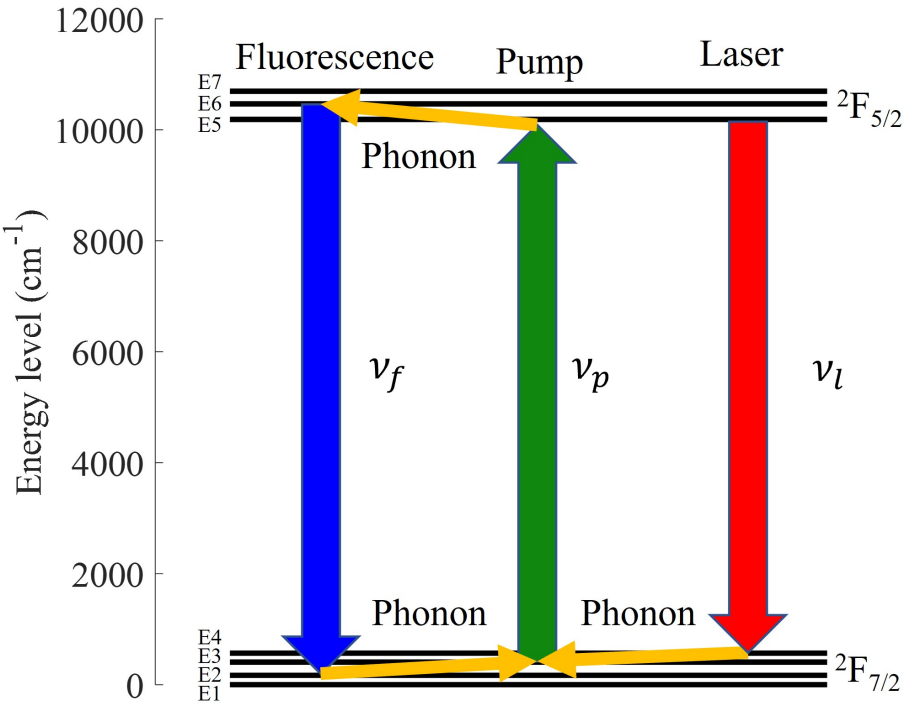

Figure 2.5: Energy levels of Yb:KYW crystal. The left cycle is the cooling cycle which absorbs phonons and the right cycle is the lasing cycle which generates phonons. For RBLs, the generated phonon energy is equal to the absorbed phonon energy.

2.3.1 Radiation-Balanced Condition

In this section, the thermal load within the laser medium is analyzed using a two-level model to reveal the requirement for reaching the radiation balance condition (RBC). Figure 2.5 shows the mechanism of radiation-balanced lasing. For a laser medium to operate at the point of radiation balance, the pump and laser intensities inside the medium need to be specifically designed to ensure that the heat generated during lasing is exactly equal to the heat absorbed by ASF, so the net thermal power inside the medium is exactly zero. In this section, the RBL is analyzed as a two-level system to derive the RBC in the absence of background absorption [45]. The effects of background absorption will be treated in a later section.

Similar to Eq. (2.9), the excited-state population in the presence of combined pump and laser light fields is

$$\frac{dN_2}{dt} = \frac{I_p\lambda_p}{hc}\left[\sigma_a(\lambda_p,T)N_1 - \sigma_e(\lambda_p,T)N_2\right] + \frac{I_l\lambda_l}{hc}\left[\sigma_a(\lambda_l,T)N_1 - \sigma_e(\lambda_l,T)N_2\right] - \frac{N_2}{\tau_f}. \quad (2.23)$$

where I_p and I_l denote pump (p) and laser (l) intensities at wavelengths of λ_p and λ_l. By solving Eq. (2.23) under steady-state conditions, the absorption coefficients at the pump and laser wavelengths are found to be

$$\alpha_p(I_p, I_l) = \sigma_a(\lambda_p, T)\left[N_1 - \frac{\sigma_e(\lambda_p, T)}{\sigma_a(\lambda_p, T)}N_2\right] = \alpha_p(0,0)\frac{\frac{\beta_l I_l}{\beta_{pl} I_{sat,l}} + 1}{\frac{I_p}{I_{sat,p}} + \frac{I_l}{I_{sat,l}} + 1}, \tag{2.24}$$

$$\alpha_l(I_p, I_l) = \sigma_a(\lambda_l, T)\left[N_1 - \frac{\sigma_e(\lambda_l, T)}{\sigma_a(\lambda_l, T)}N_2\right] = \alpha_l(0,0)\frac{-\frac{\beta_p I_p}{\beta_{pl} I_{sat,p}} + 1}{\frac{I_p}{I_{sat,p}} + \frac{I_l}{I_{sat,l}} + 1}. \tag{2.25}$$

These expressions have been simplified by introducing saturation intensities for the pump and laser fields defined respectively by

$$I_{sat,p} \equiv \frac{hc}{\lambda_p \tau_f \left[\sigma_a(\lambda_p, T) + \sigma_e(\lambda_p, T)\right]} \tag{2.26}$$

and

$$I_{sat,l} \equiv \frac{hc}{\lambda_l \tau_f \left[\sigma_a(\lambda_l, T) + \sigma_e(\lambda_l, T)\right]}. \tag{2.27}$$

In Eqs. (2.24) and (2.25) additional parameters have been introduced for convenience in the form

$$\beta_p \equiv \frac{\sigma_a(\lambda_p, T)}{\sigma_a(\lambda_p, T) + \sigma_e(\lambda_p, T)}, \tag{2.28}$$

$$\beta_l \equiv \frac{\sigma_a(\lambda_l, T)}{\sigma_a(\lambda_l, T) + \sigma_e(\lambda_l, T)}, \tag{2.29}$$

and

$$\beta_{pl} \equiv \frac{\beta_p \beta_l}{\beta_p - \beta_l}. \tag{2.30}$$

The thermal power density, according to Eq. (2.19), in absence of background absorption, is

$$\begin{aligned} H &= -\eta_{c,p} P_{abs,p} - \eta_{c,l} P_{abs,l} \\ &= I_p \alpha_p(I_p, I_l)\left[1 - \eta_{EQE}\frac{\lambda_p}{\lambda_f}\right] + I_l \alpha_l(I_p, I_l)\left[1 - \eta_{EQE}\frac{\lambda_l}{\lambda_f}\right] \end{aligned} \tag{2.31}$$

Radiation balanced is achieved when $H = 0$. The condition for radiation balance in the absence of background absorption is

$$\frac{I_{p,min}}{I_p} + \frac{I_{l,min}}{I_l} = 1, \tag{2.32}$$

in agreement with Bowman. The intensities in Eq. (2.32) are defined to be

$$I_{p,min} = I_{sat,p}\frac{\beta_{pl}}{\beta_p}\frac{\lambda_p}{\lambda_f}\frac{\eta_{ext}\lambda_l - \lambda_f}{\lambda_l - \lambda_p} \tag{2.33}$$

and

$$I_{l,min} = I_{sat,l}\frac{\beta_{pl}}{\beta_l}\frac{\lambda_l}{\lambda_f}\frac{\eta_{ext}\lambda_p - \lambda_f}{\lambda_l - \lambda_p}. \tag{2.34}$$

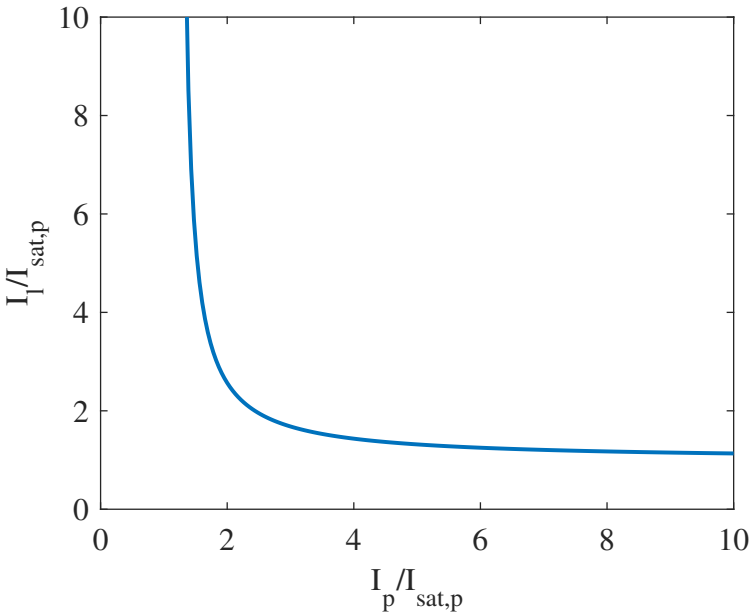

Figure 2.6: The radiation-balance condition from Eq.(2.32). Fixed parameters for the wavelength of the pump, and its absorption and emission cross sections were 1029.3 nm, 1.26×10^{-21} cm^2 and 2.24×10^{-20} cm^2, respectively. The wavelength and absorption and emission cross sections of the laser were 1048 nm, 8.83×10^{-23} cm^2, and 3.68×10^{-21} cm^2. The fluorescence lifetime was set to 0.95 ms. Pump and laser saturation intensities were calculated to be 8.59×10^3 W/cm^2 and 5.30×10^4 W/cm^2. The mean fluorescence wavelength and external quantum efficiency are 1012.1 nm and 99.3%.

Based on Eq. (2.32), to reach the condition for radiation balance, the pump and laser intensities need to be greater than $I_{p,min}$ and $I_{l,min}$ ($I_p > I_{p,min}$ and $I_l > I_{l,min}$). These two parameters are constants whose values are related to the saturation intensities at the pump and laser wavelength as shown in Eq. (2.33) and (2.34). Figure 2.6 plots the RBC for a 3% Yb:YAG crystal [24], using calculated values of $I_{p,min} = 1.23I_{sat,p}$ and $I_{l,min} = 0.99I_{sat,l}$. When the laser medium is at the RBC, both the pump and laser light fields saturate the medium, reducing the absorption and gain at pump and laser wavelengths. Hence, the RBL is normally pumped with a high intensity inside a high Q laser cavity to maintain the saturation condition and reduce the laser threshold. In the next section, the propagation of pump and laser fields will be considered to analyze thermal balance

under conditions when non-uniform intensity distributions may arise along the axis of the laser.

2.3.2 Light Field Propagation within Radiation-Balanced Medium

The heat density generated inside the laser medium was derived in the previous section to show the radiation balance at a single point within the material. In this section, radiation balance is analyzed as beams propagate through the laser medium.

When the pump and laser light fields propagate through the laser medium of RBLs or radiation-balanced amplifiers, the relations between intensities and propagation distance are

$$\frac{dI_p}{dz} = -I_p \alpha_p(I_p, I_l) \tag{2.35}$$

$$\frac{dI_l}{dz} = -I_l \alpha_l(I_p, I_l). \tag{2.36}$$

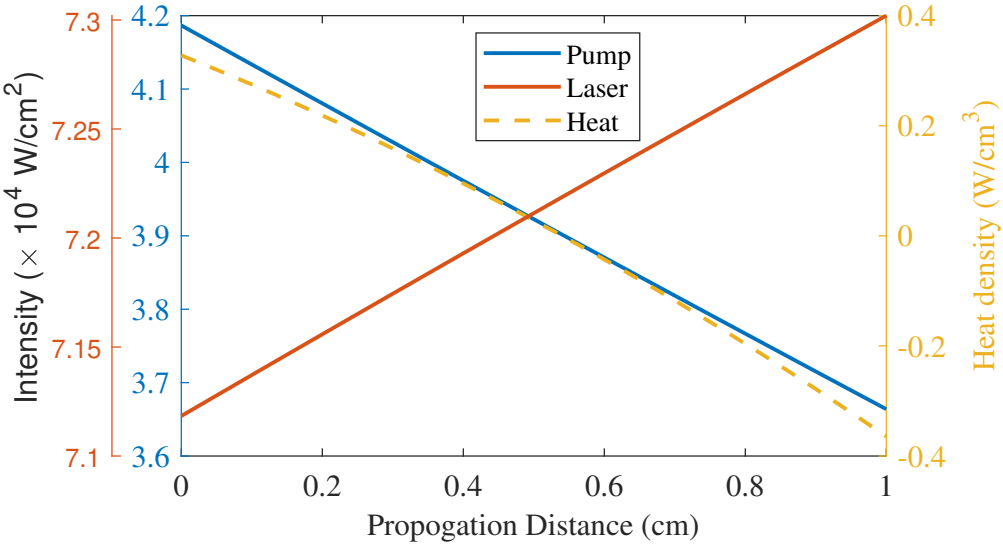

Figure 2.7: Pump (blue) and laser (red) intensities along the laser medium. The dashed yellow curve plots the heat density generated inside the material. In this simulation, the pump and laser light fields co-propagate through a 1 cm 3% Yb:YAG crystal, and the initial conditions for intensities are $I_p(z=0) = 4.87 I_{sat,p}$ and $I_l(z=0) = 1.34 I_{sat,l}$. The other parameters are the same as that of Fig. 2.6.

These two equations are coupled, and the light fields along the laser medium can be solved by imposing initial conditions on the intensities. Figure 2.7 plots the pump intensity and laser intensity along 3% Yb:YAG crystal [24] with initial conditions of $I_p(z=0) = 4.87 I_{sat,p}$ and $I_l(z=0) = 1.34 I_{sat,l}$. 12.5% of the pump intensity is absorbed and the laser intensity is amplified by 2.5% under RBC. The thermal power density generated inside the laser medium is calculated

from Eq. (2.31) and plotted in yellow. When light fields propagate through the laser medium (as described by Eq. (2.32)), the RBC is not maintained at every point inside the medium. The overall heat generated inside the laser medium needs to be calculated by integrating the heat intensity, Eq. (2.31), over the volume of the laser medium [9]. However, because the laser medium is saturated by both the pump and laser light fields near the radiation-balanced condition, the intensity variation is small, and Eq. (2.32) is still a good approximation for lightly doped or thin materials.

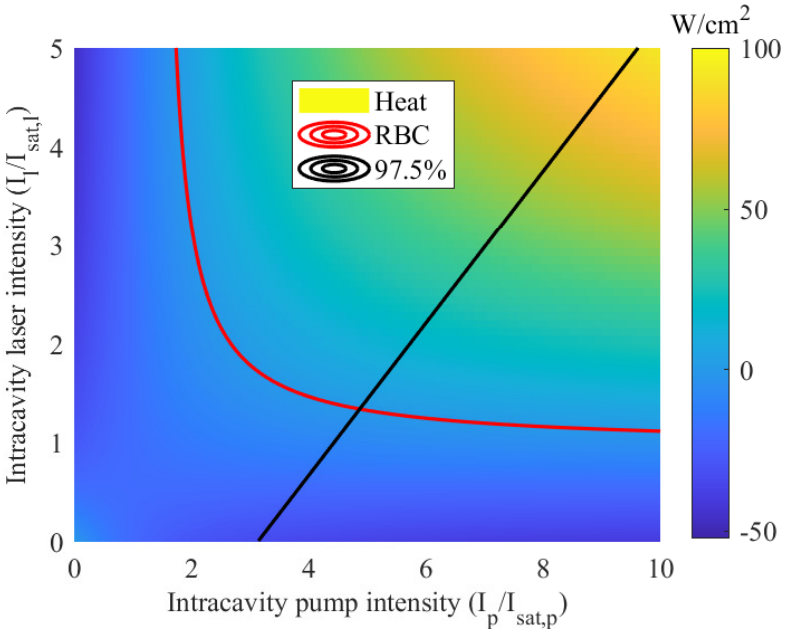

Figure 2.8: Pump and laser intensities and thermal intensity plot. The normalized intensities indicate the values at the initial position (propagation distance $z = 0$). The black curve gives the relation between the intracavitary laser and pump intensities with a 97.5% reflectivity at the laser wavelength for the output coupler. The other parameters are the same as that of Fig. 2.6. The color shows the integral of thermal density, Eq. (2.31), over the propagation distance. The red curve indicates the RBC, where net thermal power is zero. The RBL operates at the crossover point of black and red curves.

If the pump and laser fields co-propagate through the laser medium with the same beam size, a flat-top beam approximation can be used to simplify the calculation of heat energy by reducing the volume integral to the product of beam area and heat intensity. The heat intensity is calculated by integrating the heat density over the propagation distance. A representative plot of RBL based on 3% Yb:YAG [24] is shown in Figure 2.8. Increasing the pump intensity increases the gain at the laser wavelength. Once the gain is equal to the loss, the laser light field oscillates inside the cavity. The black curve shows the intracavity laser field, which appears once the pump intensity exceeds the threshold. The red curve indicates the locus of points along which the thermal power is zero (i.e., the RBC). In the region below the RBC curve, the crystal temperature decreases during

lasing. Conversely, in the region above the RBC, the crystal temperature increases during lasing. The condition for operating a radiation-balanced laser is indicated by the intersection between two curves, where the crystal temperature is unchanged during lasing.

It is important to note that in Fig. 2.8, the curve of the RBC (Eq.(2.32)) is continuous, which guarantees an intersection with the intracavity laser versus pump curve (black). In theory, when background absorption is ignored, any laser system can operate as a RBL if the pump is tuned to a wavelength where cooling efficiency is positive. In the next section, however, background absorption will be included in an extension of RBL theory to show that a constant value of impurity absorption eliminates the RBC, a significant oversight of earlier analysis since background absorption is the chief governing factor in ASF cooling. Furthermore, it will be shown that saturable impurity absorption restores solutions for radiation-balanced lasing and even extends the practicality of RBL operation to relatively impure materials.

2.4 Background Absorption in Radiation-Balanced Lasers

The RBL theory developed by Bowman [7] assumed that parasitic heating due to background impurities can generally be neglected and is intensity-independent. This seems reasonable at first because the large thermal load anticipated from near-resonant absorption by the active ions dwarfs that from low concentration impurities. Yet even weak background absorption is still a key limitation to self-cooling in RBLs. Consequently, efforts were made in the past to include parasitic heating in the RBL heat equation [8, 9]. Unfortunately, these inclusions were found to eliminate theoretical solutions for radiation balance in well-characterized materials that have been operated as RBLs in the lab [45, 46]. As summarized in this section, this problem originates from the neglect of saturation effects at the elevated light intensities that circulate inside RBL lasers. RBL pump fields need to saturate the absorption of active ions to achieve radiation balance. However, if the background absorption does not saturate, a linear increase in heat load from impurities accompanies any increase in pump intensity above threshold. As a consequence, radiation balance is predicted only for unrealistically pure media or extreme pump powers. Inclusion of impurity saturation, on the other hand, restores solutions for radiation balance in relatively impure materials and quantitatively predicts RBL operation.

2.4.1 Intensity-Independent Background Absorption

Background absorption was ignored in the review of RBL theory of Section 2.3. This neglect will be reconsidered in the present section. First, we note some characteristics of RBLs in which background absorption is considered to be an intensity-independent constant. In such a case, the

thermal power density (Eq. (2.31)) becomes

$$H = I_p\sigma_a(\lambda_p, T)\Delta N_p\left[1 - \eta_{EQE}\frac{\lambda_p}{\lambda_f}\right] + I_l\sigma_a(\lambda_l, T)\Delta N_l\left[1 - \eta_{EQE}\frac{\lambda_l}{\lambda_f}\right] + \alpha_b(I_p + I_l), \quad (2.37)$$

where α_b is the background absorption coefficient. By setting $H = 0$, the RBC can be calculated as in Section 2.3 and plotted for different assumed values of background absorption coefficient to explore operating conditions. As shown in Figure 2.9a, the inclusion of background absorption requires more cooling power to compensate the parasitic heating at the RBC. This leads to a downward shift of the curves in Figure 2.9a, rendering the laser output negligible. When the background absorption is not saturable ($\alpha_b > 1 \times 10^{-3}$ cm^{-1}), cooling is in fact prevented altogether at high intensities because of the linear increase of parasitic heating that tracks the input pump power.

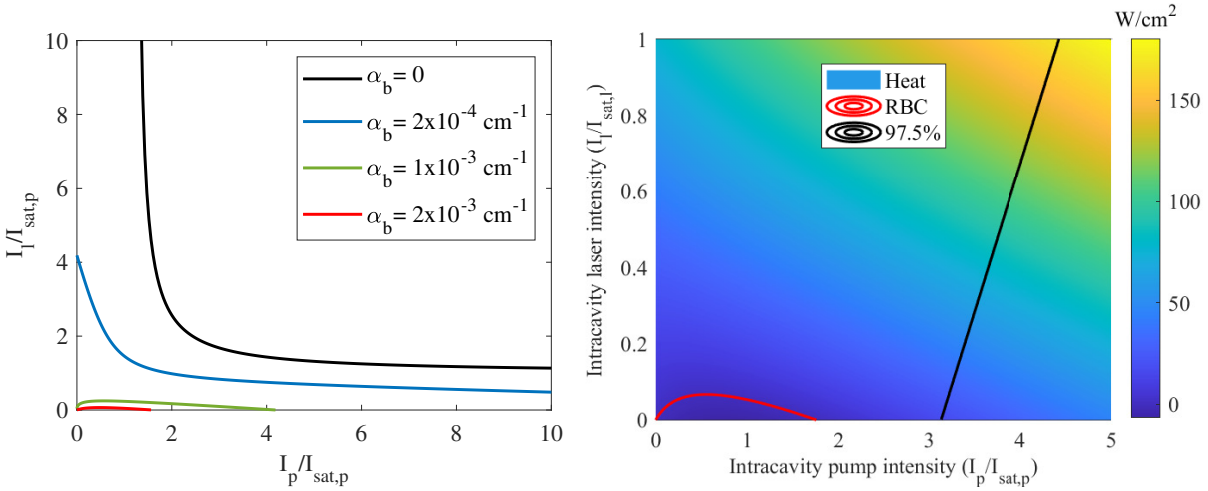

Figure 2.9: (a) The radiation-balance condition for 3% Yb:YAG based on Eq.(2.37) for different values of background absorption coefficient. The other parameters are the same as that of Fig. 2.6. (b) Pump and laser intensities and thermal intensity plot with a background absorption coefficient of 2×10^{-4} cm^{-1}. There is no crossover point for the laser curve (black) and RBC (red).

Figure 2.9b plots the pump and laser intensities with the background color indicating the thermal intensity. When the background absorption coefficient is 2×10^{-3} cm^{-1}, the RBC curve (red) shifts downward, reducing the laser output power and the efficiency of the RBL. Further, there is no intersection between the laser operating curve and the RBC. Thus, the theoretical solution for RBL operation vanishes altogether.

In existing RBL theory, if background absorption is included as a constant, even an unrealistically low value of background absorption changes the prediction for the radiation balance condition dramatically. This unavoidably results in a large mismatch between theoretical predictions

and experimental measurements [45, 46]. In the next section, saturable background absorption is included in an extension of RBL theory and is shown to resolve the disparity between prediction and measurements for realistic values of the absorption coefficient.

2.4.2 Saturation of Background Absorption

Background absorption was taken to be an unsaturable constant in the previous section, in keeping with published RBL analysis. In this section, however, the impurity absorption is allowed to saturate and a corrected condition for radiation balance is derived. The inclusion of impurity saturation not only resolves the poor agreement between prior theoretical RBC predictions and experimental observations, but also highlights the existence of solutions for radiation-balanced lasing in relatively impure materials.

The active ions of a RBL have previously been analyzed as isolated 2-level systems [45]. However, a number of shortcomings in earlier RBL theory can be addressed by including the background impurity ions as a second 2-level system coupled to the first through the relevant light fields. The condition for operating a laser under radiation-balanced conditions with significant background absorption and optical saturation of both the background and coolant ion species is formulated here.

The ground and excited state population densities of the active ions and background impurities are given by the sums

$$N_T = N_1 + N_2, \tag{2.38}$$

$$N'_T = N'_1 + N'_2. \tag{2.39}$$

Revised rate equations for the upper state population of the active ions and background impurities are

$$\frac{dN_2}{dt} = \frac{I_p \lambda_p}{hc} \left[\sigma_{a,p} N_1 - \sigma_{e,p} N_2\right] + \frac{I_l \lambda_p}{hc} \left[\sigma_{a,l} N_1 - \sigma_{a,l} N_2\right] - \frac{N_2}{\tau_f} \tag{2.40}$$

and

$$\frac{dN'_2}{dt} = \frac{I_p \lambda_p}{hc} \left[\sigma'_{a,p} N'_1 - \sigma'_{e,p} N'_2\right] + \frac{I_l \lambda_p}{hc} \left[\sigma'_{a,l} N'_1 - \sigma'_{e,l} N'_2\right] - \frac{N'_2}{\tau'_f}, \tag{2.41}$$

where the effective cross sections for active ions and background impurities have the form $\sigma_{i,j} \equiv \sigma_i(\lambda_j, T)$ and $\sigma'_{i,j} \equiv \sigma'_i(\lambda_j, T)$, where $i = (a, e)$ and $j = (p, l)$.

The net thermal power density H deposited in the medium by incident or internal light fields includes the power density absorbed from the pump and internal laser fields as well as that released by radiative and non-radiative relaxation processes. With the inclusion of saturable background

absorption, the expression for the power density becomes

$$\begin{aligned} H =& I_p \left[\sigma_{a,p} N_1 - \sigma_{e,p} N_2\right] + I_l \left[\sigma_{a,l} N_1 - \sigma_{a,l} N_2\right] - \eta_e \frac{hc}{\lambda_f} \frac{N_2}{\tau_r} \\ &+ I_p \left[\sigma'_{a,p} N'_1 - \sigma'_{e,p} N'_2\right] + I_l \left[\sigma'_{a,l} N'_1 - \sigma'_{e,l} N'_2\right]. \end{aligned} \tag{2.42}$$

The first two terms in Eq. (2.42) account for the energy exchange between the active ions and two cavity modes. The third term quantifies the flow of energy out of the laser medium via fluorescent emission, corrected for escape efficiency. The last two terms are the power density absorbed by background impurities at the pump and laser wavelengths.

By solving Eqs. (2.40, 2.41) under steady-state conditions, the absorption coefficients at the pump and laser wavelengths are found to be

$$\alpha_p(I_p, I_l) = \alpha_p(0,0) \frac{\frac{\beta_l I_l}{\beta_{pl} I_{sat,l}} + 1}{\frac{I_p}{I_{sat,p}} + \frac{I_l}{I_{sat,l}} + 1} \tag{2.43}$$

$$\alpha_l(I_p, I_l) = \alpha_l(0,0) \frac{-\frac{\beta_p I_p}{\beta_{pl} I_{sat,p}} + 1}{\frac{I_p}{I_{sat,p}} + \frac{I_l}{I_{sat,l}} + 1} \tag{2.44}$$

$$\alpha'_p(I_p, I_l) = \alpha'_p(0,0) \frac{\frac{\beta'_l I_l}{\beta'_{pl} I'_{sat,l}} + 1}{1 + \frac{I_p}{I'_{sat,p}} + \frac{I_l}{I'_{sat,l}}} \tag{2.45}$$

$$\alpha'_l(I_p, I_l) = \alpha'_l(0,0) \frac{-\frac{\beta'_p I_p}{\beta'_{pl} I'_{sat,p}} + 1}{1 + \frac{I_p}{I'_{sat,p}} + \frac{I_l}{I'_{sat,l}}}, \tag{2.46}$$

where

$$\beta'_i \equiv \frac{\sigma'_{a,i}}{\sigma'_{a,i} + \sigma'_{e,i}} \tag{2.47}$$

$$\beta'_{pl} \equiv \frac{\beta'_p \beta'_l}{\beta'_p - \beta'_l}. \tag{2.48}$$

As before, the expressions above have been written in terms of saturation intensities defined by

$$I_{sat,p} \equiv \frac{hc}{\lambda_p \tau_f \left[\sigma_{a,p} + \sigma_{e,p}\right]} \tag{2.49}$$

$$I_{sat,l} \equiv \frac{hc}{\lambda_l \tau_f \left[\sigma_{a,l} + \sigma_{e,l}\right]} \tag{2.50}$$

$$I'_{sat,i} = \frac{hc}{\lambda_i \tau' \left[\sigma'_{a,i} + \sigma'_{e,i}\right]}. \tag{2.51}$$

The thermal power density can now be written in a form that accounts for saturation effects and non-radiative decay in the laser medium:

$$\begin{aligned} H &= -\eta_{c,p}P_{abs,p} - \eta_{c,l}P_{abs,l} \\ &= I_p\left[\alpha_p(I_p,I_l)+\alpha'_p(I_p,I_l)\right]\left[1-\eta_{ext}\eta_{abs,p}\frac{\lambda_p}{\lambda_f}\right] + I_l\left[\alpha_l(I_p,I_l)+\alpha'_l(I_p,I_l)\right]\left[1-\eta_{ext}\eta_{abs,l}\frac{\lambda_l}{\lambda_f}\right]. \end{aligned} \tag{2.52}$$

In Eq. (2.52), absorption efficiencies have been defined for the pump and laser fields according to

$$\eta_{abs,p} = \frac{\alpha_p(I_p,I_l)}{\alpha_p(I_p,I_l)+\alpha'_p(I_p,I_l)} \tag{2.53}$$

$$\eta_{abs,l} = \frac{\alpha_l(I_p,I_l)}{\alpha_l(I_p,I_l)+\alpha'_l(I_p,I_l)}. \tag{2.54}$$

The radiation balance condition (RBC) is achieved when $H = 0$. Since the thermal power density in Eq. (2.52) has been altered from its earlier form, the RBC is no longer given by Eq. (2.32). By modifying the definitions of $I_{p,min}$ and $I_{l,min}$, the RBC can nevertheless be preserved in a form similar to Eq. (2.32), namely

$$\frac{I_{p,min}}{I_p} + \frac{I_{l,min}}{I_l} = 1 + C, \tag{2.55}$$

where

$$C = \frac{\beta'_p - \beta'_l}{\beta_p - \beta_l}\frac{\sigma'_{a,p}N'_T}{\sigma_{a,p}N_T}\frac{\beta_p I_{sat,l}}{\beta'_p I'_{sat,l}}\frac{1+\frac{I_p}{I_{sat,p}}+\frac{I_l}{I_{sat,l}}}{1+\frac{I_p}{I'_{sat,p}}+\frac{I_l}{I'_{sat,l}}} \tag{2.56}$$

$$I_{p,min} = I_{sat,p}\frac{\beta_{pl}}{\beta_p}\frac{\lambda_p}{\lambda_f}\frac{\eta_{ext}\lambda_l - \lambda_f(1+R_l)}{\lambda_l - \lambda_p} \tag{2.57}$$

$$I_{l,min} = I_{sat,l}\frac{\beta_{pl}}{\beta_l}\frac{\lambda_l}{\lambda_f}\frac{\eta_{ext}\lambda_p - \lambda_f(1+R_p)}{\lambda_l - \lambda_p} \tag{2.58}$$

and

$$R_p = \frac{\sigma' N'_T}{\sigma_{a,p}N_T}\frac{1+\frac{I_p}{I_{sat,p}}+\frac{I_l}{I_{sat,l}}}{1+\frac{I_p}{I'_{sat,p}}+\frac{I_l}{I'_{sat,l}}} \tag{2.59}$$

$$R_l = \frac{\sigma' N'_T}{\sigma_{a,l}N_T}\frac{1+\frac{I_p}{I_{sat,p}}+\frac{I_l}{I_{sat,l}}}{1+\frac{I_p}{I'_{sat,p}}+\frac{I_l}{I'_{sat,l}}}. \tag{2.60}$$

When formulated to take into account background saturation, the radiation-balance condition acquires intensity-dependent factors C and R_i. If the variation of the impurity cross sections with wavelength is weak ($\beta'_p \approx \beta'_l$), or the effective absorption cross section is larger than the

effective emission cross section ($\beta_i' > 0.5$), the factor C is negligible ($C \approx 0$). Under these circumstances, impurity saturation plays an insignificant role in RBL operation and the RBC (Eq. (2.55)) has exactly the same form as Eq. (2.32), published originally in Ref. [7]. The factor R_i depends on the small signal absorption coefficients, the pump and laser intensities, and the corresponding saturation intensities. When the saturation intensity of active ions is comparable to the saturation intensity of impurities, the factor R is mainly determined by the ratio of small signal absorption coefficients of the background and coolant ions. If the impurity concentration is considered negligible, or impurities are simply ignored, R vanishes. Then Eq. (2.55) not only reduces to Eq. (2.32) but reproduces the prior result of Ref. [7].

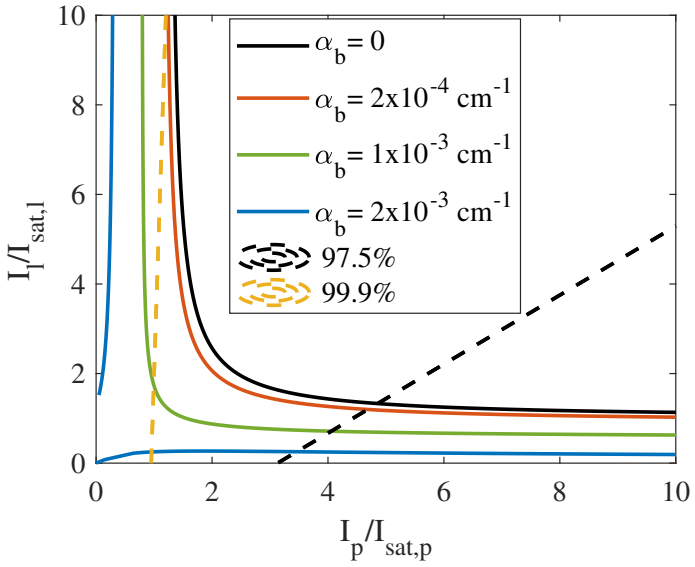

Figure 2.10: The theoretical RBC plotted for different values of background absorption coefficient. Saturation of parasitic heating shifts the RBC down as the background absorption coefficient increases. Impurity saturation intensity was assumed to be 2×10^4 W/cm^2 and the remaining parameters are the same as that of Fig. 2.6. The dashed lines give the relations between the intracavitary laser and pump intensities with 97.5% or 99.9% reflectivity at the laser wavelength for the output coupler.

When impurities are not ignored, the factor R introduces important dependencies on concentration and intensity, as we now show. Fig. 2.10 plots the radiation-balance condition for 3% Yb:YAG [24] for different values of background absorption with an assumed impurity saturation intensity of 2×10^4 W/cm^2. The curve depicting the RBC shifts downward as impurity concentration increases, making it possible to balance the thermal load with background absorption as high as 2×10^{-3} cm^{-1} at relatively low pump intensity. Furthermore, when the background absorption falls below 2×10^{-4} cm^{-1}, the parasitic heating has an insignificant effect on radiation balance in the model. This explains why the original RBL model that excluded background ab-

sorption altogether appeared to fit experimental measurements based on an arbitrary assumption of a vanishingly small background absorption [45].

Note the blue curve has an intersection with the y-axis and it is multi-valued near the origin. At low intensities, the cooling power at 1048 nm laser wavelength is small for 3% Yb:YAG crystal (Fig. 4.4). With the increase of the background absorption, the parasitic heating is increased and it overcomes the cooling power with a background absorption value of 2×10^{-3} cm^{-1} (blue curve). Then the laser beam induces heating at low intensity with this impurity level, instead of cooling. However, the cooling efficiency is modified with the increase in intensities. Recall that the laser saturation intensities was calculated to be 5.30×10^4 W/cm^2, and the impurity saturation intensity was assumed to be 2×10^4 W/cm^2 ($I_{sat,l} > I_b$). The absorption of background saturates before Yb^{3+}, reducing the parasitic heating. Then at high intensity, the laser beam induces a cooling, which is reversed compared to the situation at low intensity. With the increase of the laser intensity (along y-axis) in absence of the pump light, the background absorption saturates first, which turns the initial heating at low intensity to cooling at high intensity, leading to the intersection between the blue curve and y-axis. The blue curve indicates that the cooling induced by the pump light is balanced by the heating induced by the laser light. The laser-induced heating depends on both the laser intensity and cooling efficiency. Near the origin, the heating is small, which can be induced by a near-zero laser intensity (lower trace) or a near-zero cooling efficiency (upper trace). Hence, the blue curve is multi-valued near the origin.

Recall that the radiation-balanced condition plotted in Fig. 2.10 only shows the relation between two light intensities at the condition where the cooling power is zero when the crystal is illuminated by two light beams at pump and laser wavelengths. For the relation between the intracavity pump and laser intensities inside a laser cavity, the rate equation Eq.(2.40) needs to be solved. The dashed black line indicates the normalized intracavity laser intensity versus pump intensity with an output coupler of 97.5%. With the increase of the background impurity absorption, the radiation-balanced condition can be achieved at a lower pump intensity, with a reduced laser intensity. Although the RBC is multi-valued for high impurity levels near the origin, normally there is no intersection between the dashed laser intensity versus pump intensity lines (yellow dashed line) and the upper RBC curve (upper blue curve) because the threshold shifts the laser lines to the high pump intensities. For example, the gain of 3% Yb:YAG at laser wavelength (Eq. (2.44)) is positive only when $I_p > 0.8 I_{sat,p}$. The yellow dashed line indicates the laser versus pump with an output coupler of 99.9% reflectance, where the threshold is at $Ip \sim 0.9 I_{sat,p}$. Only one intersection is observed even with a close to unity output mirror reflectance. If there are several intersections between the laser line and RBC curve in other crystals, then with the increase of the pump intensity, the balanced condition can be achieved at several separated pump intensities.

By incorporating saturation of both the impurity and coolant ions, the present analysis offers a

more general model of cooling efficiency. In addition, it extends RBL theory to impure gain media that were previously predicted to require unrealistically high powers to operate or that had no analytic solution for radiation balance at all. Moreover, this model indicates that some gain media that fail to achieve any net refrigeration in low intensity laser cooling experiments could operate as RBLs. Experimental results showing that background saturation improves cooling efficiency in agreement with this conclusion are covered in Section 4.3.

CHAPTER 3

Experimental Procedures

This chapter discusses the experimental procedures to evaluate materials for laser refrigeration and designs for RBLs. All of the samples examined in this work are listed in Section 3.1. Procedures for measuring their absorption and emission spectra as well as MFW are detailed in Section 3.2. Precise thermometry used in this work is described in the following Section 3.3. Then, methods of measuring cooling power and cooling efficiency are addressed in section 3.4. Next, the pump locking technique for achieving a RBL is introduced. In the end, experimental designs of RBLs are presented in Section 3.6.

3.1 Laser-Cooled Samples

This section presents information on all the samples used in this work, which is tabulated in Table 3.1. Laser cooling was investigated in Yb:YLF, Yb:KYW, and Yb:YAG crystals. Yb:YLF crystal maintains the MAT record of 91K [5] and Yb:KYW crystal has the highest figure of merit among Yb^{3+} doped RBL mediums [15]. Yb:YAG crystal is the only bulk medium where RBLs were achieved [8, 9] prior to this work.

Samples	Doping (Mole %)	Size (mm^3)	Source
Yb:YAG	3	$1 \times 1 \times 10^B$	Scientific Materials
Yb:KYW	1	$1 \times 1 \times 10^B$	Altechna
Yb:KYW	2	$0.9 \times 1.2 \times 10$	FEE
Yb:KYW	10	$1 \times 1 \times 10^B$	Altechna
Yb:KYW	20	$1 \times 1 \times 10^B$	Eksma
Yb:YLF	10	$3.4 \times 5.1 \times 5.6$	Loan from Ref. [55]

Table 3.1: List of all samples used in this work. [B] Sample has Brewster-cut end faces.

The Yb:YAG and Yb:KYW samples were commercially available and purchased from the companies listed in the right column, and the Yb:YLF sample was a loan courtesy of Prof. J. R. Silva,

Universidade Estadual de Mato Grosso do Sul, Brazil and used in Ref. [55]. All Yb:KYW crystals were cut with the Ng axis parallel to the 10 mm edge. The 1% and 10% samples were Brewster-cut Nm parallel to the plane of incidence. The 2% sample, which had the Nm axis parallel to the shortest edge, was coated for anti-reflection over the range 970-1070 nm. The orientation of crystal axes for Yb:YLF is presented in Appendix A.

3.2 Material Spectroscopy

The spectroscopic properties of materials are important for both laser cooling studies and RBLs. In Section 3.2.1, the procedure of measuring absorption and emission cross sections using the McCumber [56] relation is introduced. And the method of measuring the MFW is covered in subsection 3.2.2 using the fluorescent spectra at three orthogonal polarizations.

3.2.1 Absorption and Emission Cross Sections

The samples studied in this work have two different sizes (table 3.1), the small Yb:YAG and KYW crystals and the large Yb:YLF crystal, leading to two different methods of measuring the cross sections.

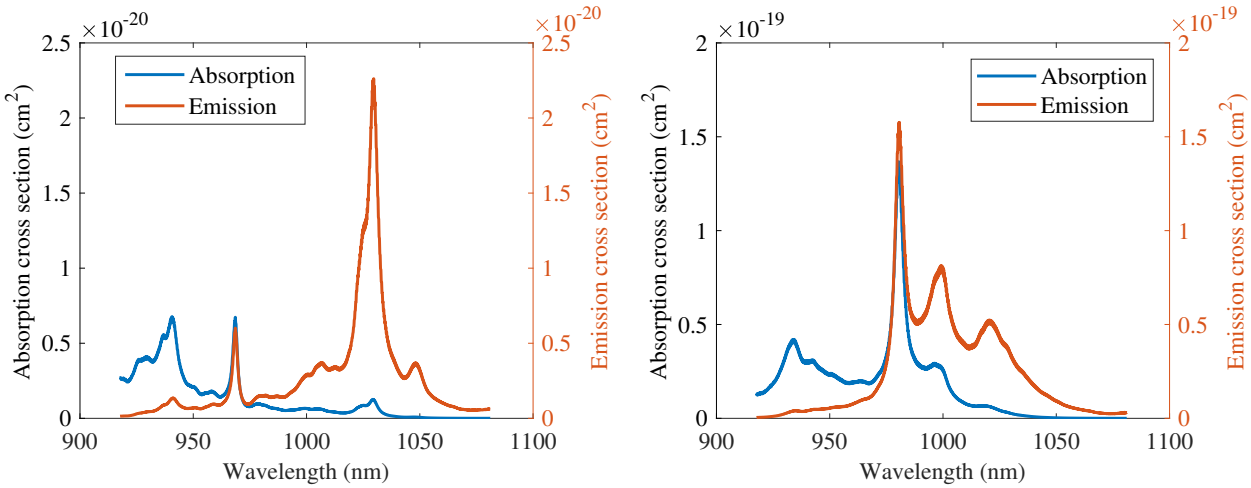

Figure 3.1: (a) Absorption and emission cross sections for 3% Yb:YAG. (b) Absorption and emission cross sections for 1% Yb:KYW (polarization $E||N_m$).

For the small Yb:YAG and Yb:KYW crystals, the emission spectrum was measured and the absorption spectrum was calculated using the McCumber [56] relaxation. The crystals were pumped with a tunable Ti:Sapphire laser (M Squared SolsTiS, 750 – 1050 nm) near the surface to avoid

reabsorption, and the infrared luminescence was collected with a multimode optical fiber (Ocean Optics QP600-2-VIS-NIR; NA= 0.4) connected to a 0.25 m grating spectrometer (Oriel 74100) equipped with a CCD detector (Andor DU491A-1.7). A polarizer was placed between the crystal and the collecting fiber to ensure the measured spectrum has the same polarization as the pump. The absorption cross section was calculated using the McCumber relation based on measured fluorescence data. To permit scaling of the absolute value of absorption and emission cross-sections, the absorption coefficients were determined by tuning the Ti:Sapphire laser to 1030 nm (Yb:YAG) or 1025 nm (Yb:KYW) and measuring the incident, reflected, and transmitted laser powers. Figure 3.1 shows the measured absorption and calculated emission cross sections with this technique.

For the larger Yb:YLF crystal, the absorption spectrum was measured directly with a SHIMADZU UV-3600 spectrophotometer, and the emission spectrum was calculated using the McCumber relation. The measured cross sections for the Yb:YLF crystal are plotted in 2.2a.

3.2.2 Mean Fluorescence Wavelength

As mentioned in Section 2.1.2, the polarized-averaged MFW characterizes the average emitted photon energy that escaped from the crystal, which takes the radiation trapping into account. Experimentally, MFW was measured with the crystal pumped at the center to ensure the reabsorption was included. A rotating polarizer was placed between the crystal and fiber to collect the fluorescence along two orthogonal polarizations. The fluorescence was measured at both the side and the top of the crystal, measuring the four spectra along three orthogonal polarizations, and the common one was used as the reference to compensate for the difference of coupling induced by repositioning the fiber. Then Eq. (2.2) was used to compute the polarized-averaged MFW, and the computed values are shown in table 4.1 in Section 4.2. Fluorescence spectra for all the KYW samples are compared in Fig. 3.2 where the effects of self-trapping of the emission are evident in the lower three traces as suppressed intensity around 980 nm.

3.3 Temperature Measurement

The previous section covered the methods for material spectroscopy. In this section, two methods of monitoring the crystal temperature are introduced, infrared thermography and Differential Luminescence Thermometry (DLT). Infrared thermography was accomplished using a thermal camera to collect the black-body radiation (BBR) from the sample surface, which is a two-dimensional measurement that images the temperature distribution across the surface. DLT deduced the temperature based on the collected fluorescence, which measures the average temperature of the illuminated part of the sample. Both methods are non-contact and will not add additional heat load to

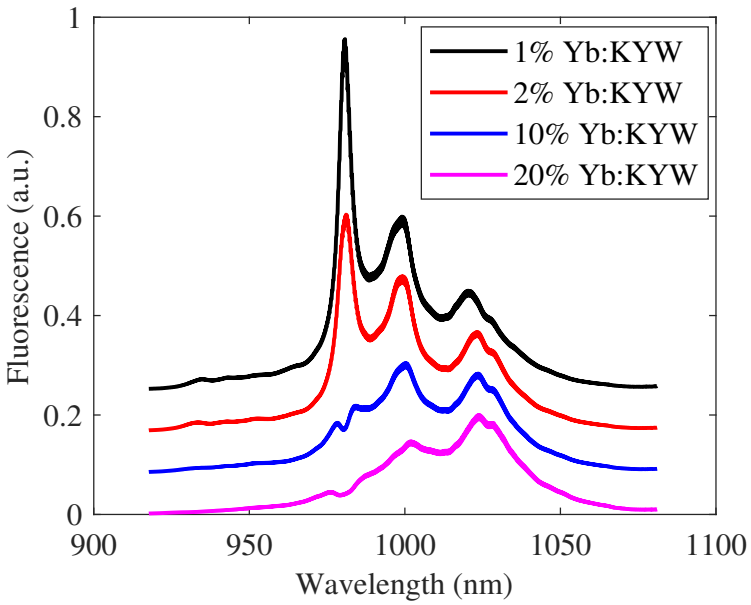

Figure 3.2: Emission spectra for samples of Yb:KYW doped with 1, 2, 10, and 20% Yb^{3+} (polarization $E//N_m$). The emission peak at ~980 nm was reabsorbed at high dope density.

the samples. These two methods were cross-checked for reliability and were in good quantitative agreement, within 0.1 K (Section 4.1).

3.3.1 Infrared Thermography

Infrared thermography was performed using a FLIR A655sc (equipped with a T198059 lens with a resolution of 50 μm/pixel in the 7.5-14 μm range) to monitor the temperature of the medium during the cooling experiments. The thermal camera collects the Black-Body Radiation (BBR) of the sample, from which the radiated power, based on Stefan–Boltzmann law, is

$$P = \epsilon \sigma A T^4, \tag{3.1}$$

where the σ and A are the Stefan–Boltzmann constant and crystal surface area, respectively. ϵ is the surface emissivity, which is the crystal parameter. Eq. (3.1) shows that if the emissivity is known, the crystal temperature can be calculated from the measured BBR by the thermal camera.

However, the radiation collected by the camera is not only emitted by the sample itself. Radiation from the surroundings reflected via the sample surface is also collected by the camera. What's more, the radiation from the sample and the reflected radiation will be influenced by the absorption of the atmosphere. To measure temperature accurately, it is therefore necessary to compensate for the effects of a number of different radiation sources.

Figure 3.3 illustrates the factors influencing thermographic measurements. τ is the transmission

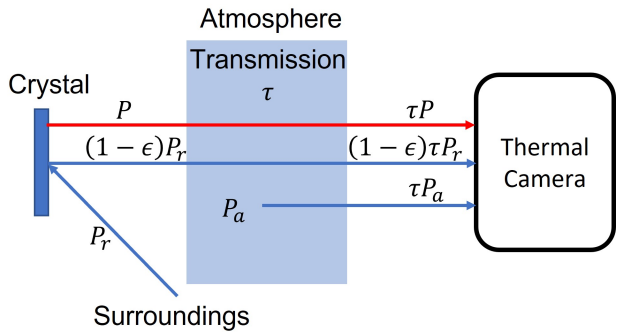

Figure 3.3: A schematic representation of thermographic measurements.

of the atmosphere, which depends on the room temperature T_{atm}, humidity H_{atm}, and the distance d between the object and the camera. The red arrow indicates the radiation from the sample, P, which is related to emissivity ϵ and crystal temperature T. This sample radiation, after absorption in the atmosphere, is collected by the camera. The emission of the surroundings P_r is characterized by a reflected temperature T_{ref}. This emission from surroundings, after being reflected from the sample surface and attenuated by the absorption of the atmosphere, is also collected by the camera. In addition, the atmosphere itself has an emission of P_a, which is related to the atmosphere temperature T_{atm}. What's more, the add-on lens reduced the transmitted radiation and introduced additional radiation from itself, which is characterized by the lens transmission τ_{lens} and lens temperature T_{lens}. Hence, the collected radiation relates to the crystal temperate with corrections of 7 parameters, T_{atm}, H_{atm}, d, ϵ, T_{ref}, τ_{lens}, T_{lens}. The FLIR software handles all the corrections based on the inputs of these parameters. Among all these parameters, the atmosphere temperature T_{atm} and H_{atm} were measured by a thermometry (Fisher Scientific, accuracy ± 1°C and $\pm 1\%$) during the experiments. The distance between the sample and camera d was equal to the focal length of the add-on mirror, 83 mm. The transmission of the add-on lens τ_{lens} is 0.9, specified by FLIR. The temperature of the add-on lens T_{lens} was assumed the same as the room temperature T_{atm}. Then, the crystal temperature can be measured based on the collected radiation with two parameters, crystal emissivity ϵ and reflected temperature T_{ref}.

To measure the emissivity, the BBR were collected at various crystal temperatures. The sample was placed in a temperature controller (Quantum Northwest Flash 300) with an accuracy of $\pm$ 0.01 K, as shown in the inset photo of Fig. 3.4. The average region of the measurements is indicated as the red box in the inset thermal image. The BBR was collected at a range of temperatures, then the emissivity ϵ and reflected temperature T_{ref} were adjusted such that the temperature measured from the thermal camera at each step was close to the temperature readout from the temperature controller. Figure 3.4 plots the thermal camera data taken over a range of temperatures for calibration of 1% Yb:KYW using Eq. (3.1). Note that the reflected temperature T_{ref} added a constant back-

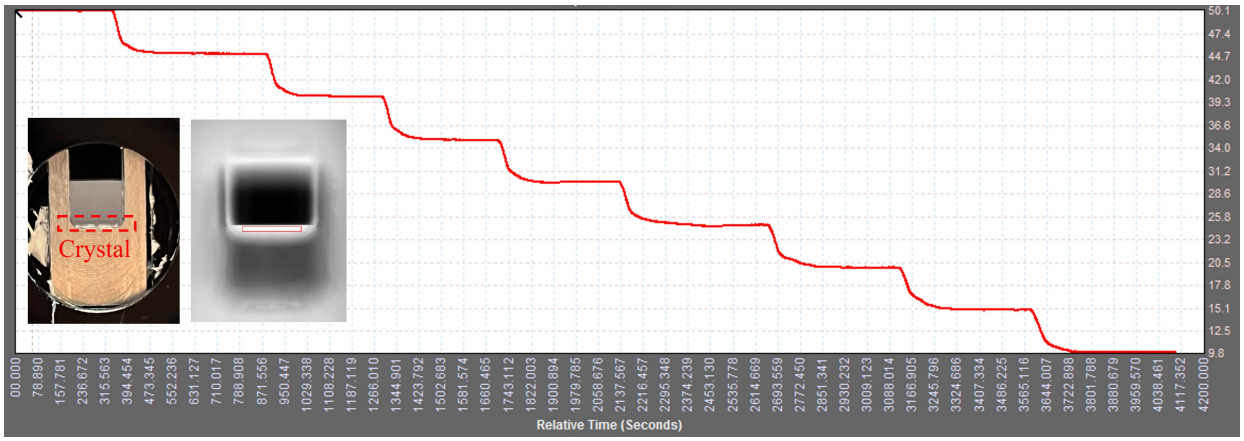

Figure 3.4: Thermal camera data taken over a range of temperatures for calibration of 1% Yb:KYW. The inset photo shows the setup, where the crystal (transparent) was supported by an aluminum structure within the temperature controller. The red box of the thermal image indicates the region of averaging.

ground to the measured temperature. Once the emissivity is known, every time when the camera was repositioned, the reflected temperature T_{ref} needed to be adjusted so that the measured crystal temperate equals the room temperature. Another thing to note is that the focus of the thermal camera, controlled by the FLIR software, is important. Experimentally, the focus was tuned so that the edge of the crystal was sharp on the thermal camera, as shown in the thermal image of Fig. 3.4 and Fig. 3.5b.

With the measured emissivities, the transient temperature measurements were recorded using FLIR's ResearchIR software with a frame rate of 1 Hz during the cooling experiments. Figure 3.5 shows the thermal images for a cooling experiment on the 1% Yb:KYW. Before the experiment, the crystal temperature was equal to the room temperature, as shown in Fig. 3.5a. When pumped with 1 W at 1025 nm, the temperature was 1.8 K below room temperature at steady state, and the crystal became dark on the thermal image as shown in Fig. 3.5b.

3.3.2 Differential Luminescence Thermometry

Differential Luminescence Thermometry (DLT) deduces the sample temperature based on the variations of emission spectra with temperature [44]. The fluorescence spectra were collected in real-time during pumping, and the temperature was calculated based on the transition lineshape according to a calibration.

Luminescence for all the samples excited with on-axis pumping was collected with a multimode optical fiber (Ocean Optics QP600-2-VIS-NIR; NA = 0.4) and analyzed with a 0.25 m grating spectrometer (Oriel 74100) equipped with a CCD detector (Andor DU491A-1.7). The DLT calibration

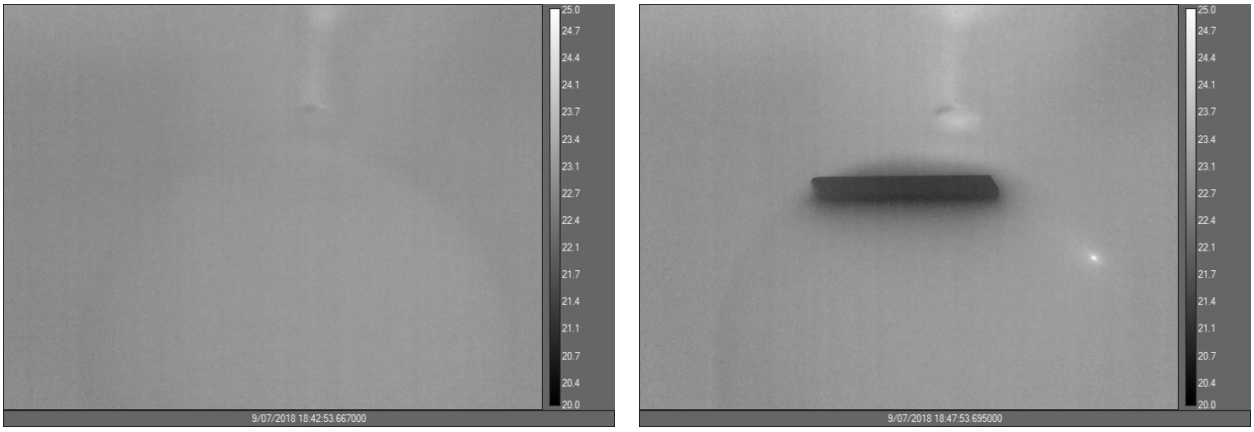

(a) (b)

Figure 3.5: Thermal images for a cooling experiment on the 1% Yb:KYW. (a) Pump is blocked, and the temperature of the crystal is equal to room temperature. (b) Steady-state crystal temperature (1.8K below room temperature) when pumped with 1 W at 1025 nm.

was performed by recording the fluorescence at a range of temperatures in steps of 0.5°C in a temperature-controlled oven (Quantum Northwest Flash 300) with an accuracy of ± 0.01 K.

The sample spectrum recorded at the highest temperature served as a reference. The absolute value of the difference between the normalized reference and any chosen normalized luminescence spectrum was integrated over a selected wavelength range to yield the DLT signal. Mathematically, the difference in the normalized spectrum is calculated using the expression

$$\Delta S(\lambda, T, T_0) = \frac{S(\lambda, T)}{\int S(\lambda, T)\, d\lambda} - \frac{S(\lambda, T_0)}{\int S(\lambda, T_0)\, d\lambda}, \tag{3.2}$$

where $S(\lambda, T)$ is the measured spectrum at temperature T. Then the DLT signal is

$$S_{DLT} = \int_{\lambda_1}^{\lambda_2} |\Delta S(\lambda, T, T_0)|\, dx, \tag{3.3}$$

where λ_1 and λ_2 limit the spectrum region of interest for the integral.

Figure 3.6 shows the spectrum of 1% Yb:KYW crystal for calibration. The normalized spectrum near the mean peak at 980 nm (Fig. 3.6a) had a temperature-dependent lineshipe and the small dependence was amplified by subtracting the reference temperature at 30°C using Eq. (3.2) as shown in Fig. 3.6b. Then the DLT signal was calculated by integrating the difference of normalized spectrum from 970 nm to 990 nm and linearly fitted to give a calibration curve as shown in Fig. 3.7.

With the calibration curve, the temperature of samples can be calculated based on the real time

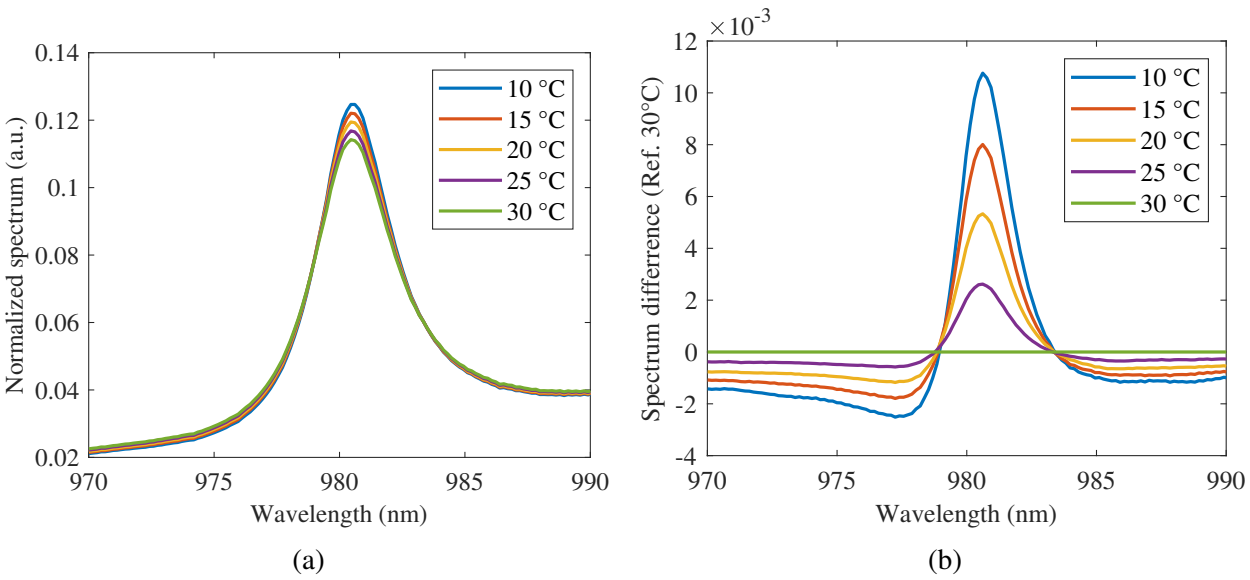

Figure 3.6: DLT calibration for 1% Yb:KYW (a) Normalized fluorescence spectrum near the main peak at 980 nm plotted at different temperatures. (b) Calculated DLT difference using Eq. (3.2) with a reference spectrum at 30°C.

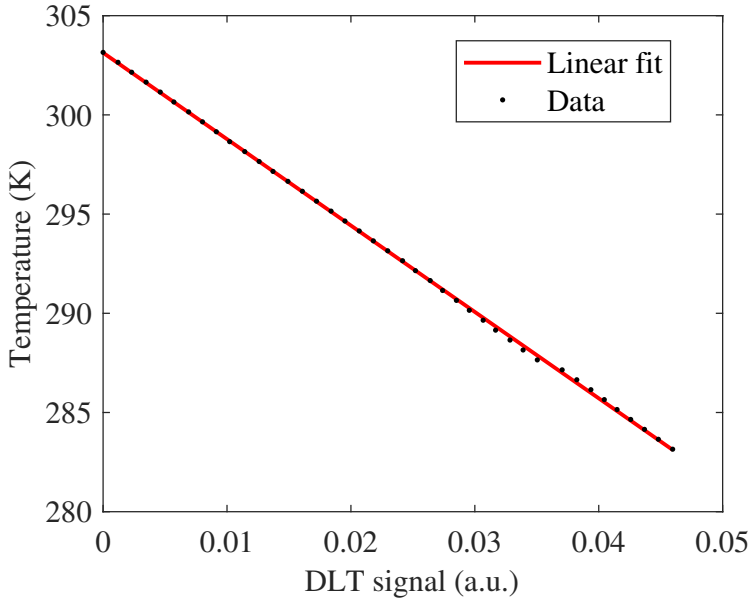

Figure 3.7: DLT calibration plot for 1% Yb:KYW. Black points are calculated DLT data using Eq. (3.3). The red curve shows the linear fit to the calculated DLT data.

collection of fluorescence spectrum. The infrared luminescence was analyzed by DLT in a time short enough (20 ms) to permit real-time tracking of the temperature dynamics. One hundred measurements were averaged to reduce noise, i.e. 2 seconds per measurement, so it was possible

to follow cooling or heating dynamics in real time.

3.4 Cooling Power and Cooling Efficiency Measurement

The previous section discussed the methods of temperature measurement, which enable the characterization of the cooling efficiency and cooling power. The cooling efficiency evaluates the cooling performance of different materials and cooling power estimates the capacity of heat compensation in RBLs. The optimization of thermal isolation and two methods of measuring the cooling efficiency or cooling power, a steady-state method and a dynamic method, are discussed in following subsections.

The cooling efficiency and cooling power can be determined from the thermal balance equation based on the measured temperature change of samples. This equation [57, 58] accounts for the various contributions to heating power in a crystal of temperature T, emissivity ϵ and surface area A_{surf} under the assumption that it is enclosed by a blackbody radiator at the environmental temperature T_0.

$$cM\frac{dT}{dt} = -\eta_c P_{abs} + A_{surf}\varepsilon\sigma_B\left(T_0^4 - T^4\right) + \left(h_{cv}A_{surf} + k\frac{A_{ct}}{L}\right)(T_0 - T) \tag{3.4}$$

The parameters c, M, σ_B, h_{cv}, k, A_{ct}, and L in Eq. (3.4) are the sample specific heat, sample mass, the Stefan-Boltzmann constant, convective heat transfer coefficient, thermal conductivity of the link, cross-sectional area, and sample length, respectively.

The left hand side of Eq. (3.4) is determined directly by observed rates of temperature change, together with some fixed sample properties. The rate of heating or cooling then reflects the balance of energy loss or gain processes from the three terms on the right side of the equation. These terms describe in succession the laser-induced energy gain or loss per unit time, the power exchanged between the sample and its surroundings due to blackbody radiation, and the power lost or gained through thermal conduction. The conduction term has two parts, corresponding to contact of the sample surface with air and conduction through the sample support.

3.4.1 Thermal Isolation

For laser cooling experiments, the accumulated temperature difference between the samples and the supports induces a conductive heat transfer from the support to the laser-cooled samples, which adds an additional thermal load and compromises the cooling power, as shown in Eq. (3.4). Hence, thermal isolation is important in the experiment to maximize the overall cooling power.

The thermal balance equation, Eq. (3.4), gives two directions to minimize the thermal load from the support, reducing the cross-sectional area or selecting a supporting material with low thermal

conductivity. Hence the samples were supported in either of two ways: (a) on three glass capillaries oriented transverse to the sample length to minimize the line contacts, or (b) on a commercial aerogel disk (Classic Silica Disk, Aerogel Technologies), which has a exceedingly low thermal conductivity. Figure 3.8 gives the schematic of the experimental setup for 1% Yb:KYW crystal. Experimental results (Section 4.1) showed that the aerogel method maintained a better thermal isolation because of its low thermal conductivity, where a temperature drop of 1.8K was achieved with aerogel support while only 0.5K temperature drop was observed with glass capillaries.

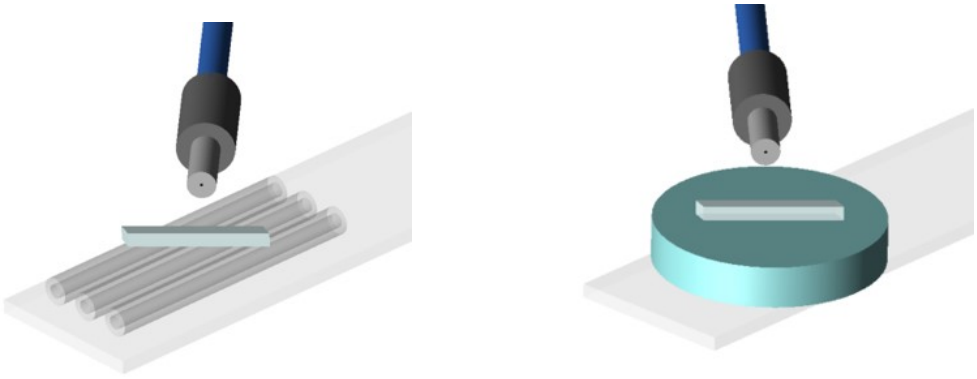

(a) (b)

Figure 3.8: Schematic of the experimental setup for 1% Yb:KYW crystal supported by (a) three glass capillaries and (b) a commerical aerogel. The fiber was used to collect the fluorescence.

3.4.2 Steady-State Method

The steady-state method measures the wavelength-dependent temperature change at steady state. Then a best fit, based on the theoretical prediction of cooling power, is performed to the measured temperature change, to determine the the cooling power, external quantum efficiency, background absorption, and cooling efficiency.

Cooling power in general has a nonlinear relationship with respect to temperature changes when convection, blackbody radiation, and impurity absorption are taken into account. However, it exhibits a simple proportionality to the steady-state value of ΔT for small temperature excursions. When the temperature change of the crystal is small, the second term in the right hand side of Eq. (3.4) can be approximated as $4A_{surf}\epsilon\sigma_B T_0^3 \Delta T$ [58]. Then the heat equation in steady state reduces to

$$P_c = a \times \Delta T. \tag{3.5}$$

where a is a constant. The steady state cooling power is proportional to the steady state temperature change ΔT. The experimentally measured cooling power equals the theoretical estimation

according to Eq. (2.4),

$$P_c = a \times \Delta T = \left[\eta_{EQE} \frac{\alpha_r(\lambda)}{\alpha_r(\lambda) + \alpha_b} \frac{\lambda}{\lambda_f} - 1\right] P_{abs}. \tag{3.6}$$

This equation has three unknown parameters, a, η_{EQE}, and α_b. Experimentally measured values of ΔT at steady state versus wavelength λ were therefore used to find values of η_{EQE} and α_b that yielded the best fit to Eq. (2.4). And the cooling efficiency and cooling power itself can be calculated based on the fit result.

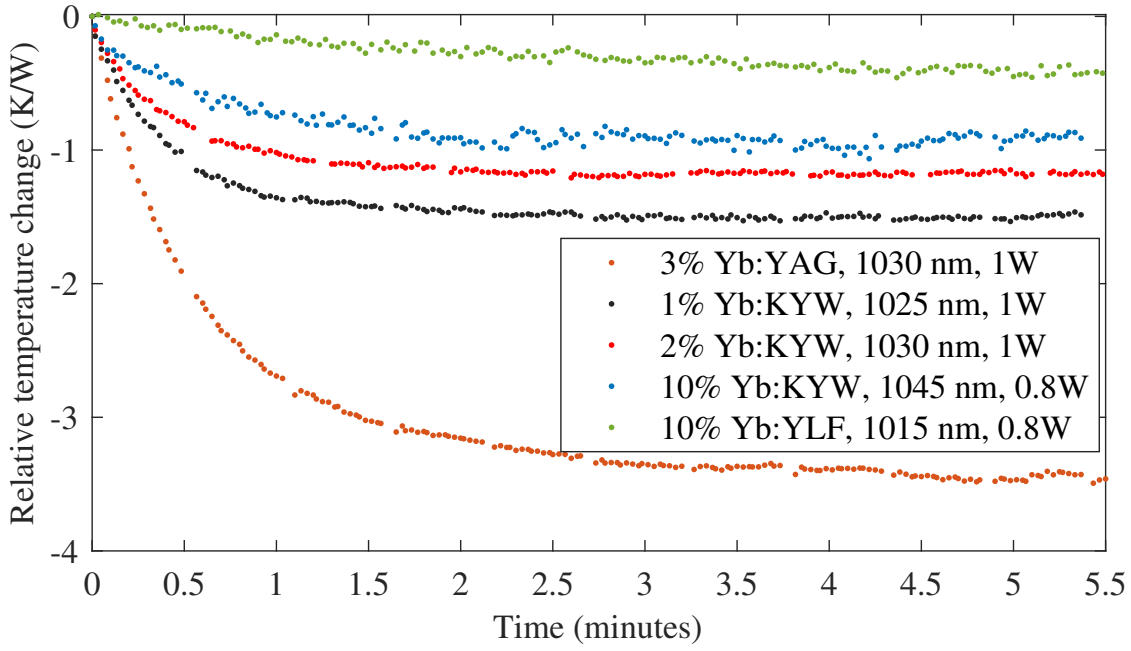

Figure 3.9: Experimental measurements of sample temperature versus time in Yb-doped samples of YAG, KYW, and YLF.

Figure 3.9 shows the measured DLT temperature change results versus time at the optimum wavelength in Yb-doped samples. For small crystals of YAG and KYW with dimensions $1 \times 1 \times 10$ mm^3, it took several minutes for the temperature to reach the steady state, while for larger crystals, Yb:YLF with a volume 10 times larger, the laser induced cooling power needs a much longer time to reach the steady state, as shown in the left hand side of Eq. (3.4). A drift of the lab environment, specifically the room temperature, was observed in these longer time scales, which prevented the accurate temperature measurement for large samples using this steady-state method. In the next subsection, a dynamic method will be introduced to measure the cooling efficiency for large samples.

3.4.3 Dynamic Method

In this section, a dynamic method is introduced to measure the cooling efficiency for large crystals. The dynamic method keeps track of the crystal temperature change versus time and measures the cooling efficiency directly from a linear fit to the dynamic temperature change.

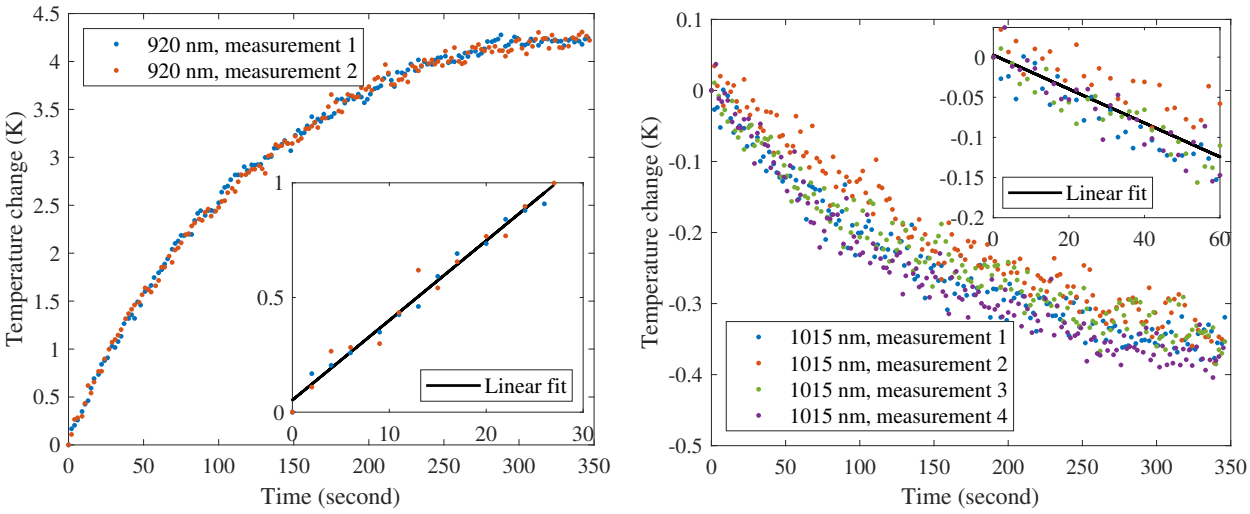

(a) (b)

Figure 3.10: Temperature change versus time in Yb:YLF recorded by DLT at a pump power of 0.8 W. (a) Pumping in the heating range, $\lambda = 920$ nm. The inset shows that during the first thirty seconds while the temperature changed by $\Delta T = 1$ K. The temperature increase was well described by a linear regression with a slope of 3.48×10^{-2} K/s. (b) Pumping in the cooling range, $\lambda = 1015$ nm. The inset shows that during the first sixty seconds. The temperature decrease is well described by a linear regression with a slope of -2.11×10^{-3} K/s.

The heat equation describes the temperature dynamics of the crystal during pumping, hence the cooling efficiency could be calculated based on the measured crystal temperature change versus time. The second and third terms on the right-hand side of Eq. (3.4) depend on how different the sample and environmental temperatures are. For small excursions in temperature the difference between T and T_0 is small. For this reason, the second and third terms of Eq. (3.4) can be neglected when temperature changes are small or times are short. Thermal balance in the crystal is then determined solely by the laser cooling term containing the cooling efficiency η_c. At short times, the cooling rate is linear in time, as seen in Figures 3.10, and is equal to the cooling power. A simple determination of η_c therefore becomes possible from observations of temperature change at short times using

$$\eta_c = {P_{abs}}^{-1} cM \frac{dT}{dt} \tag{3.7}$$

when the absorbed power is known from careful measurements of the incident, reflected, and

transmitted pump power. For Yb:YLF crystal, the specific heat $c = 0.79$ J/g·K [59], and the mass $M = 0.408$ g was determined using a precision balance (QUINTEX213-1S).

For large excursions of temperature from ambient (or at long times), the temperature T differs significantly from T_0. Its dependence on time therefore becomes nonlinear, and Eq. (3.7) ceases to be a valid approximation. In practice, it was found that excellent linear fits were obtained for temperature excursions of $\Delta T < 1$ K or for times less than 1 minute. Consequently, the restriction of data analysis to these conditions furnished simple but accurate determinations of the cooling efficiency at arbitrary wavelengths.

3.5 Pump Locking Technique and Laser Efficiency

The previous section introduced the methods of measuring the cooling power. A radiation-balanced laser (RBL) is operated by equaling the amount of heat generated during lasing to the measured cooling power. In this section, the RBL operation for a single pass setup and the corresponding laser efficiency are discussed, then a pump locking technique (lock the laser cavity to the pump wavelength) is introduced, which enhances the laser efficiency and reduces the required pump intensity at the radiation-balanced condition (RBC).

3.5.1 Single Passed Pump

In this subsection, the output laser intensity and laser efficiency of RBL for 3% Yb:YAG are discussed with the pump passing once through the crystal.

Figure 3.11a plots the intracavity laser intensity versus pump intensity, with the pump passing once through the crystal for 3% Yb:YAG. The pump and laser wavelengths are 1029.3 nm and 1048 nm, respectively. The background color is the calculated thermal intensity and the red curve indicates the radiation-balanced condition (RBC) where the thermal intensity is zero. Other colored lines give the relations between the intracavity laser intensity and pump intensity with various reflectances of the output coupler labeled in legend. The lines for small output couplers are shifted to the right because it requires a higher input intensity to reach the laser threshold. The intersection between the red curve and colored line indicates the laser is operated at RBC, i.e. lasing without heating. To calculate the output laser power, the intracavity laser intensities are multiplied by the corresponding transmittances of the output couplers. Fig. (3.11b) plots the output laser intensity versus pump intensity, which is obtained by shrinking the intracavity laser intensity plot (Fig. 3.11a) in the y-direction with a pump dependent shrinking ratio. The left part is not colored because the gain is lower than the cavity loss, and there is no output laser light at low pump intensities. The top left region in the original intracavity laser intensity plot has a transmittance value close

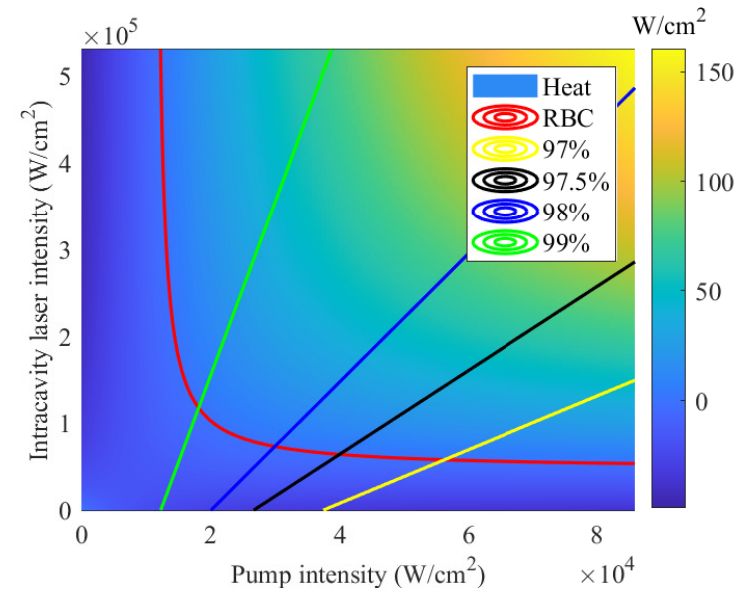

(a)

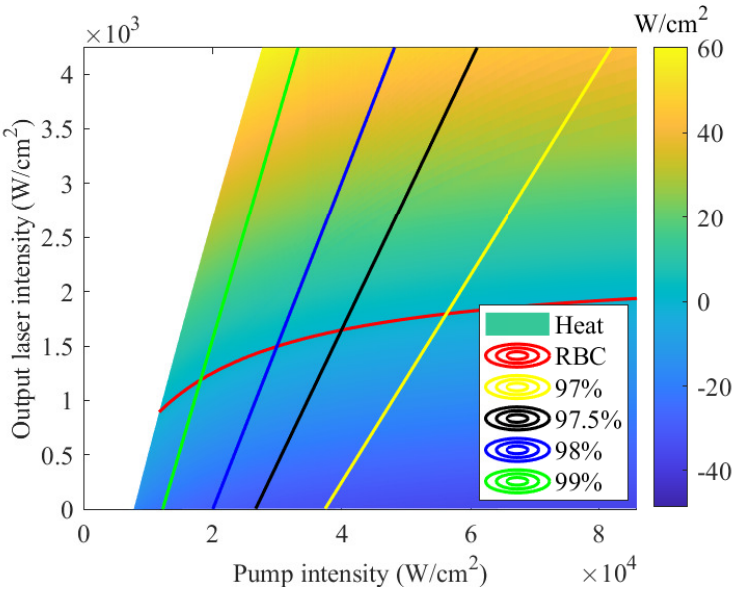

(b)

Figure 3.11: (a) Intracavity and (b) output laser intensity versus pump intensity for 3% Yb:YAG, with the pump passing once through the crystal. The background color is the calculated thermal intensity. The red curve indicates the RBC where the thermal intensity is zero. The green, blue, black and yellow curves give the relations between the laser intensity and pump intensity with the reflectance of the output couplers labeled in legend. The background absorption coefficient was 2×10^{-4} cm^{-1} (Table 4.1) and remaining parameters are same as that of Fig. 2.10.

to zero, which leads to a small output laser intensity, even though there are intense intracavity intensities. The left part is shrunk more than the right, bending the red RBC curve down at low

pump intensities. Below the threshold, increasing the pump intensity along the x-axis increases the cooling power in the crystal (blue background color). Once the gain induced by the pump equals the cavity loss (output coupler), the laser light starts to oscillate inside the cavity. Then, increasing the pump intensity, for example, along the black curve for 97.5% output coupler, increases the output laser intensity, generating more heat in the lasing cycle and increasing the thermal intensity inside the crystal. At a specific pump intensity, the cooling turns to heating and this critical point indicates zero thermal intensity in the crystal, which falls on the red RBC curve.

In Fig. 3.11b, for the colored laser output intensity versus pump intensity lines, the intersections with the x-axis indicates the threshold and the intersections with the red RBL curve indicates the radiation-balanced operation. When the reflectance of the output coupler is 97.5%, the laser reaches the threshold with a pump intensity of 2.7×10^4 W/cm^2, and at balanced condition, the output laser intensity is 1.6×10^3 W/cm^2 with a pump intensity of 4.0×10^4 W/cm^2. Recall that the 3% Yb:YAG crystal has a dimension $1 \times 1 \times 10$ mm^3. If the pump and laser beams fill the full 1×1 mm^2 cross section, then the required pump power at the threshold power is 270 W, and the radiation-balanced operation needs a pump power of 400 W. Hence, the beam size inside the crystal needs to be confined in order to fulfill the required intensity with limited pump power. The geometry design of the laser cavity is covered in Subsection 3.6.1.

Assuming that the pump and laser lights have the same beam radius, the laser efficiency at the radiation-balanced operation is 4% for the 97.5% output coupler with the pump passing once through the crystal. The laser efficiency at radiation-balanced operation, defined as the ratio of output laser power to pump power, is equal to the slope of a straight line through the origin and the intersection point on the red RBC curve for various output coupler reflectances. The laser efficiency decreased with decreasing the reflectance of the output coupler. The highest laser efficiency is calculated to be 7.6 % with a 99.9% output coupler for 3% Yb:YAG crystal. In other words, the laser efficiency cannot exceed 7.6% at RBC for 3% Yb:YAG with a crystal geometry of $1 \times 1 \times 10$ mm^3, when the pump and laser wavelengths are 1029.3 nm and 1048 nm, respectively.

The theoretical maximum laser efficiency at RBC, when the background absorption is ignored, can be derived by setting Eq.(2.31) to zero, then the laser efficiency is

$$\eta_E = \frac{-I_l \alpha_l(I_p, I_l)}{I_p \alpha_p(I_p, I_l)} = \frac{\eta_{EQE}\lambda_p - \lambda_f}{\eta_{EQE}\lambda_l - \lambda_f}. \tag{3.8}$$

This equation shows that the laser efficiency increases when reducing the separation between the pump and laser wavelengths. When the pump and laser wavelengths are corresponding to the E3-E5 and E5-E4 transitions (Fig. 2.5), the theoretical maximum laser efficiencies are 35.0% for the 3% Yb:YAG ($\lambda_p = 1029.3$ nm, $\lambda_l = 1048$ nm, $\lambda_f = 1012.1$ nm, and $\eta_{EQE} = 0.993$). The calculated efficiency for the pump passing once through the crystal is much lower than the theoretical

limit. That's because RBLs need a high intensity to maintain saturation, but the absorption is small due to the saturation. For example, only 12.5% of the pump is absorbed in the radiation-balanced operation for the 97.5% output coupler, and the optical-to-optical conversion efficiency is actually 32.5%, which is much higher than the 4% laser efficiency. The majority part of the pump, used to maintain saturation, is not absorbed by the laser medium. The laser efficiency can be increased by enhancing the absorption of the pump power. Bowman achieved a 19% laser efficiency [8] at RBC using a 120 mm long Yb:YAG rod with the pump passing once through the crystal, where the absorption was enhanced with the long crystal length. Yang enhanced the absorption by placing the 0.5 mm Yb:YAG disk inside a vertical external-cavity surface-emitting laser (VECSEL) cavity and achieved a 15% optical-to-optical conversion efficiency [9] at RBC. However, the presence of the VECSEL cavity required an additional pump to maintain lasing for another laser cavity, and the overall laser efficiency was 1.8%. A pump locking technique will be introduced in Subsection 3.5.3, where the laser efficiency is boosted to the optical-to-optical conversion efficiency by a total absorption of the input pump power.

Besides the low laser efficiency, introducing the pump into the laser cavity is another issue for RBLs. For a standard laser cavity, the input mirror has zero reflectance at the pump wavelength to transmit the pump light to the cavity and a close to unity reflectance at the laser wavelength to reflect the oscillating laser light. Similarly, a zero reflectance at the pump wavelength, 1029.3 nm for Yb:YAG, is desired to transmit all of the pump power into the crystal, and the small saturated gain of the laser medium at RBC requires a close to unity reflectance at the laser wavelength, 1048 nm for Yb:YAG, to achieve lasing. The input mirrors need to have a reflectance that turns from zero reflection to total reflection in a $\sim$20 nm wavelength range, which is too difficult to be achieved. Due to the feature of small separation between the pump and laser wavelength, the spatial separation between pump and laser beams was used to introduce the pump in current RBLs. Bowman used a pump injection mirror with a 3 mm hole in the center to introduce the pump to from the mirror and transmit the laser through the hole [8]. Yang used an additional cavity that was tilted from the RBL cavity to introduce the pump [9]. Both methods introduced a mode-mismatch between the pump and laser, which further reduces the laser efficiency. In Subsection 3.5.4, a mode-matched pump locking cavity is presented to introduce the pump using spectral separation instead of spatial separation, where the pump and laser light are both oscillating in the same cavity.

3.5.2 Pump Locked Cavity without Lasing

For a pump locking technique, the crystal is placed in a laser cavity, and the cavity is locked to the pump. Then both the pump and laser light oscillate in the cavity. For the previous single-pass setup, the output laser intensity was obtained by shrinking the intracavity plot in the y-direction.

Similarly, to analyze the output laser intensity versus input pump intensity, the intracavity plot needs to be shrunk in the x-direction, according to the relation between intracavity pump intensity and input pump intensity. In this section, this relation is discussed in the absence of lasing light.

For a resonant cavity, the intercavity intensity $I_{p,intra}$ and reflected intensity $I_{p,ref}$ can be calculated from the input intensity $I_{p,in}$ according to

$$I_{p,intra} = \frac{1 - R_i}{\left(1 - \sqrt{R_i e^{-\alpha L}}\right)^2} I_{p,in} \tag{3.9}$$

$$I_{p,ref} = \left(\frac{\sqrt{R_i} - \sqrt{e^{-\alpha L}}}{1 - \sqrt{R_i e^{-\alpha L}}} \right)^2 I_{p,in}, \tag{3.10}$$

where R_i and L are the reflectance of the input coupler and the crystal length, respectively. α is the absorption coefficient at the pump wavelength, Eq. (2.43), which depends on both the pump and laser intracavity intensities. In this subsection, the intracavity laser intensity is assumed to be zero for the absorption coefficient α ($I_l = 0$ in Eq. 2.43).

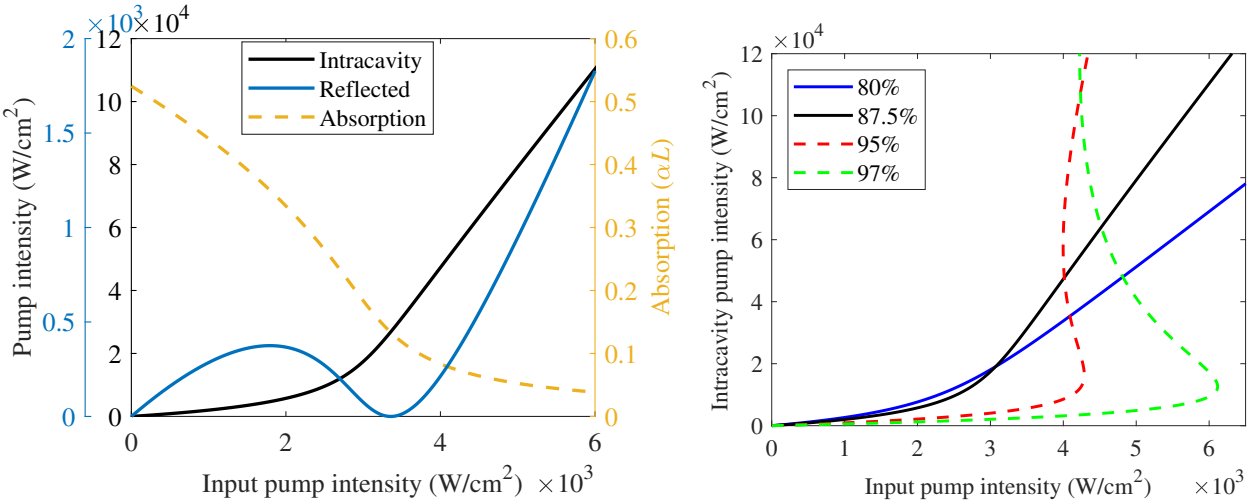

Figure 3.12: (a) The intracavity (black) and reflected (blue) pump intensity, together with the absorption of the pump (yellow), versus input pump intensity for 87.5% reflectance of the input coupler. (b) Intracavity pump intensity versus input pump intensity with reflectance of input couplers labeled in the legend for 3% Yb:YAG. The laser intensity is assumed to be zero ($I_l = 0$) in Eq. 2.43.

Figure 3.12a plots the intracavity pump intensity versus input pump intensity with an assumed input coupler reflectance of 87.5% for 3% Yb:YAG according to Eq. (3.9). The blue and yellows curves plot the reflected pump intensity from the input coupler, Eq.(3.10), and the absorption of

the pump light by the crystal, Eq. (2.43) with $I_l = 0$. The black curve shows the intracavity pump intensity, which is amplified by the resonance cavity. The intracavity intensity increases with increasing the input pump intensity, but the relation is nonlinear. The intracavity intensity depends on both the input intensity and the amplification ratio, which relates to the difference between the transmittance of the input coupler and intensity-dependent absorption. The absorption (dashed yellow curve) decreases with an increase in intracavity intensity, and at a critical intracavity intensity, the absorption equals to the transmittance of the input coupler, leading to an impedance-matched cavity [60]. The impedance-matched cavity has the strongest interference effect, which leads to the highest amplification ratio for the intracavity intensity and a zero reflection because of the constructive and destructive interference, respectively. The reflected pump intensity from the input coupler is plotted in blue, and it vanishes at the impedance-matched condition. Close to the impedance-matched intensity, the strong interference effect causes a rapid change in the amplification ratio and induces a strong nonlinearity between the intracavity intensity and input pump intensity. One thing to note is that at the impedance-matched intensity, since there is no reflection, all of the pump is absorbed by the crystal, which means a total absorption of the input pump intensity. This feature will be used to enhance the laser efficiency of RBLs in Subsection 3.5.3.

Fig. 3.12b shows the relations of intracavity pump intensity versus input pump intensity for 3% Yb:YAG with various input coupler reflectivities. All the curves show the nonlinearity. What's more, the curve swings back with the increase of input pump intensity for a reflectance of input coupler higher than 95% (dashed curves), leading to a bistable cavity [61]. Normally, the bistable cavity should be avoided because the laser threshold may fall into the bistability region, as will be shown in Subsection 3.5.3 shortly.

3.5.3 Pump Locked Cavity with Lasing

The analysis in the previous subsection excluded the laser light and showed that total absorption can be achieved in an impedance-matched cavity at one specific input intensity. In this section, the analysis includes laser light and shows that the impedance-match operation achieved at the threshold is independent of input intensity, meaning that the total absorption is always maintained during lasing.

Fig. 3.13a shows the intracavity pump intensity versus input pump intensity for 3% Yb:YAG with 87.5% reflectance for the input coupler according to Eq.(3.9) and Eq.(2.43). The dashed black curve is plotted without the laser light inside the cavity ($I_l = 0$ in Eq.(2.43)), which is the same as the black curves in Fig. 3.12. The solid green, black and yellow lines indicate the relations in presence of the laser light inside the cavity, with a 96.5%, 97.5%, and 98.5% reflectance for the output couplers. The intersection between the dashed black curve and the solid line indicates

the laser threshold. The lines corresponding to a lower reflectance for output couplers are located higher because they require a higher intracavity (input) pump intensity at the threshold. The background color plots the thermal intensity, and the red curve indicates the radiation-balanced condition (RBC). The intracavity pump intensity increases with the increase of input pump intensity along the dashed black curve below the threshold. When the gain for the laser light equals the cavity loss (transmittance of the output coupler), the laser starts to oscillate inside the cavity. Then the intracavity pump intensity follows the back solid lines (for example, 97.5% reflectance for the output coupler) with further increase of input pump intensity. Along the black line, the thermal intensity turns from cooling to heating at a critical intensity (red curve), which means the laser is operated at RBC, lasing without heating.

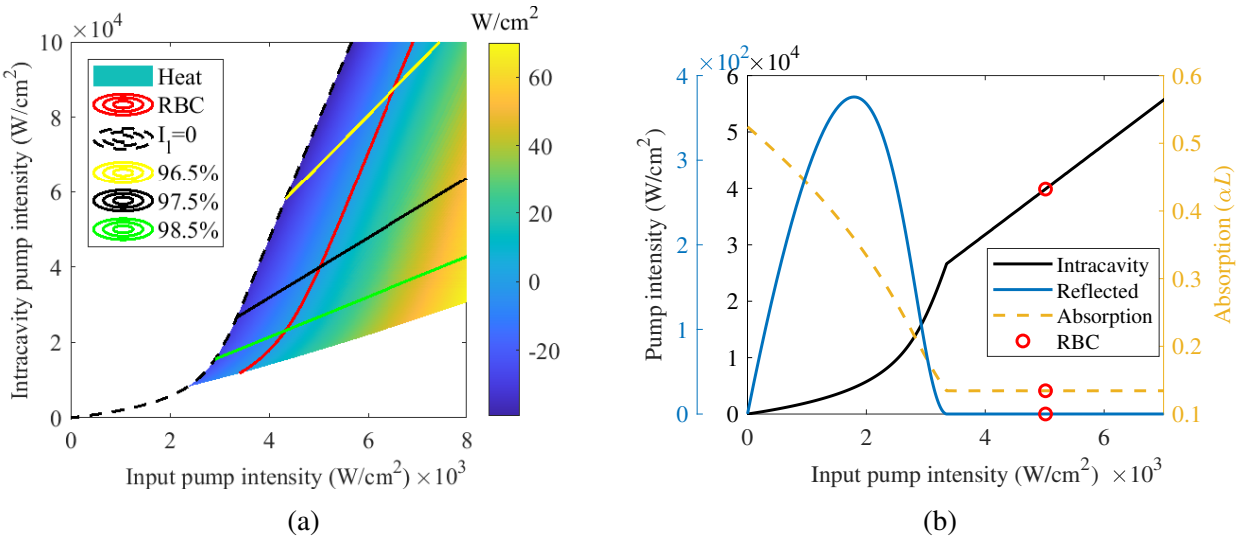

Figure 3.13: (a) The intracavity pump intensity versus input pump intensity with 87.5% reflectance of input coupler for 3% Yb:YAG. The dashed black line plots the relation in absence of the laser light. The yellow, black, and green lines plot the relations in presence of the laser light with various output couplers labeled in the legend. The background color plots the corresponding thermal intensity, and the red curve indicates the RBC. (b) The intracavity (black) and reflected (blue) pump intensity, together with the absorption of the pump (yellow), versus input pump intensity for 87.5% and 97.5% reflectance of the input and output couplers. The red circles indicate the radiation-balanced condition.

Figure 3.13b details this process by including the reflected pump intensity, Eq.(3.9), and crystal absorption, Eq. (2.43), for 87.5% input coupler and 97.5% output coupler. The black curve shows the relation between the intracavity intensity and pump intensity (Eq. 3.9), with the red circles indicating the RBC. In absence of lasing, this relation is nonliear as plotted in Fig. 3.12a. However, the relation becomes linear when the input pump intensity reaches the laser threshold in presence of the laser light. Similarly, the absorption of the pump, after initial decreasing, is not further

reduced when the pump intensity increases above the threshold. At the threshold, the gain at the laser wavelength equals the cavity loss (transmittance of the output coupler). The cavity loss is a constant, which means the gain is also a constant even with a further increase in the input pump intensity. The intensity-independent gain leads to an intensity-independent absorption because they are both dependent on the population difference between the ground state and excited state. Below the laser threshold, the saturable absorption of the pump (yellow curve) decreases with increasing the pump power, which comes from the reduced electron population in the ground state limited by the spontaneous decay rate from the excited state. At the threshold, the stimulated emission at laser wavelength shows up, increasing the decay rate from the excited state, and the absorption of the pump is locked to a constant value, independent of the input pump intensity. The dashed yellow curve is flat after the threshold, which means the amplification ratio of the intracavity pump intensity is constant, leading to a linear increase with the input pump intensity. As mentioned above, when the transmittance of the input coupler equals the cavity loss, an impedance-matched cavity is maintained, and total absorption is achieved. In absence of the laser light, the impedance-matched cavity can only be achieved at one specific input pump intensity. If we can lock the absorption of the pump to a value the same as the transmittance of the input coupler, the cavity is always an impedance-matched cavity during lasing, independent of the input pump intensity. Then the total absorption is maintained during lasing. Fig. 3.13b is an impedance-matched cavity during lasing for 3% Yb:YAG, with 87.5% input coupler and 97.5% output coupler. The blue curve plots the reflected pump intensity for an impedance-matched cavity, and it remains zero after reaching the threshold. This demonstrates the total absorption during lasing, enhancing the laser efficiency. As presented in Subsection 3.5.1, the laser efficiency is 4% for 97.5% output coupler at RBC with a pump intensity of 4×10^4 W/cm^2 for a single pass setup. By introducing a 87.5% input coupler with pump locking technique, the laser efficiency is boosted to 32.5% with a reduced input intensity of 5×10^3 W/cm^2. The laser efficiency is 8 times higher, while the required input intensity is 8 times lower. This technique not only dramatically increased the laser efficiency at radiation-balanced operation but also significantly reduces the required input intensity to reach RBC.

Experimentally, when the output coupler is selected, the ideal input coupler is supposed to have a transmittance that is the same as the absorption of the pump at the threshold to maximize the laser efficiency. However, a perfect impedance-matched cavity is hard to achieve due to the uncertainties in the mirror reflectivity. Figure 3.14 plots the intracavity (black) and reflected (blue) pump intensity, together with the absorption of the pump (yellow), versus input pump intensity for close to an impedance-matched cavity. The input coupler has a reflectance of 87.5%, and the output couplers are 96.5% for Fig. 3.14a and 98.5% for Fig. 3.14b. Similarly, the relation between intracavity pump intensity and input pump intensity is linear after the threshold, as explained above. However, the reflected input intensity does not vanish during lasing. The locked absorption value

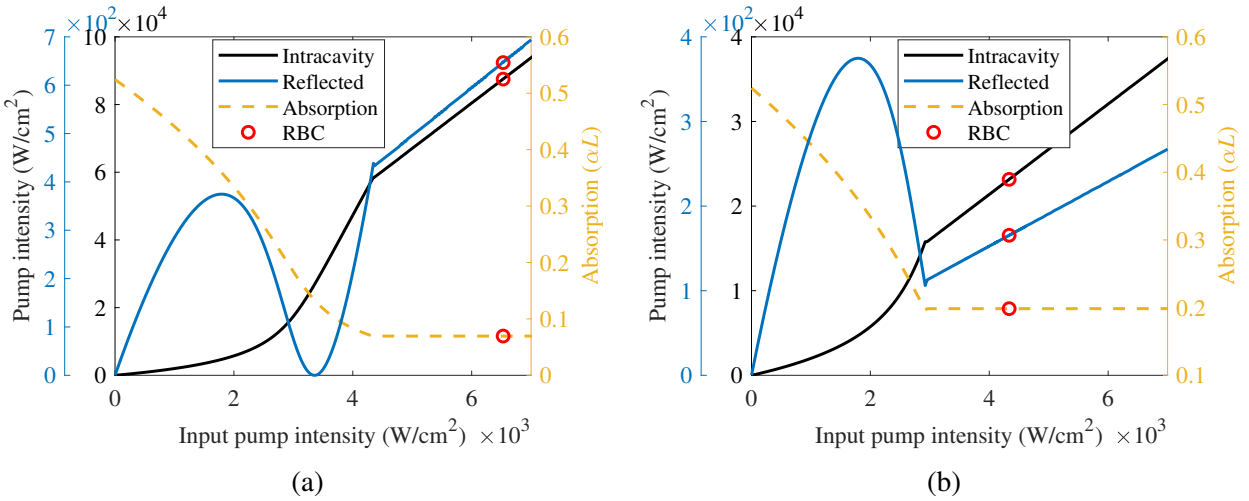

Figure 3.14: The intracavity (black) and reflected (blue) pump intensity, together with the absorption of the pump (yellow), versus input pump intensity for 87.5% reflectance of the input coupler. The reflectance of the output coupler is (a) 96.5% and (b) 98.5%. The red circles indicate the radiation-balanced condition.

for the 96.5% (98.5%) output coupler is lower (higher) than the transmittance of the 87.5% input coupler. This mismatch only leads to a 0.7% (1%) reflection during lasing. Though the total absorption is not achieved, the overall laser efficiency is still more than 30%, which is much higher than the 4% of the single pass setup. A detailed analysis of laser efficiency at RBC with various reflectance of input and output couplers is presented in Subsection 3.5.4, which provides guidance for selecting the input and output couplers.

The analysis above presents the relations between the intracavity pump intensity and input pump intensity for 87.5% input coupler. As plotted in Fig. 3.12b, different input couplers have different relations, and the cavity can be bistable with the high reflectance of the input coupler. Fig. 3.15a plots the intracavity pump intensity versus the input pump intensity for 80% input coupler. It has a similar shape to the 87.5%, along the dashed black curve before the laser threshold and along the black curve (for 97.5% output coupler) after the laser threshold with increasing the input pump intensity. If the relation is monotonic, it has a similar dependency. Fig. 3.15b plots the intracavity pump intensity versus the input pump intensity for a 95% input coupler. The threshold for a 97.5% output coupler (the intersection between the dashed black curve and solid black line) falls in the bistable range. This laser threshold cannot be arrived at by simply increasing the input pump intensity because the intracavity pump intensity will jump up when the input pump intensity is increased to $\sim 4.3 \times 10^3$ W/cm^2. The high reflection of the input coupler leads to a bistable cavity which should be avoided when selecting the input couplers.

In summary, the pump locking technique locks the laser cavity to the pump, and both the pump

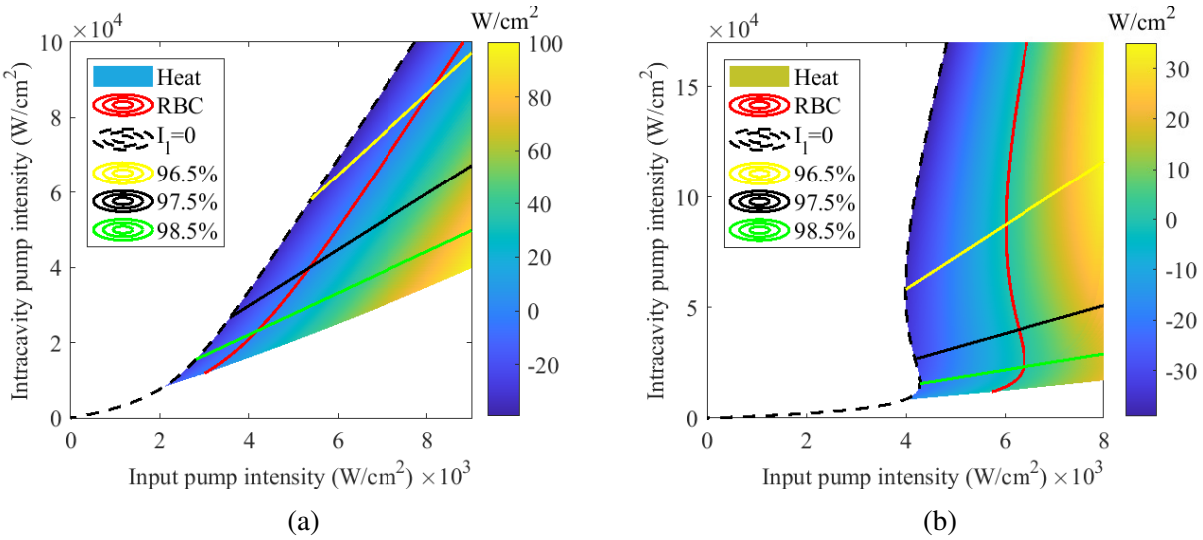

Figure 3.15: The intracavity pump intensity versus input pump intensity with (a) 80% and (b) 95% reflectance of input coupler for 3% Yb:YAG. The dashed black line plots the relation in the absence of the laser light. The yellow, black, and green lines plot the relations in presence of the laser light with various output couplers labeled in the legend. The background color plots the corresponding thermal intensity, and the red curve indicates the RBC.

and laser lights are oscillating in the same cavity. This pump-locked cavity enhances the laser efficiency and reduced the required input pump intensity at radiation-balanced operation.

3.5.4 Laser Operation and Laser Efficiency

The previous sections discussed the relationship between intracavity pump intensity and input pump intensity. This relation is used to obtain the output laser intensity versus input pump power in this section by shrinking the intracavity intensity plot in the x-direction, converting the intracavity pump intensity to input pump intensity. What's more, the laser efficiency at the RBC is analyzed with various reflectances of input and output couplers.

Fig. 3.16 plots the output laser intensity versus input pump intensity for 3% Yb:YAG with 87.5% input coupler. The black line is plotted with an output coupler of 97.5%. The input pump intensity at threshold is $\sim 3.4 \times 10^3$ W/cm^2, and the laser efficiency is 32.5% at RBC with an input pump intensity of $\sim 5.0 \times 10^3$ W/cm^2 for the 97.5% output coupler. Recall that for the 87.5% input coupler, the 97.5% output coupler makes the cavity impedance-matched, and the efficiency is maximized. This can also be seen in Fig. 3.16. The laser efficiency for various output couplers is equal to the slope of the straight line through the origin and the intersections between the red curve and the colored line. The highest laser efficiency is achieved when the line just touches the red RBC curve, where the output coupler is exactly 97.5%.

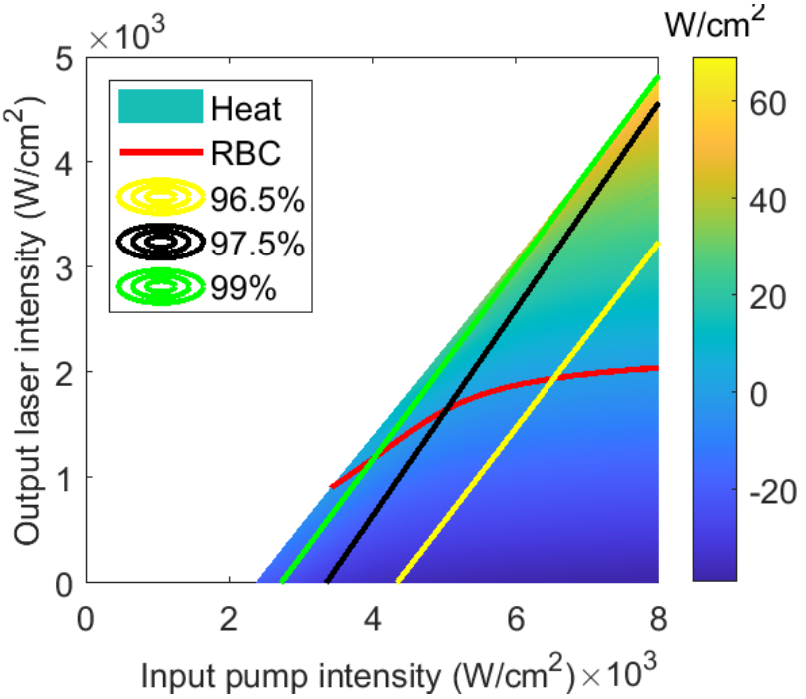

Figure 3.16: Output laser intensity versus input pump intensity for 3% Yb:YAG with an 87.5% reflectance of input coupler. The background color is the calculated thermal intensity. The red curve indicates the RBC where the thermal intensity is zero. The green, black, and yellow lines show the relations between the output laser intensity and input pump intensity, with the reflectance of the output couplers labeled in the legend. The background absorption coefficient and impurity saturation intensity are 2×10^{-4} cm^{-1} and 2×10^{4} W/cm^2. The other parameters are the same as that of Fig. 2.6.

The input coupler for Fig. 3.16 is 87.5%. A different value of the input coupler will lead to a different shrinking ratio (relation between intracavity pump intensity and input pump intensity) in the x direction, and the Fig. 3.16 will be different. Figure 3.17 plot the laser efficiency at RBC for various input and output couplers, which can be used to compare the laser performance with different combinations of input and output couplers. The color indicates the laser efficiency at radiation-balanced operation, with a maximum value of 33% in this plot. Recall the theoretical maximum laser efficiency for 3% Yb:YAG in absence of background absorption is 35% (Eq. 3.8). The difference is induced by the background absorption. As discussed in Subsection 2.4.2, the presence of background absorption requires additional pump power to generate more cooling power in order to compensate for the parasitic heating at radiation-balanced operation, which reduces the laser efficiency. For the input coupler, the reflectance higher than 95% is not calculated because the cavity is a bistable cavity in that range, which should be avoided when selecting the reflectance of input couplers. For the output coupler, the reflectance lower than 96% is not calculated because that range required an ultra-high input pump intensity to reach the threshold (intracavity

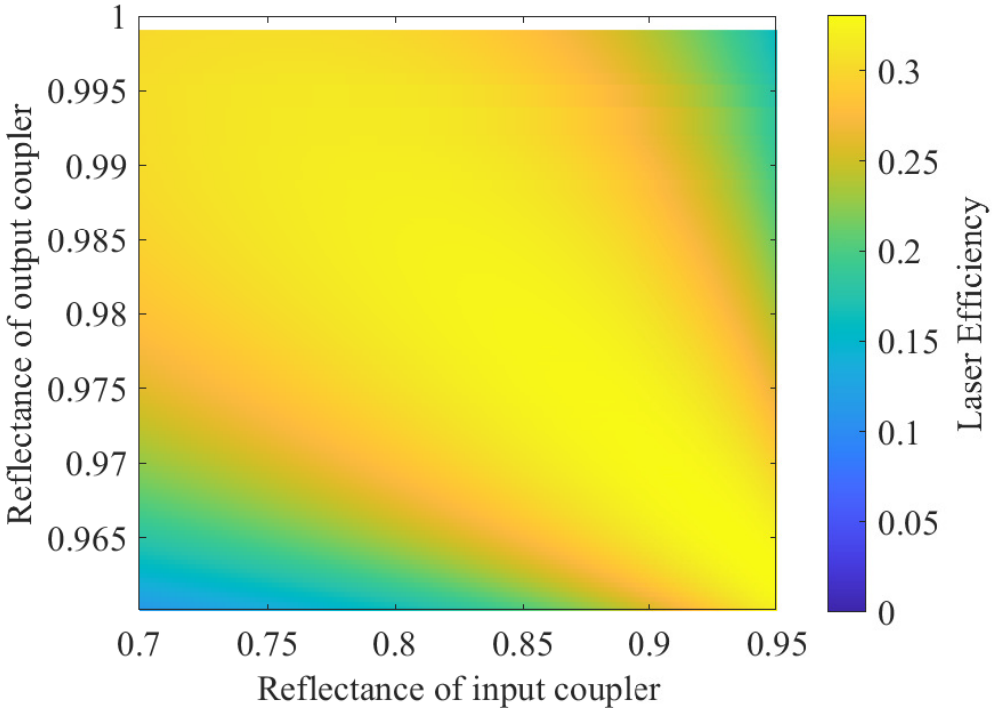

Figure 3.17: Laser efficiency at RBC versus the reflectance of input and output couplers. The maximum laser efficiency in this figure is 33%. The background absorption coefficient is 2×10^{-4} cm^{-1}. The other parameters are the same as that of Fig. 2.10.

pump intensity is 20 times the saturation intensity), and the laser efficiency is low. This figure shows the robustness of the pump locking technique since an efficiency of more than 30% can be achieved within a large region of the reflectivities. This efficiency plot provides guidance in selecting the reflectance for input and output couplers. The yellow region is preferred because it has a high laser efficiency, and near-total absorption is achieved due to the impedance-matched cavity.

Another thing to note is that this figure is for 3% Yb:YAG with a dimension of $1 \times 1 \times 10$ mm^3. The small gain leads to a tighter restriction for the output coupler. With a heavily doped crystal or a long crystal, the gain will be enhanced, and it will lose the restrictions placed on the output coupler. For example, Bowman used a 120 mm Yb:YAG rod, and lasing was observed with an 80% output coupler [8]. In that case, the maximized laser efficiency can be achieved with a reflectance that is the same for both the input and output coupler. Then, a mirror with a flat spectral reflectivity at 1029.3 nm (pump) and 1048 nm (laser) can be used as both the input coupler and output coupler. Even with this 3% Yb:YAG crystal, one mirror with 97.5% reflectivity at 1029.3 nm pump and 87.5% reflectance at 1048 nm laser can be used as both input and output coupler. The 10% reflectivity difference in $\sim$ 20 nm range is feasible, and it introduces the pump into the cavity with the spectral separation. This pump-locking technique ensures a mode match between

the pump and laser since they are oscillating in the same cavity. In summary, this pump-locked cavity simplifies the alignment and dramatically increases the laser efficiency by a total absorption of the pump power and an increased mode match between pump and laser. In addition, since the pump is also oscillating inside the cavity, this technique reduced the required input intensity to achieve a RBL.

3.6 Radiation-Balanced Laser Design

The previous section introduced a pump-locked cavity and plotted the laser efficiency at RBL for various input and output couplers. In this section, the geometric cavity design, coupler selection, and experimental setup of RBLs are presented. What's more, the processes to design the RBLs are summarized in the end.

3.6.1 Cavity Design

In this subsection, the geometry cavity design of a four-mirror ring cavity for use in demonstrating a radiation-balanced laser is discussed. As presented in Section 2.3, the RBL has a small gain in the laser medium because of saturation; therefore, the overall cavity loss needs to be controlled when designing the cavity. In terms of the crystal, a Brewster angle cut or anti-reflection coating at the ends is desired. However, because of the high intracavity intensities, heating near the ends of the crystal due to absorption in the anti-reflection coatings was observed in Bowman's RBL experiment [8]. Hence, Brewster-cut crystals were used in this work.

However, the Brewster angle introduced an astigmatism aberration in the cavity, leading to a mismatch between the elliptical oscillating cavity mode and the input circular Gaussian pump beam. A four-mirror ring cavity was used to compensate for the aberration, and Fig. 3.18 shows the layout of the cavity for the 3% Yb:YAG crystal. M1 and M2 are two curved mirrors ($R = 100$ mm). M3 and M4 are flat mirrors. The $l1$ is the distance between the crystal and the curved mirror. $l2$ is the path length from M2 to M1 through M3 and M4.

The purpose of the astigmatic compensation is to produce a maximum overlap of the x- and y-stability ranges, which leads to equal mode characteristics in x and y [62] directions. The mode match increases the coupling between the cavity mode and circular input pump beam, which further enhanced the laser efficiency. Fig. 3.19 plots the stability range [63] for Yb:YAG and Yb:KYW crystals based on the ABCD matrix of this ring laser cavity. The calculated maximum overlap is found to be (a) $l1 = 5.45$ cm with 9.89° angle of incidence for Yb:YAG and (b) $l1 = 5.47$ cm with 9.75° angle of incidence for Yb:KYW.

Figure 3.20 plots the beam waist inside the Yb:YAG and Yb:KYW crystals in x and y directions

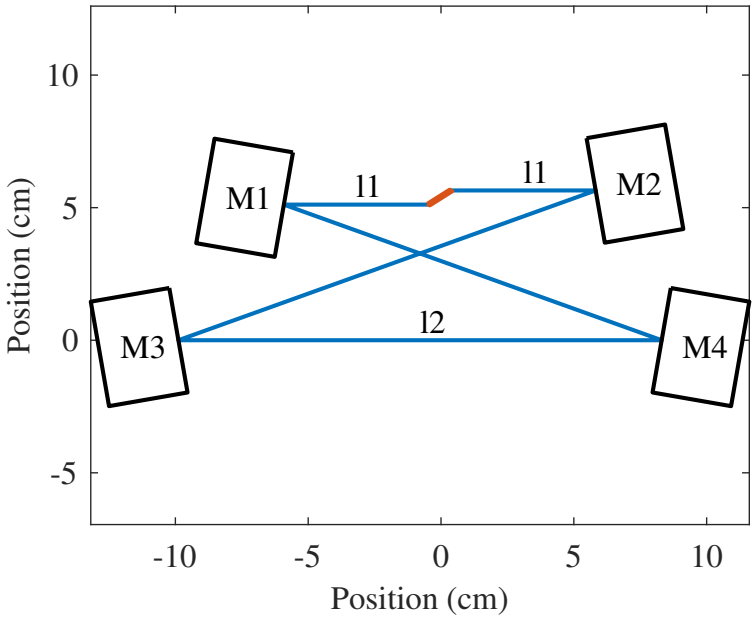

Figure 3.18: Four mirror ring cavity for 3% Yb:YAG crystal (red). M1 and M2 are curved mirrors ($R = 100$ mm). M3 and M4 are flat mirrors. $l1 = 5.45$ cm is the separation distance between the crystal and the curved mirror. $l2 = 50$ cm is the path length from M2 to M1, through M3 and M4. The angle of incident for M1 and M2 is $9.89°$.

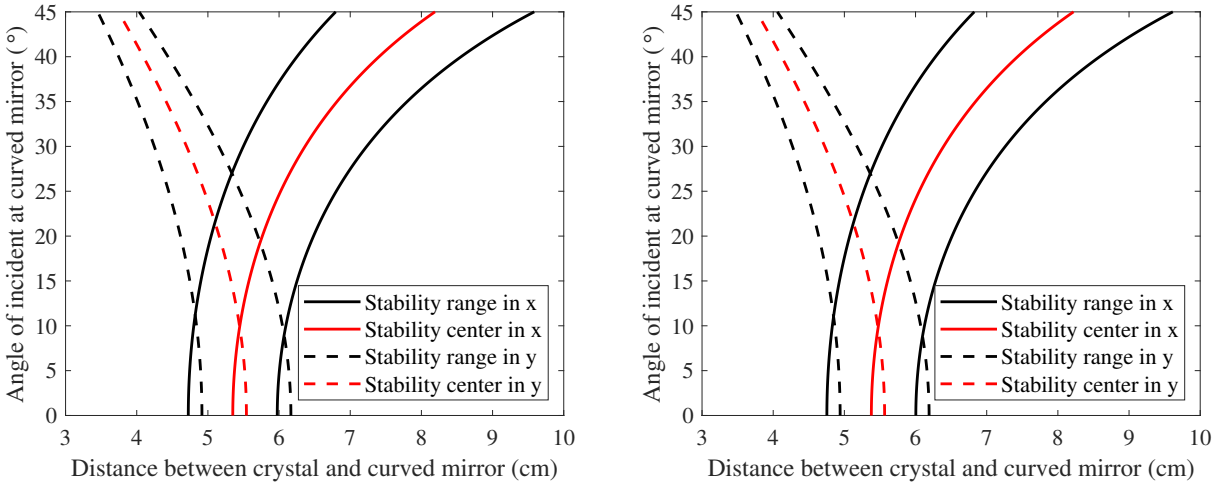

Figure 3.19: Cavity stability range at different angles of incidence for the curved mirror, and $l1$ separation distance between crystal and curved mirror, for (a) 3 % Yb:YAG and (b) 2% Yb:KYW. $l2 = 50$ cm for both plots. The solid curves are in the x-direction, and the dashed curves are in the y-direction. The black curves are the boundary of the stability range, and the red curves are the center. The maximum overlap is found to be (a) $l1 = 5.45$ cm with 9.89° angle of incidence for Yb:YAG and (b) $l1 = 5.47$ cm with 9.75° angle of incidence for Yb:KYW.

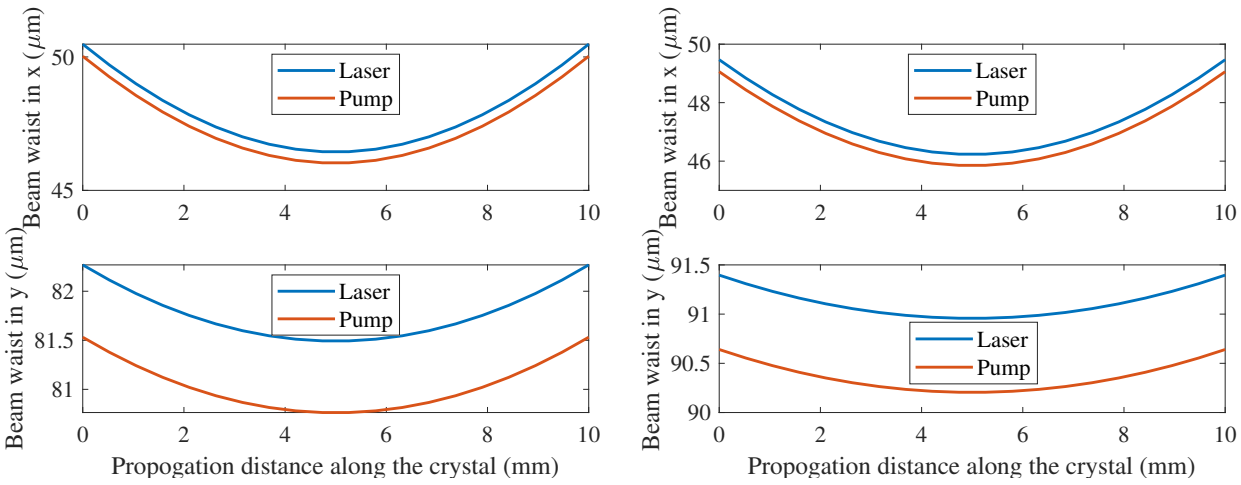

Figure 3.20: Beam waist inside (a) 3 % Yb:YAG and (b) 2% Yb:KYW in x- and y-directions when the astigmatism is compensated. The red curves are the pump beam waist at (a) 1029.3 nm and (b) 1022.5 nm. The blue curves are the laser beam waist at (a) 1048.0 nm and (b) 1039.6 nm.

when the astigmatism is compensated. The beam waists are $\omega_x \approx 47\mu$m, $\omega_y \approx 81\mu$m for Yb:YAG and $\omega_x \approx 47\mu$m, $\omega_y \approx 91\mu$m for Yb:KYW. The beam waist inside the crystal in the y-direction is larger than the x-direction, which is induced by the Brewster angle. When the cavity was aligned, the beam waist at the position of the crystal was measured using the knife-edge technique [64] with a razor blade, and the results are plotted in Fig. 3.21. The transmittance of the pump is measured with the beam blocked by inserting the razor blade. The fitted beam waist is 51.8 μm for Yb:YAG cavity at 1030 nm and 54.4 μm for Yb:KYW cavity at 1022.5 nm, which are close to the designed beam waists. The small deviation may come from the uncertainties of the mirror positions. The agreement shows a good coupling between the input pump mode and intracavity mode. The confined beam size inside the crystal ensures the required high intensities at the radiation-balanced condition with low input power.

In summary, the geometric cavity design ensures not only the compensation of the astigmatic abbreviation induced by the Brewster angles but the saturation condition with low input power by limiting the beam area across the laser medium. What's more, the laser efficiency is also enhanced by increasing the mode match between the input pump mode and oscillating cavity mode.

3.6.2 Cavity Mirror Selection

The previous subsection presented the four mirror ring cavity for demonstrating RBLs. In this section, the mirror reflectivity is discussed for designing the Yb:YAG and Yb:KYW RBLs.

In this work, the flat mirror M3 plotted in Fig. 3.18 was selected to be both the input coupler and

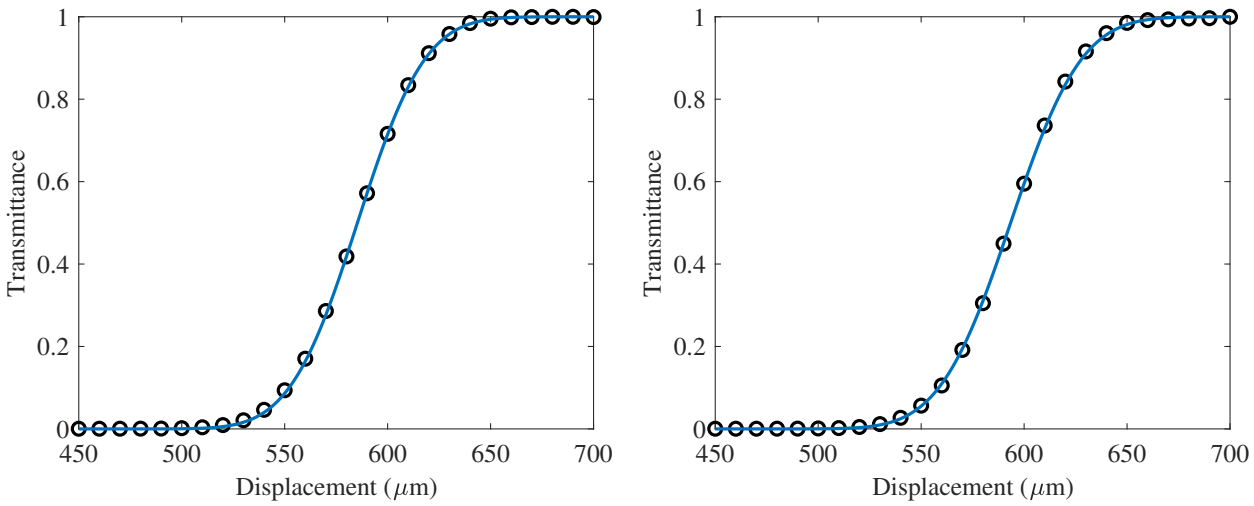

Figure 3.21: Measured transmission of pump beam at the position of the crystal when the cavity is aligned for (a) 3 % Yb:YAG and (b) 2% Yb:KYW crystals. The circles are experimentally measured transmittance, and the solid curve is the fitting of the experimental data. The fitted beam waists were (a) 51.8 μm and (b) 54.4 μm.

output coupler, and the other three mirrors (M2, M3, and M4) were coated with an anti-reflection coating (R$>$ 99.995%, 10° angle of incidence). Fig. 3.22 plots the laser efficiency at RBC for 3% Yb:YAG versus the mirror reflectivity at 1029.3 nm pump and 1048 nm laser wavelength. Unlike the previous efficiency plot in Subsection 3.5.4, this figure includes the loss introduced by the other three mirrors. The selection of the reflectivity for M1 is based on this plot. In principle, the region that has a large yellow area (Laser efficiency $>$ 30%) is supposed to be used in order to compensate for the reflectivity uncertainties introduced by the custom coating. The top left yellow region in the figure has a high reflectivity at the pump wavelength and low reflectivity at the laser wavelength, meaning a large reflectivity difference ($\sim$ 25%) in a small wavelength separation ($\sim$20%), which is hard to be achieved. The bottom right yellow region has a small reflectivity difference ($\sim$ 5%) which is easier to be achieved, however, it has a smaller tolerance range (smaller yellow area). What's more, if the cavity loss is more than the predicted value, the low reflectance of the output coupler will require an ultra-high input pump intensity to compensate for the unexpected loss and reach the laser threshold. Hence, the right region near the center, with a 10% reflectance difference, is selected. This region is plotted in red ($97.5 \pm 0.5\%$ and $87.5 \pm 1.0\%$ reflectance for output and input couplers), where the laser efficiency is $>$ 30%. Hence, more than 30% efficiency can be achieved if the reflectivity of the custom coating falls into the red box.

A custom-coated mirror from Andover was used as M1 for 3% Yb:YAG, which has a dielectric coating on one surface and an anti-reflection coating (R$<$0.25%) on the other surface, with an angle

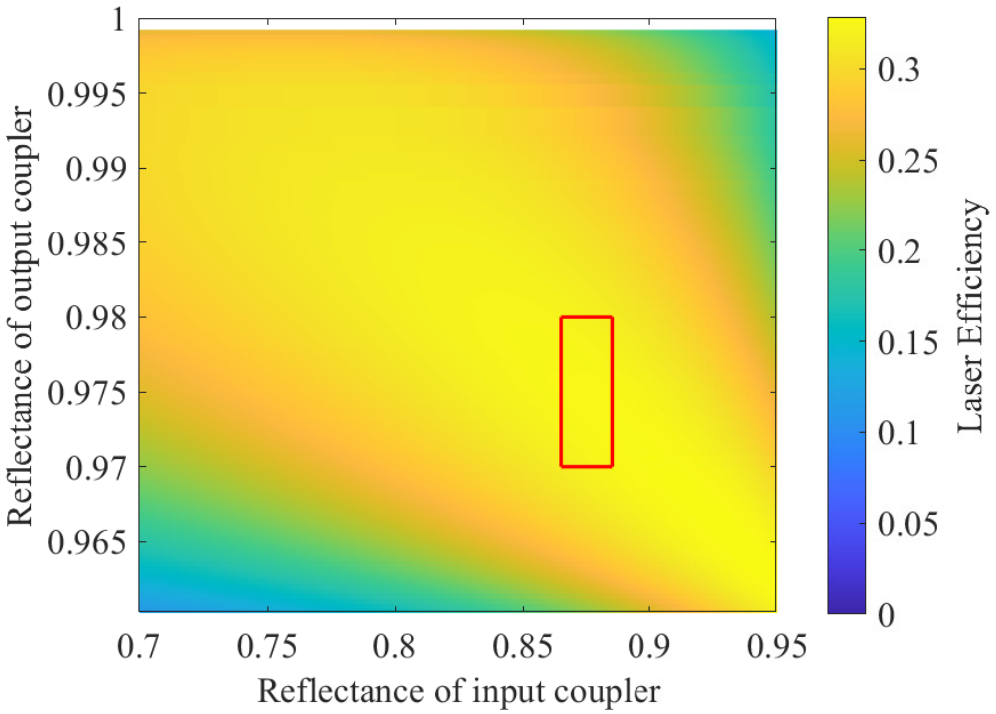

Figure 3.22: Laser efficiency at RBC versus the reflectance of input and output couplers. The maximum laser efficiency in this figure is 32.8%. Besides the input and output couplers, three mirrors with a reflectance of 99.995% are also included in this calculation. The red box plots the region of $97.5 \pm 0.5\%$ and $87.5 \pm 1.0\%$ reflectance for output and input couplers. The background absorption coefficient and impurity saturation intensity are 2×10^{-4} cm^{-1} and 2×10^{4} W/cm^2. The other parameters are the same as that of Fig. 2.6.

of incident of 10° for both coatings. Fig. 3.23a plots the spectral reflectance curve for this mirror, measured with the SHIMADZU UV-3600 spectrophotometer. The reflectance at 1029.3 nm and 1048.0 nm are 88.3% and 97.8%, respectively, leading to a near impedance-matched cavity with a laser efficiency of 32.5% at RBC. Fig. 3.23b plots the small signal gain($I_l = 0$) of 3% Yb:YAG and the cavity loss, induced by the custom coated mirror versus wavelength. The red curve is the calculated small signal gain with a pump intensity of $I_p = 1.9 \times I_{sat,p}$ at 1029.3 nm. It has an intersection with the black curve of the cavity loss, indicating the laser threshold with a lasing wavelength $\sim$ 1050 nm, which is around the resonance transition of E5-E4. The position of the intersection depends on the curvature of the cavity loss, meaning that the lasing wavelength can be selected by tuning the reflectance curve of the output coupler.

The small signal gain (red curve in Fig 3.23b) has a rapid increase at 1050 nm because the emission cross section has a peak at the 1050 nm (E5-E4 transition, Fig 3.1). This peak ensures maximized gain at 1050 nm, leading to a laser wavelength at 1050 nm. To tune the output laser

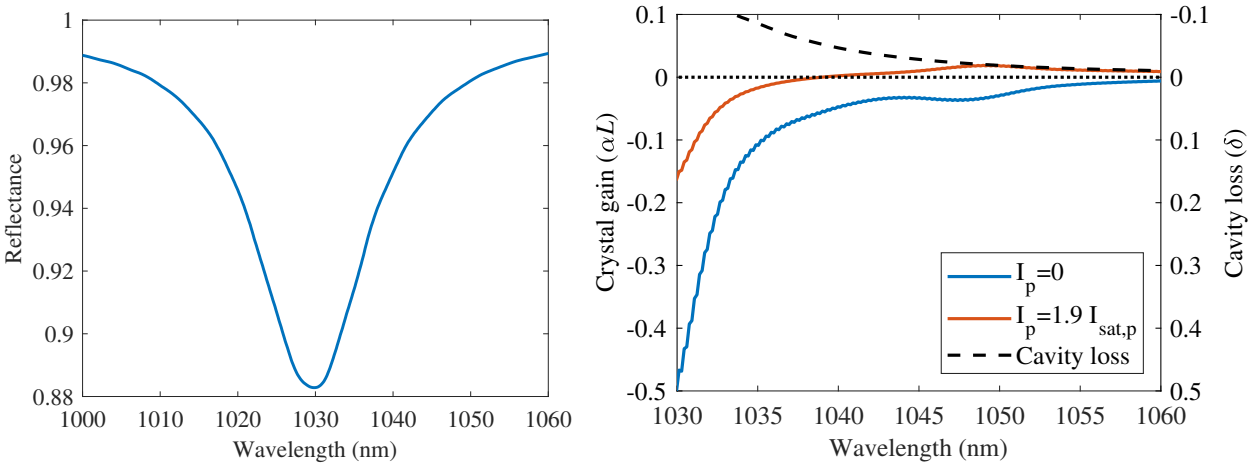

(a) (b)

Figure 3.23: (a) Measured spectral reflectance for the custom coated mirror with a 10° angle of incident. The reflectance at 1029.3 nm and 1048.0 nm are 88.3% and 97.8%, respectively. (b) The small signal gain αL ($I_l = 0$) for the 3% Yb:YAG and cavity loss δ with the custom coated mirror. The blue curve is the gain without the pump light. The red curve is the calculated small signal gain with a pump intensity of $Ip = 1.9 \times I_{sat,p}$ at 1029.3 nm. The lasing wavelength is ∼1050 nm.

wavelength, a steep wavelength-dependent cavity loss near 1050 nm is needed. The tuning can be achieved by either inserting an etalon or introducing a reflectance peak at the desired wavelength in one of the cavity mirrors. For Yb:KYW crystal, the emission cross section near the 1039.6 nm (E5-E4 transition, Fig 3.1) is monotonic decreasing. The laser wavelength can easily be tuned with a wavelength-dependent cavity loss. For example, this can be achieved by introducing a local peak on the designed spectral reflectance curve of the mirror M1. Recall that the laser efficiency, Eq. 3.8, dependents on both the pump and laser wavelength. The laser efficiency will increase (decrease) with the blue (red) shift of the laser wavelength.

Yb:KYW crystal has the highest figure of merit among Yb^{3+} doped RBL mediums [15]. The theoretical maximum laser efficiency at RBC for 1% Yb:KYW, in absence of background absorption, is 41.2% ($\lambda_p = 1022.5$ nm, $\lambda_l = 1039.6$ nm, $\lambda_f = 999.4$ nm, and $\eta_{EQE} = 0.989$), which is much higher than the Yb:YAG crystal. This 1% Yb:KYW crystal is ideal for demonstrating the RBL. However, cracks were observed at the Brewster angle surface, and half of the surface was detached. The transmitted light was strongly distorted, which prevented the laser operation in this crystal. To demonstrate the RBL in KYW host, the 2% Yb:KYW crystal was used. To fit this crystal into the designed ring cavity, both ends of this crystal were polished to have the Brewster angle (E//Nm, 1020nm). The 2% Yb:KYW has less cooling power because the reabsorption of fluorescence is strong in this crystal (Table 4.1), which requires additional pump power at RBC to compensate for the heating. Theoretical maximum laser efficiency at RBC for 2% Yb:KYW

is 15.2% ($\lambda_p = 1022.5$ nm, $\lambda_l = 1039.6$ nm, $\lambda_f = 1002.1$ nm, and $\eta_{EQE} = 0.983$), if the laser wavelength is 1039.6 nm, corresponding to the E5-E4 transition.

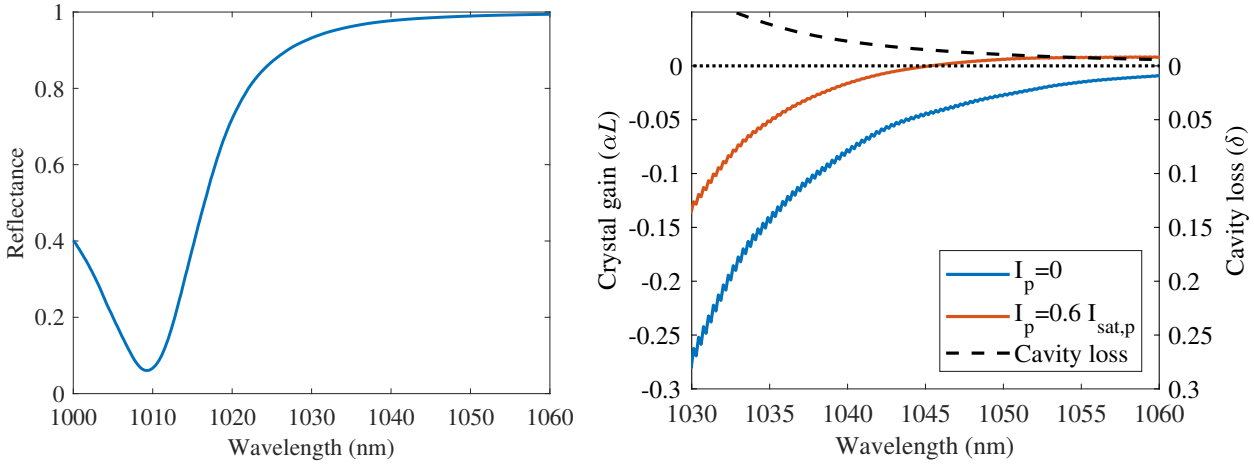

(a) (b)

Figure 3.24: (a) Measured spectral reflectance for the 1064 nm 45° laser line mirror (Edmund 11-075) with a 10° angle of incident. The reflectance at 1022.5 nm and 1050.0 nm are 81.3% and 98.9%, respectively. (b) The small signal gain αL ($I_l = 0$) for the 2% Yb:KYW and cavity loss δ. The blue curve is the gain without the pump light. The red curve is the calculated pump intensity of $I_p = 0.6 \times I_{sat,p}$ at 1022.5 nm. The lasing wavelength is ∼1050 nm.

Due to the feasibility of the custom coating design with a relatively flat reflectance near laser wavelength, a standard 1064nm 45° laser line mirror (Edmund 11-075) was used as the coupler for the 2% Yb:KYW crystal. Fig. 3.24 plots the spectral reflectance of this mirror and the small signal gain of this 2% Yb:KYW crystal. The reflectance increases from 6% to 99% with the wavelength increasing from 1010 nm to 1050 nm. The 1022.5 nm pump and desired 1039.6 nm laser sit on a steep slope and have a reflectance of 81.3% and 97.5%. However, the reflectance is monotonic, increasing near the laser wavelength and the reflectance at 1050 nm is as high as 98.9%. This 98.9% reflectance leads to a lower cavity loss at 1050 nm compared to the ideal 1049.6 nm. Then, the position of the intersection between gain and loss is ∼ 1050 nm, rather than the on resonance 1039.6 nm. This red shift of the laser wavelength reduces the theoretical maximum laser efficiency at RBC to 10% ($\lambda_p = 1022.5$ nm, $\lambda_l = 1050$ nm, $\lambda_f = 1002.1$ nm, and $\eta_{EQE} = 0.983$).

The laser efficiency at RBC is plotted in Fig. 3.25 for 2% Yb:KYW crystal with 1022.5 nm pump wavelength and 1050 nm laser wavelength. The maximum laser efficiency reduces to 2.8% from the theoretical maximum laser efficiency of 10%. That's because the Yb:KYW is impure compared to Yb:YAG (Table 4.1), and the parasitic heating induced by the impurities requires an

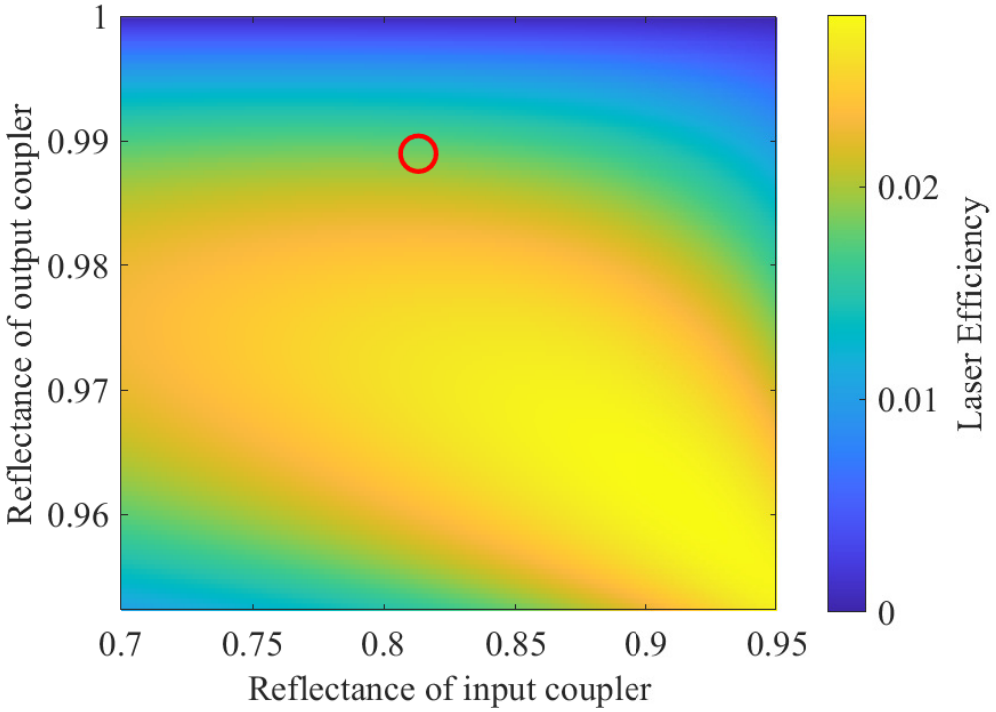

Figure 3.25: Laser efficiency at RBC versus the reflectances of input and output couplers. The maximum laser efficiency in this figure is 2.8%. Besides the input and output couplers, three mirrors with a reflectance of 99.995% are also included in this calculation. The red circle indicates the reflectance of the Edmund mirror, 81.3% reflectance at 1022.5 nm and 98.9% reflectance at 1050 nm. The corresponding laser efficiency is 1.8%. The background absorption coefficient and impurity saturation intensity are 9.4×10^{-4} cm^{-1} and 2×10^{4} W/cm^2. Fixed parameters for the wavelength of the pump and its absorption and emission cross sections were 1022.5 nm, 3.90×10^{-21} cm^2 and 3.51×10^{-20} cm^2 respectively. The wavelength, and absorption and emission cross sections of the laser were 1050 nm, 2.19×10^{-22} cm^2, and 6.94×10^{-21} cm^2. The fluorescence lifetime was set to 0.3 ms. Pump and laser saturation intensities were calculated to be 1.66×10^{4} W/cm^2 and 8.81×10^{4} W/cm^2. The mean fluorescence wavelength and external quantum efficiency are 1002.1 nm and 98.3%.

additional pump power to compensate for the extra heating. What's more, the 2.8% efficiency is for an impedance-matched cavity, while the standard laser line mirror we used is far from the impedance-matched condition. The red circle indicates the reflectance of the Edmund mirror, 81.3% reflectance at 1022.5 nm and 98.9% reflectance at 1050 nm. The calculated laser efficiency for this mirror is 1.8%.

The factors limiting the laser efficiency are summarized here. First, the crystal is 2% Yb:KYW, rather than the ideal 1% Yb:KYW. The strong reabsorption in 2% crystal reduces the cooling power and decreased the theoretical maximum laser efficiency from 41.2% to 15.2%. Second, the lasing wavelength is 1050 nm rather than the 1039.6 nm resonance transition. This red shift of

the laser wavelength reduces the theoretical maximum laser efficiency (Eq. 3.8) from 15.2% to 10%. Third, the impurity level for Yb:KYW crystal is higher than Yb:YAG, requiring more pump power to compensate for the background heating. This high impurity level further reduces the laser efficiency from the theoretical maximum of 10% to 2.8%. Finally, the pump is not totally absorbed since the cavity is not an impedance-matched cavity. The laser efficiency is reduced from 2.8% to 1.8%. Though the laser efficiency is low, the RBC can still be achieved with the standard laser line mirror for this impure 2% Yb:KYW crystal.

This section discussed the selection of the input and output couplers for Yb:YAG and Yb:KYW RBLs and the corresponding laser efficiencies. The next section will show the experimental approach of realizing the pump-locked RBL cavity.

3.6.3 Radiation Balanced Laser Setup

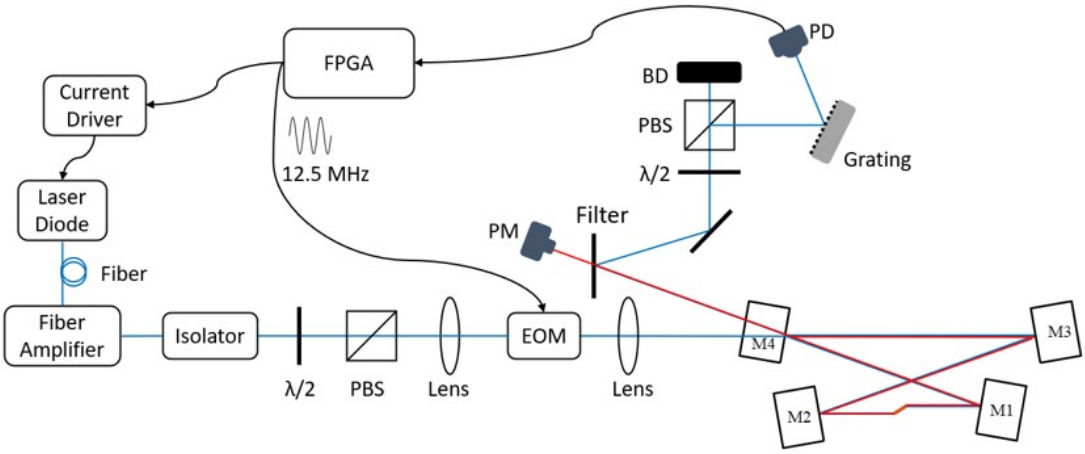

Figure 3.26: Schematic of the RBL setup. Abbreviations are as follows, PBS: polarizing beam splitter, EOM: electro-optic modulator, PM: power meter, BD: beam dump, PD: photodetector.

In this section, the experimental setup for the RBL is presented. The diagram of the setup is shown in Fig. 3.26. The 1030 nm laser diode for Yb:YAG (Innovative Photonic Solutions I1030SB0050PA-IS), or the 1022.5 nm for Yb:KYW (Innovative Photonic Solutions I1022SB0100PA), was mounted on the Thorlabs LM14S2 laser diode mount. The Thorlabs TED 200C temperature controller and Thorlabs LDC 205C laser diode driver were used to control the temperature and current of the laser diode. The output of the laser diode, after a fiber isolator (DK Photonics PMISO-S-30-P-L-F-90-08-FA) and a fiber attenuator (Thorlabs VOA1064PM-APC), was used as a seed for a fiber amplifier (IPG YAR-10K-1020-LP-SF), which was able to deliver an output power of 11W. The pump beam was focused by a lens to go through an electro-optic modulator (LINOS PM-C-BB), which was driven by a voltage amplifier (QIOPTIQ SIN-Amplifier) with

a reference oscillation signal of 12.5 MHz generated by a FPGA (Red Pitaya STEMlab 125-14). A second lens was used, combined with the first one, to reshape the pump to match the cavity mode of the ring cavity. The pump beam reflected by the cavity together with the output laser beam were separated by a long pass edge filter (AVR Optics LP02-1064RU-25). A detector (Thorlabs PDA05CF2) was used to monitor the reflected pump after a grating (Newport 33009FL01-360R). The Pound–Drever–Hall technique [65, 66, 67] was used to lock the cavity to the pump wavelength. The current driver of the laser diode was tuned by the FPGA based on the signal of the reflected pump power [68]. The input pump power and output laser power were measured by a power meter (Thorlabs S470C and Thorlabs PM100D), and the crystal temperature was monitored by a thermal camera (Sec. 3.3.1).

The FPGA has a clock period of 8 ns, and the on-board digital-to-analog converter has an output bandwidth of 50 MHz with a voltage range of ± 1 V. Every 10 clock periods (80 ns), the output voltage reversed the sign (± 1 V), leading to a square wave output with a frequency of 12.5 MHz. A homemade three-stage low pass filter with a cutoff frequency of 18 MHz was used to convert the square wave to a sine wave. This sine wave was amplified to 50 Vpp (peak to peak voltage) to drive the electro-optic phase modulator. This phase modulator introduced a $\lambda/30$ phase difference, which generated two 12.5MHz sidebands with a relative power of 1% of the fundamental (square of the first Bessel function, $J_1(2\pi/30)^2$). The reflection ratio of the laser cavity was different for the fundamental and two sidebands, and the reflected pump beam contained the beat signal. The reflected pump signal was monitored by a high-speed detector and was sent to the FPGA. The lock-in amplifier was implemented digitally to separate the error signal [68]. The input signal was multiplied by the 12.5 MHz reference and then was filtered by using a low pass filter with a cut-off frequency of 15.3 kHz. Then the separated error signal was sent to the PID module to generate the control signal digitally. The best combination of the proportional, integral, and derivative was found (1.5 proportional coefficient, 50 ms integral time, and zero derivative coefficient), which made the mean and standard deviation of the error signal close to zero during locking. In scanning mode, the output signal of the FPGA was a triangular ramp signal. During scanning, when the error signal reached a set trigger value, the output was swapped to the PID control signal. This output voltage was sent to the laser diode current driver to modulate the current applied to the laser diode in order to modulate the wavelength. Hence, the wavelength of the laser diode can be locked to the cavity longitudinal mode. The output power of the laser diode is $\sim$40 mW. A fiber attenuator was used to reduce the seed power to $\sim$4 mW since the required input power of the fiber amplifier is 1-5 mW.

Two lenses were used to couple the pump beam to the cavity mode. The positions and curvatures of the cavity mirrors define the oscillating intracavity Gaussian mode. For the designed ring cavity (Fig. 3.18), the intracavity Gaussian beam was focused in the center of the crystal (Fig. 3.20).

Meanwhile, this focused beam was refocused by the curved mirrors (M3 and M4) to the plane in the middle of l2 with a beam waist of $\sim 260 \mu$m. Experimentally, if the input pump beam is focused to the center of l2 with the designed beam waist, the mode match between the input pump beam and cavity mode can be achieved. First, the beam size of the pump from the fiber amplifier was measured at various positions with a beam profiler (Thorlabs BC106-VIS) to measure the beam waist and the waist position. Then, based on the separation between the fiber amplifier and the cavity, the propagation of the Gaussian beam through two lenses with fixed focal lengths (400 mm and 300mm) was calculated. This calculation gives the positions of the two lenses where the pump can be focused to the middle of l2 with desired beam waist. The pigtail of the fiber amplifier and both lenses are mounted on a translation stage for fine adjustment. A beam profiler (Thorlabs BC106-VIS) was placed at the designed focal plane in the middle of l3 to check the beam waist and waist position. When the measured beam waist and waist position is the same as designed, the input pump beam is coupled to the cavity mode.

This section discussed all the parameters needed to design the RBLs. The sequences of steps needed to design a new RBL are summarized here. First, the cooling power needs to be measured for a new crystal, to identify the external quantum efficiency and background absorption coefficient (Section 3.4). Then, the cooling efficiency measurement at various intensities gives the saturation intensity of the background impurity (Section 3.4). With all these parameters, the pump wavelength can be selected. Normally the pump beam has a wavelength where the cooling power is maximized. Once the desired laser wavelength is known, the efficiency plot (3.17) can be generated to help with the selection of mirrors. When selecting the mirrors, the wavelength-dependent cavity loss (Fig. 3.23) needs to be checked to make sure the laser wavelength does not shift for the designed reflectance curve. Finally, based on the available pump power, the cavity (Section 3.6.1) can be designed to confine the beam size inside the crystal to reduce the required power to reach the balance condition.

CHAPTER 4

Results and Discussion

This chapter presents and discusses the main experimental and theoretical results relevant to laser cooling and RBLs. Section 4.1 compares the thermal isolation of glass and aerogel supports. Next, measured cooling powers are presented for Yb:YAG and Yb:KYW crystal in Section 4.2, and Yb:KYW is found to have less cooling because of the higher impurity. The following Section 4.3 shows the measured cooling efficiency at different intensities, proving cooling can be enhanced by saturating the impurities absorption, which enables the RBL operation for impure Yb:KYW crystal. Lastly, Section 4.4 details the RBL measurements for Yb:YAG and Yb:KYW.

4.1 Thermal Isolation of Glass and Aerogel Supports

This section shows the measured temperature change of cooled Yb:KYW crystal with glass and aerogel supports to study the thermal isolation between the crystal and supports in order to find the best supporting material for laser cooling and RBL experiments. In addition, the results of COMSOL simulations are also presented to help understand the process of heat transfer.

Figure 4.1 plots the crystal temperature change of 1% Yb:KYW when pumped with 1 W at 1025 nm, obtained by the thermal camera and DLT. The Pump radiation was focused to a spot diameter of 165 μm and passed once through the sample. In these figures, lineouts are shown for two different parts of the overall thermal image. The red curve monitored the support material immediately adjacent to the crystal. The blue curve monitored the transient temperature of the crystal itself. For comparison, temperatures deduced from DLT are shown in black, closely overlapping the blue curve.

A small temperature drop, followed by a heating transient, was observed in samples supported on glass (Fig. 4.1a) in both the thermal camera and DLT data. This was interpreted as the result of fast initial cooling in the interaction volume followed by an influx of heat from uncooled portions of the sample itself and through contacts of the sample with its holder. Upon replacing the glass supports with an aerogel disk, the data of Fig. 4.1b were obtained. Despite the increase in contact area

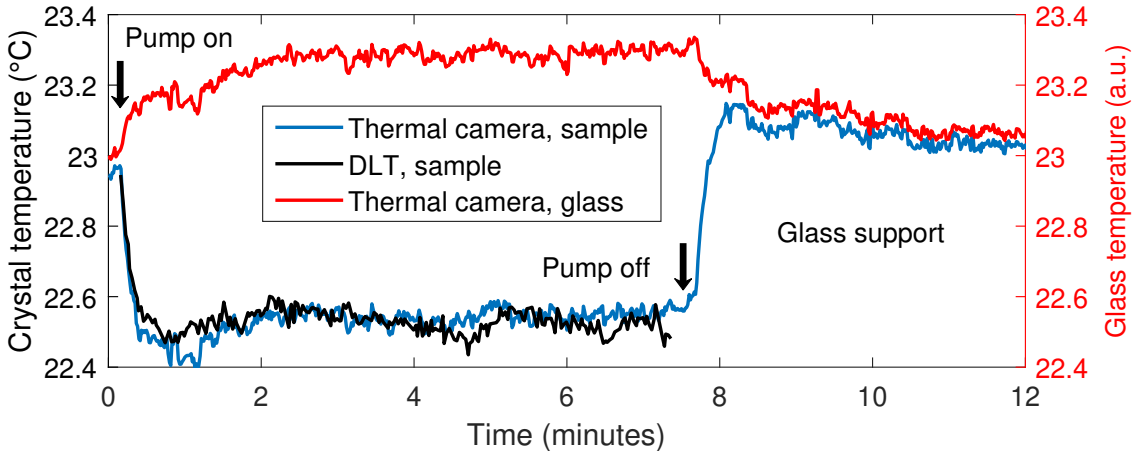

(a)

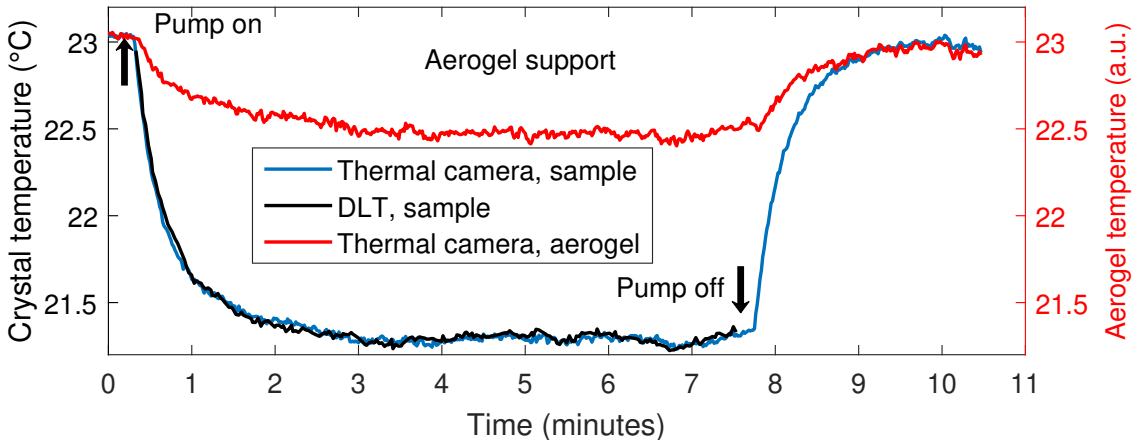

(b)

Figure 4.1: (a) Data from the infrared camera, showing image lineouts of temperature versus time of the 1% Yb:KYW crystal (blue) and the glass support next to it (red). Because the camera was focused on the crystal, not the glass, only the left scale is accurately calibrated. (b) Image lineouts and DLT data on temperature versus time for the same sample on aerogel. For comparison, in each of (a) and (b), temperature versus time obtained by the DLT method is also displayed (black).

incurred by placing the crystal directly on this support, the thermal isolation improved markedly due to the exceedingly low thermal conductivity of the aerogel. Three-dimensional COMSOL simulations of heat transport and cooling (as well as the infrared camera data of Figs. 4.1) confirmed that localized heat transfer through the contact points of a crystal supported by glass capillaries offset most of the radiative cooling provided by the laser beam. Much larger temperature drops, indicating better thermal isolation, were noted in samples supported on aerogels. Glass supports were heated by fluorescent emission from the sample as evidenced by the red trace in Fig. 4.1a whereas the aerogels absorbed less fluorescence and cooled, as shown by the red trace in Fig. 4.1b.

Additionally, a small heating transient in the blue and black curves tracking sample temperature in Fig. 4.1a disappeared with the use of aerogels (Fig. 4.1b). This indicated that the heat load responsible for the observed rise of temperature following the fast initial drop was delivered through the glass supports and was negligible with aerogels.

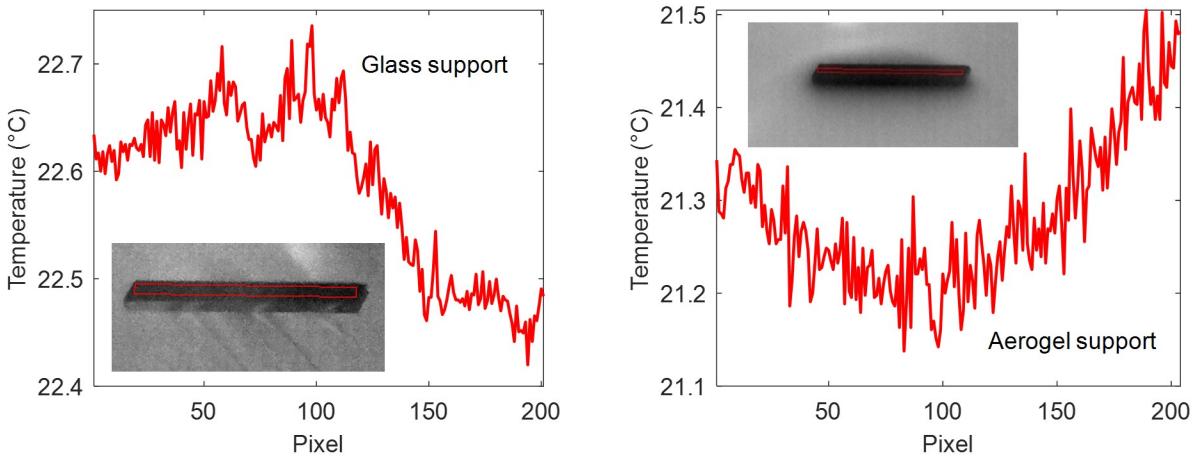

(a) (b)

Figure 4.2: Longitudinal temperature distribution of the crystal on (a) glass supports and (b) an aerogel disk. Insets show the thermal camera image of the crystal with the pump beam introduced from the left.

An experimental trace of the longitudinal temperature distribution in a 1% Yb:KYW crystal on glass is shown in Fig. 4.2a. Two peaks in temperature were observed at contact points between the sample and glass, confirming the strong influx of heat from the support. Although the support was made of three capillaries, only two of them made contact with the crystal in this experiment. The temperature distribution on aerogel support was plotted in Fig. 4.2b, where it may be noted that the location where the temperature was lowest was not at the input face of the crystal where pump power was highest. Instead, because of convective heat input at the ends, the crystal was coolest near its mid-point.

Finite element computations were performed using COMSOL to determine sample temperature from a set of coupled equations. The equations specified relations for cooling power, the Stefan-Boltzmann Law, diffusion, and convection following prior work [57]. Boundary conditions corresponded to actual sample sizes. Material parameters were taken from the literature or, in the case of emissivities, were determined from thermal camera data taken over a range of temperatures for calibration using the Stefan-Boltzmann Law. Mesh sizes for calculated temperature distributions were chosen to ensure very high spatial resolution (4.3a). These simulations predicted more uniform cooling with twice the temperature drop on aerogels versus glass. Experimental data how-

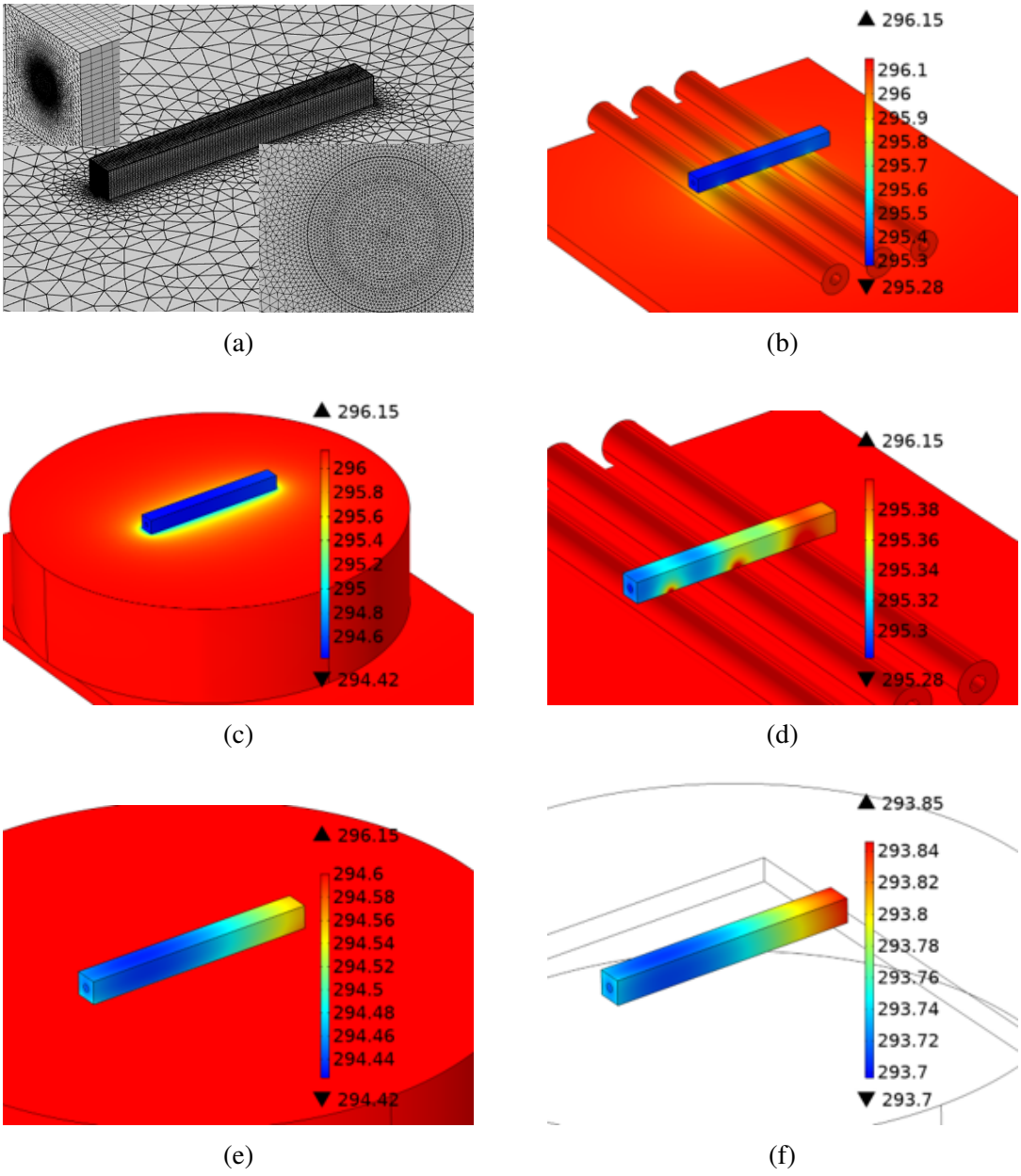

Figure 4.3: (a) Image of the crystal and mesh geometries used for the COMSOL simulation. The upper inset shows the 3-D mesh of the crystal end, and the lower inset shows the 2-D mesh grid on that surface. (b-e) COMSOL simulations of laser cooling with input power of 1 W at 1025 nm in a $1 \times 1 \times 10$ mm^3 sample of 1% Yb:KYW, on (b) glass and (c) aerogel. (d,e) are identical to (b,c) but have magnified temperature scales to highlight local heating and gradients. The calculated temperature drops are 0.87 K in (b,d) and 1.73 K in (c,e). (f) Simulation of laser cooling with a substrate thermal conductivity of zero. The calculated temperature drop is $\Delta T = 2.45$ K. All simulations include thermal conduction, convection, and black-body radiation. Crystal parameters were taken from Table 4.1.

ever showed a factor of three improvement on aerogel. This discrepancy arose from the absorption of fluorescence by the glass capillaries, an extra source of heat which was omitted in the simulation but appears to be strong in the experiments on glass as indicated by the thermal camera image in Fig. 4.2a. For simulations and experiments exclusively on aerogels, a much better agreement was obtained. In 1% Yb:KYW and 3% Yb:YAG, the simulated temperature drop was within 10% of the experimental value based on either DLT or thermal camera measurements. In Fig. 4.3d and 4.3e the scale of the simulation has been magnified to permit more detailed visualization of the temperature distributions. It is evident in these figures that on aerogel the temperature distribution is more uniform, and the longitudinal gradient of temperature is smaller than on glass. The points of contact on glass can also be seen to display local heating, which is absent in the results on aerogel. Residual differences between measured and simulated temperatures on aerogel supports in Figs. 4.1 and 4.3, while small, were ascribed to non-optimal positioning of the pick-up fiber in relation to the point of lowest temperature along the sample axis. A further conclusion can be drawn from Fig. 4(f), where the temperature drop obtained on a fictitious substrate having zero thermal conductivity is simulated. While a non-conducting substrate provides better thermal isolation as expected, the experimental results on aerogel (Fig. 4.1b) reveal a temperature drop that is 70% of the theoretical value, showing nearly ideal performance. Thus, the combined results of Figs. 4.1, 4.2 and 4.3 confirm that better thermal isolation and greater uniformity of temperature can be achieved with the use of aerogel supports. Therefore, the aerogel supports were used in the laser cooling and RBL experiments.

4.2 Cooling Power Measurement of Yb:YAG and Yb:KYW Crystals

The previous section demonstrated that the aerogel provided better thermal isolation compared with the glass capillaries. This section presents the measured cooling power and crystal parameters for Yb:YAG and Yb:KYW crystals with aerogel supports using the steady-state method mentioned in Subsection 3.4.2.

The cooling power versus wavelength for 3% Yb:YAG is shown in Figs. 4.4, where the solid curves are best-fits to Eq. (3.6) using the experimentally measured absorption spectra and a wavelength-independent level of background impurity absorption. The fit is presented after normalization to the input power for convenient comparison. Optimum cooling in 3% Yb:YAG was at $\sim$ 1030 nm, in close accord with the wavelength of maximum cooling power expected from Eq. (3.6). The fits for Yb:KYW crystals are shown in Fig. 4.5. The calculated maximum cooling efficiencies are 2.3 % at 1050 nm for 3% Yb:YAG, 1.0% at 1030 nm for 1% Yb:KYW, 0.9% at

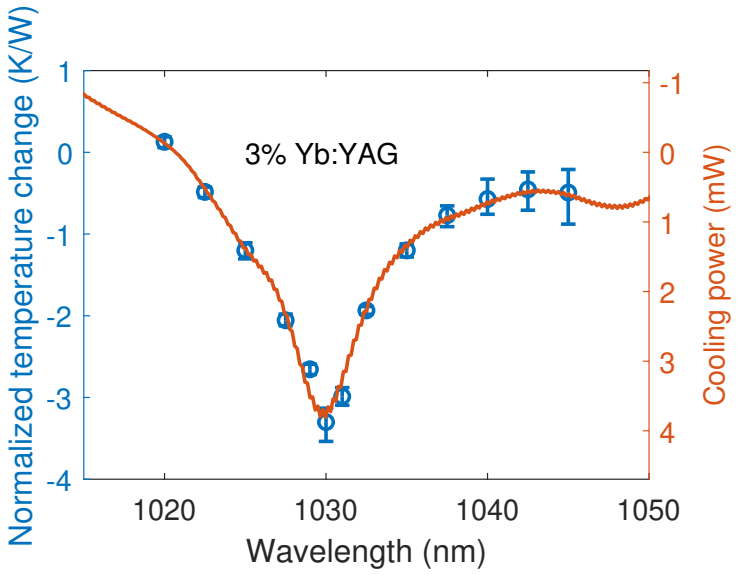

Figure 4.4: Temperature change versus wavelength for 3% Yb:YAG, with a theoretical fit (solid curve) of cooling power from Eq. (3.6) using the best-fit parameters of Table 4.1. Pump power was 1 W with a spot diameter of 165 μm.

1038 nm for 2% Yb:KYW, 0.5% at 1051 nm for 10% Yb:KYW, and -0.8% at 1051 nm for 20% Yb:KYW. The external quantum efficiency η_{EQE} and background impurity absorption coefficients α_b determined from the best fits are shown in Table 4.1. These values are in reasonable agreement with the estimates from thermal lens spectroscopy[24].

Samples	**Doping (Mole %)**	$\boldsymbol{\lambda_f}$ **(nm)**	$\boldsymbol{\eta_{EQE}}$	$\boldsymbol{\alpha_b}$ **(cm^{-1})**
Yb:YAG	3	1012.1	0.993 ± 0.001	$(2.0 \pm 1.8) \times 10^{-4}$
Yb:KYW	1	999.4	0.989 ± 0.001	$(1.7 \pm 0.2) \times 10^{-3}$
Yb:KYW	2	1002.1	0.983 ± 0.001	$(9.4 \pm 1.2) \times 10^{-4}$
Yb:KYW	10	1006.6	0.971 ± 0.002	$(1.1 \pm 0.6) \times 10^{-3}$
Yb:KYW	20	1013.0	0.965 ± 0.005	$(2.6 \pm 1.4) \times 10^{-3}$

Table 4.1: Sample specifications and parameters deduced from DLT analysis.

The Yb:YAG crystal had a lower measured background absorption coefficient compared to Yb:KYW crystals. The small background coefficient in the YAG sample indicates higher purity than the KYW crystals, and partly accounts for its superior cooling power, which is evident from a comparison of Fig. 4.4 and 4.5. For Yb:KYW crystals, contrary to the expectation that more coolant ions should improve laser cooling, the cooling power in 10% Yb:KYW was less than in 1% Yb:KYW or 2% Yb:KYW near room temperature. In the 20% sample, net heating was observed (Fig. 4.5d). When increasing the doping density, the reabsorption effect is increased, as one can see from the absence of the 980 nm emission line in Fig. 3.2. This reabsorption leads to a

lower escape coefficient and a longer mean fluorescence wavelength, reducing power emitted from the crystal, which is considered as the major limitation for cooling power. Dopant densities below 10% are therefore the most favorable for RBL operation in KYW at present.

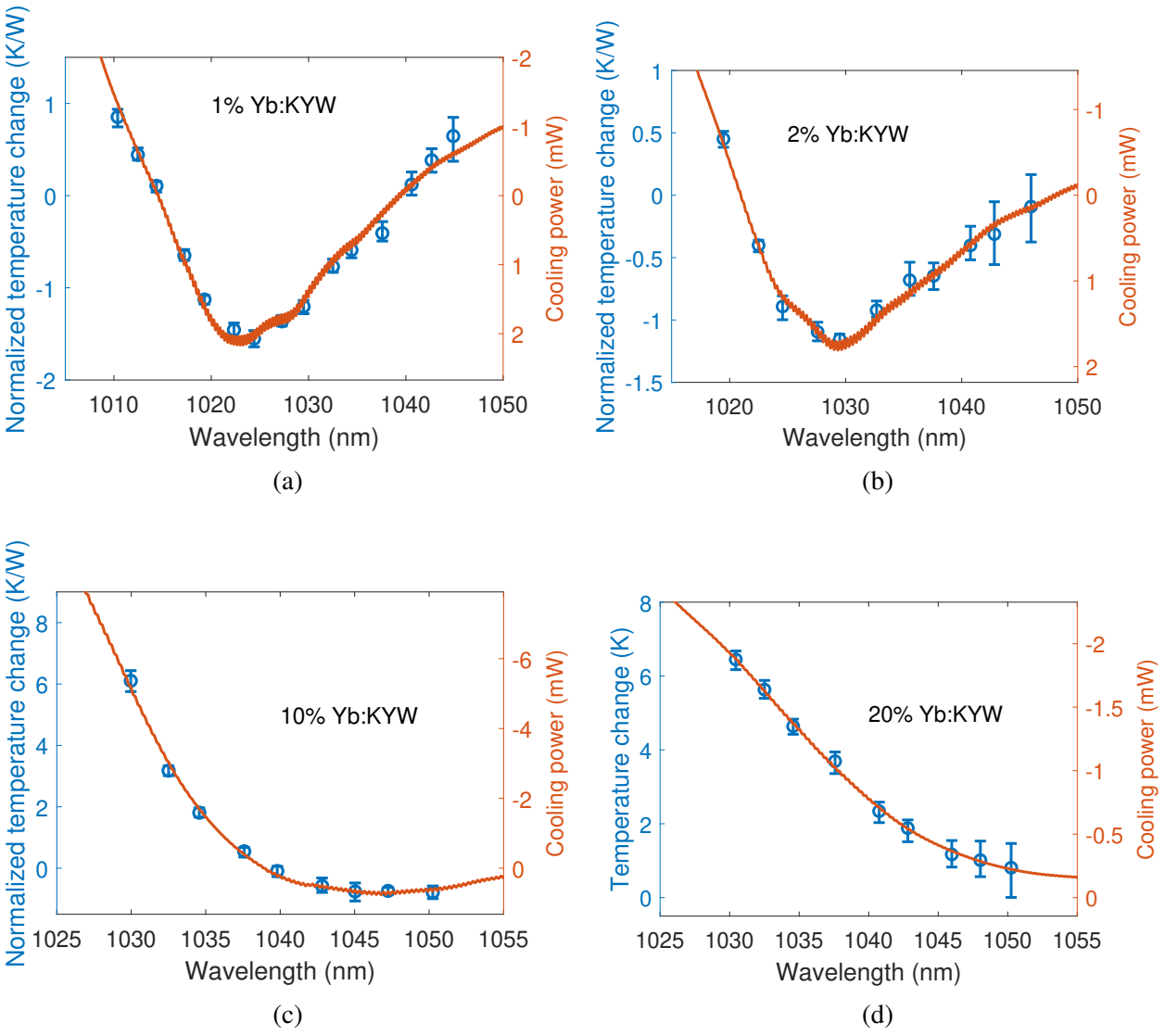

Figure 4.5: Temperature change versus wavelength for Yb:KYW crystals, with a theoretical fit (solid curve) of cooling power from Eq. (3.6) using the best-fit parameters of Table 4.1. Pump power was 1 W (a), 0.8 W for (c) and 0.1 W for (d). In (b), the pump power was 1 W for wavelengths shorter than 1036 nm, and 0.8 W for the rest due to laser tuning limitations. The spot diameter for the pump is 148 μm.

4.3 Improved Cooling Efficiency for Yb:YLF Crystal through Optical Saturation

The previous section showed the measured cooling power for Yb:YAG and Yb:KYW crystals, and the cooling power was found to be limited by the background absorption for impure Yb:KYW crystals. This section presents the measured cooling efficiency at various pump intensities, showing an increased cooling efficiency by reducing the background absorption through the optical saturation of background impurities, which demonstrates the differential absorption saturation theory presented in Section 2.2

Figures 4.6 present plots of cooling efficiencies as a function of wavelength, measured with DLT and Thermal Lens Spectroscopy (TLS) [50] at several intensities. The pump intensities and beam radii corresponding to these measurements are tabulated in Table 4.2. Both plots indicate that the slopes of the cooling efficiency curves steepen with increasing intensity. At long wavelengths, the cooling efficiencies at elevated intensities also exceed those at low intensity. Intensity-dependent improvement in η_c implies that the saturation of coolant and impurity ions is different and varies with wavelength. This effect, which we refer to as differential absorption saturation, can be explained by the arguments of Section 2.2.

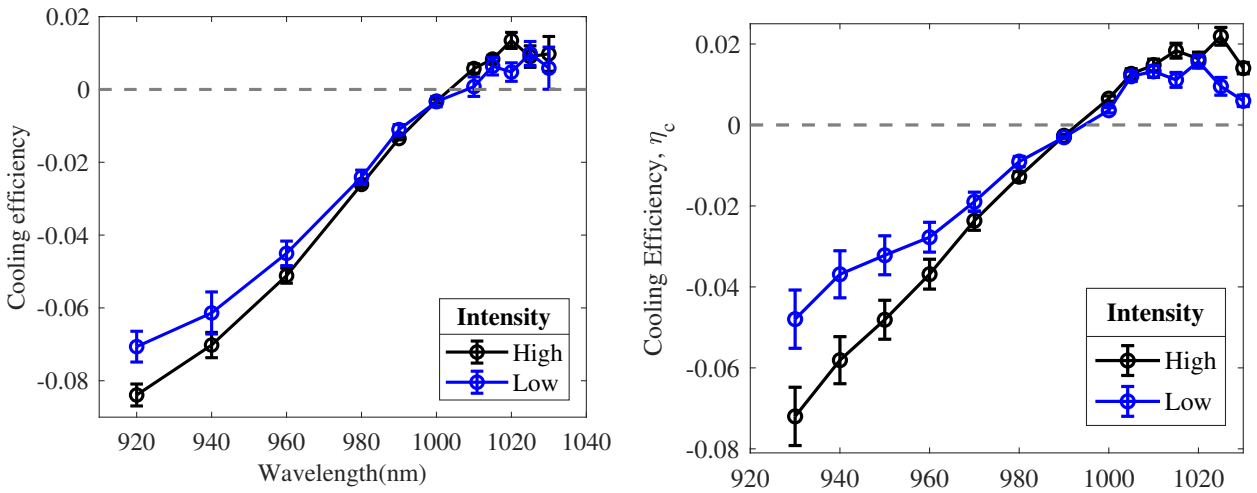

Figure 4.6: (a) DLT and (b) TLS measurements of cooling efficiencies in 10% Yb:YLF as a function of wavelength and intensity. The input powers were 0.8 W for (a) and in a range of 30-530 mW for (b). The pump beam was focused to the tabulated spot sizes and the resulting intensities are listed in Table 4.2.

A further thing to note in Figure 4.6 is that the experimental traces for efficiency at different intensities intersect around 1000 nm. At this wavelength, the curves all pass through a common

	Beam radius (μm)	Intensity (W/cm^2)
DLT High	32.4-39.3	$(1.6-2.4)\times 10^4$
DLT Low	284-318	$(2.0-3.3)\times 10^2$
TLS High	316-364	$(1.1-1.3)\times 10^3$
TLS Low	316-364	$(1.1-1.3)\times 10^3$

Table 4.2: Pump beam radius (half-width at 1/e^2 intensity) and intensity values used for the measurements presented in Fig. 4.6. Entries indicate the small variations of intensity at multiple wavelengths for each intensity category.

point as predicted by the theory of Sec. 2.2. The significance of this is that cooling efficiency is the same for all intensities, or that the cooling efficiency is independent of intensity at this point. For this to be the case, the saturation intensity of background impurities must equal that of the coolant ions, computed from Eq. (2.14) to be $\sim 2.6\times 10^4$ W/cm^2. Hence, a determination of the wavelength (λ_{cr}) at which the crossing takes place permits one to deduce the saturation intensity of background impurity absorption, which is the key limitation to cooling efficiency.

Data taken in the cooling range at wavelengths longer than λ_{cr}=1000 nm in both figures show the same crossing wavelength and heightened cooling efficiencies at elevated intensities. This is consistent with an increase of the Yb^{3+} saturation intensity relative to the background as the detuning from the Yb^{3+} absorption peak increases. In this range ($\lambda > \lambda_{cr}$), the observations can be explained by low background saturation intensity ($I_b(\lambda) < I_r(\lambda)$), which leads to reduced parasitic heating and heightened efficiency. Data taken in the heating range at slightly shorter wavelengths ($\lambda < \lambda_{cr}$) have progressively smaller detunings from the Yb^{3+} absorption peak. Cooling efficiencies drop but still display an intensity dependence, consistent with a reduction of the Yb^{3+} saturation intensity near resonance.

TLS and DLT measurements in 10% Yb:YLF were in good mutual agreement. Both sets of experiments revealed an intensity dependence of laser cooling and efficiency enhancement at elevated laser intensities. These effects are in accord with differential absorption saturation theory (Sec. 2.2) which predicts that saturation of the background absorption at high pump intensities can increase laser cooling efficiency (provided that $I_b < I_r$). The observation of a crossing point (λ_{cr}) in efficiency curves measured at different intensities furnishes a new method of determining the saturation intensity of background absorption, applicable even when the absorbing species is not identified. The experimental value for our sample was found to be $I_b = I_r(\lambda_{cr}) = 2.6\times 10^4$ W/cm^2 by inserting the observed wavelength λ_{cr} together with measured cross sections into Eq. (2.14).

The background saturation intensity I_b is surprisingly low. This result may stem from the valence and site symmetry of the dominant impurity. Divalent iron is thought to be the main source

of background absorption in Yb:YLF crystals [53], but this impurity could also substitute at Yttrium (Y^{3+}) sites in YLF, rendering it trivalent. If this were the case, we note that trivalent iron in a material like Fe:YAG has a low-energy transition from $^6A_{1g}$ to $^4T_{1g}$ that is both spin- and parity-forbidden [69]. It is known that there is a long-lived excited state accessed by this forbidden transition with a fluorescence lifetime of 170 µs [70], making it easy to saturate. In the YAG host, the transition is centered at 903 nm and is broad enough that it has an absorption cross section of $\sigma_a = 1.2 \times 10^{-20}$ cm^2 at 1000 nm [16]. While the emission cross section in YAG and both the absorption and emission cross sections in YLF are unknown, it is not unreasonable to surmise that the background saturation intensity of trivalent iron could be extremely low at this wavelength in YLF. Basing an estimate solely on σ_a of Fe^{3+}:YAG, the calculated saturation intensity of trivalent iron would be 9.9×10^4 W/cm^2, which is 23% lower than that of Yb^{3+} at 1000 nm calculated in the same way. This agrees roughly with the saturation intensity I_b determined for the background in our sample, as well as the requirement that $I_b < I_r$ for enhanced cooling (albeit in a different host). Much higher saturation intensities would be expected for other valences like Fe^{2+} or Fe^{4+} since transitions near 1000 nm are allowed and originate from short-lived upper states [71]. Fe^{2+} or Fe^{4+} would not saturate at the low intensities of our experiments. However, a sizeable proportion of Fe^{3+} ions could easily saturate and become less absorptive, thereby causing an improvement in cooling efficiency. Consequently, we consider Fe^{3+} to be a viable candidate for the saturable background species in our experiments.

Impurities other than iron could of course contribute significantly to background absorption in crystalline Yb:YLF. Earlier work found significant correlations between background absorption levels and elements such as vanadium and chromium [53]. In certain valence states, these elements could have low saturation intensities near 1000 nm. Cr^{4+} ions in YAG, for example, have a saturation intensity that is only 10% of that of Yb^{3+} at 1000 nm [72]. Consequently, a mixture of background absorption species might be involved in the reduction of parasitic heating and enhanced cooling reported here at high pump intensities. Although we are unable to state with certainty what ionic species causes intensity-dependent laser cooling, it does seem that transition metal and other impurities present as trace elements have properties consistent with the experimentally-determined saturation intensity $I_b = 2.6 \times 10^4$ W/cm^2.

Our results show that the major efforts that have been made in the past to purify optical refrigerants are not the only way to improve cooling efficiency or to reach lower temperatures in a given material. In Subsection 2.2.3, optical saturation is shown to offer a possible route for reaching lower MAT. The achievement of lower temperatures would significantly improve the performance of imaging arrays by reducing electronic noise. We note however that because absorption coefficients are temperature-dependent [4], characterization of optical saturation at low temperatures will be necessary to predict precisely how successful this cooling strategy may be in practice.

Only if the background absorption saturates before that of the coolant ions in the cryogenic range ($I_b < I_r$) will MATs drop as the result of operation at high pump intensities (see Fig. 2.4a).

The inclusion of background saturation in laser cooling analysis not only reveals that optical refrigeration can be improved at high intensities, but makes an important correction to radiation-balanced laser theory. When background saturation is included, stable solutions for radiation balance are found at impurity absorption levels typical of batch-processed crystals ($\alpha_b(0) > 10^{-4}\ cm^{-1}$) rather than in ultrapure ($\alpha_b(0) < 10^{-4}\ cm^{-1}$) laser media exclusively (Figure 2.10). More accurate predictions and modeling are enabled when parasitic heating and background saturation are included in the heat equation of RBLs. This finding will therefore promote the use of cooling materials that are not well developed and currently suffer from higher background impurity levels, such as KYW [24]. That is, this research opens an avenue for laser refrigeration of impure materials that could not be cooled previously at all.

4.4 Radiation-Balanced Lasers using Yb:YAG and Yb:KYW

This section presents the experimentally measured radiation-balanced laser operations for Yb:YAG and Yb:KYW with aerogel supports. The experimental setup was shown in Subsection 3.6.3. The crystal temperature and output laser power were measured with a series of input pump powers. The radiation-balanced operation was determined when the crystal temperature remained unchanged during lasing. The laser efficiency was recorded at the radiation-balanced condition (RBC). Radiation-balanced operations were observed in 3% Yb:YAG and 2% Yb:KYW crystals. Recall that in subsection 3.6.2, the designed laser efficiency for 3% Yb:YAG was 32.5% at radiation-balanced operation. The experimentally measured laser efficiency was 30.5%, which is in excellent agreement with the theoretical prediction. For Yb:KYW, due to the damage of the ideal 1% Yb:KYW and lack of mirrors with desired reflectance curve, the 2% Yb:KYW crystal was used with a standard laser line mirror. These compromises reduced the laser efficiency from a theoretical maximum of 41.2% to 1.8%. The experimentally recorded laser efficiency for the 2% Yb:KYW crystal was 2.2%, in excellent agreement with the design. The achieved laser efficiency of 30.5% for 3% Yb:YAG is the highest among all radiation-balanced lasers (RBL) to date. The radiation-balanced operation is first observed in Yb:KYW crystal, which is predicted to have the highest figure of merit among Yb^{3+} doped RBL mediums [15].

Fig. 4.7 plots the measured crystal temperature during lasing. The inset in Fig. 4.7a displays the thermal image of the 3% Yb:YAG crystal at steady state with an input pump power of 1.2 W at 1030 nm. The red box indicates the region of interest and its temperature readout is plotted versus pixels. The temperature was uniformly distributed across the crystal. What's more, the temperature of the crystal during lasing was the same as the crystal temperature without the pump, meaning the crystal

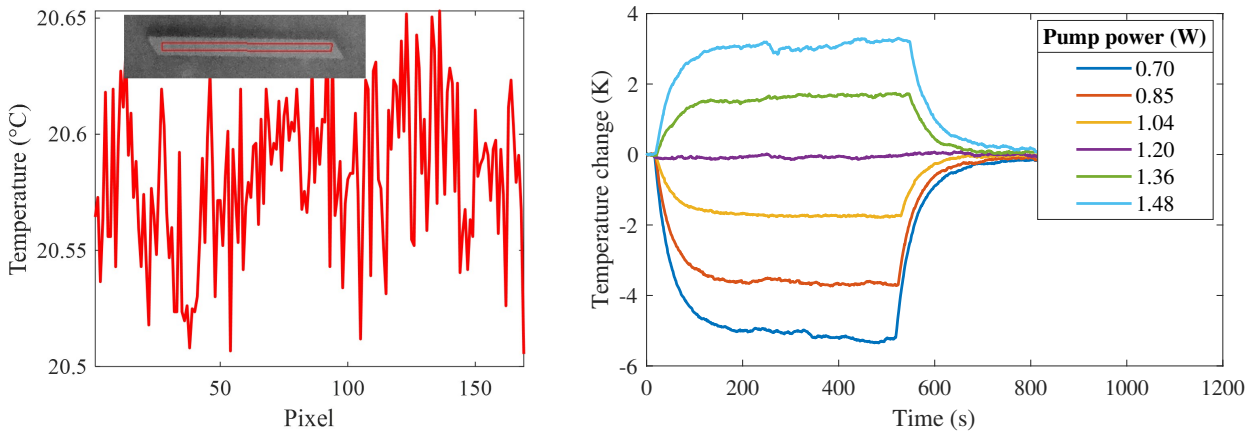

Figure 4.7: (a) Longitudinal temperature distribution of 3% Yb:YAG crystal at steady state with an input pump power of 1.2 W, which is at the balanced condition. Inset shows the thermal image of the crystal with the pump beam introduced from the left. (b) Measured temperature change of 3% Yb:YAG crystal versus time at a series of input pump powers. The temperature was averaged over the rectangle region (red box) shown in the inset thermal image. Zero temperature change was observed with an input pump power of 1.20 W. The pump was turned on at ∼10 s and was blocked at ∼500 s.

was at radiation-balanced condition (RBC), lasing without heating. The crystal temperature in the red rectangular region of interest was averaged and monitored during the measurements. Fig. 4.7b plots the averaged crystal temperature change versus time at a series of input pump powers, labeled in the legend. The pump was on at ∼20 s and was blocked at ∼500 s. When the pump was on, the presence of the pump and laser lights inside the crystal generated thermal power inside the crystal. Depending on the relative intensity of the cooing cycle and the lasing cycle, the generated thermal power can be positive or negative, leading to a temperature increase or decrease of the crystal. If the cooling cycle and lasing cycle are balanced, the thermal power is zero, which is the RBC. At RBC, the crystal temperature is the same as the room temperature. When the pump was blocked, the thermal power disappears, and the crystal temperature returned back to room temperature. For the input pump power increased from 0.7 W to 1.48 W, the steady state temperature change of the crystal during lasing was increased from -5.3 K to 3.3 K. The temperature change of the crystal at steady-state was zero with an input pump power of 1.2 W, as indicated in purple, meaning no thermal power was generated during lasing. Then the 3% Yb:YAG laser was operated at RBC with an input power of 1.2 W.

Figure 4.8a plots the scattered fluorescence collected from the 3% Yb:YAG crystal at RBC, and the peaks at 1030 nm and 1050 nm are scattered pump and laser lights, which agrees with the

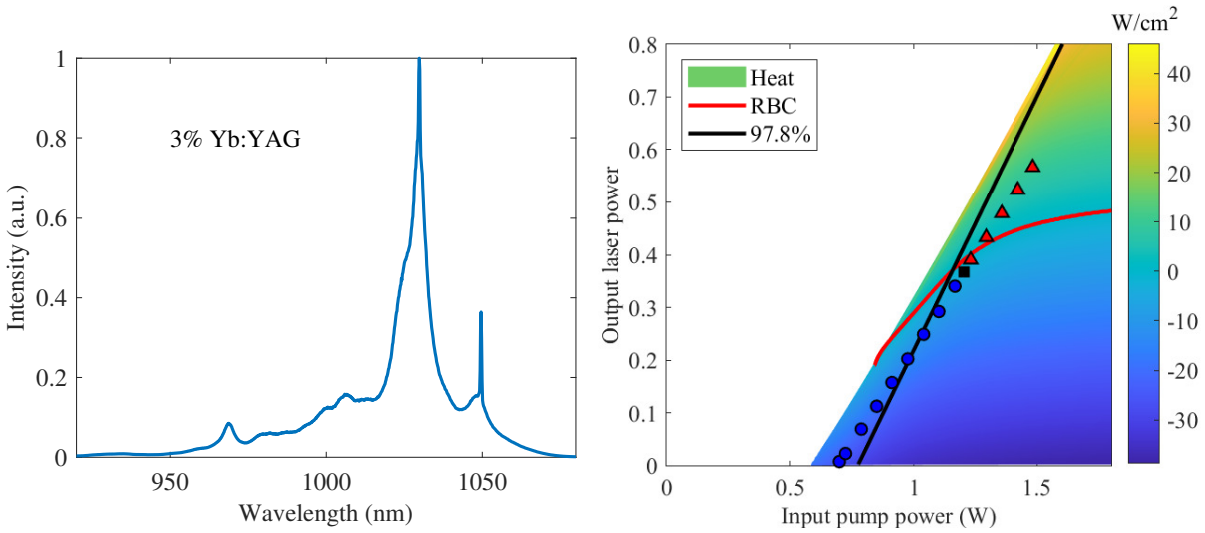

(a) (b)

Figure 4.8: (a) Side-scattered fluorescence collected from the 3% Yb:YAG at RBC. The peaks at 1030 nm and 1050 nm are scattered pump and laser lights. (b) Output laser power versus input pump power. The data points represent the measured output laser power versus input pump power. Blue circles are in the cooling regime ($\Delta T < 0$), red triangles are in the heating regime ($\Delta T > 0$), and the black square is the RBL point ($\Delta T \sim 0$). The black curve, background color, and red curve are the theoretically predicted output power versus input power, thermal intensity, and RBC with 88.3% and 97.8% reflectance at 1029.3 nm and 1048 nm. The other parameters are same as Fig. 3.22.

designed pump and laser wavelength in Subsection 3.6.2. The ring cavity was a bidirectional laser cavity, and the output laser light was experimentally observed in both directions. To measure the output laser power for both directions, the laser output power in the forward direction was measured directly (Fig. 3.26) and multiplied by a factor of 2, with the assumption that the saturated gain is the same for both directions.

In Fig. 4.8b, the solid black line plots the theoretically predicted laser output power versus input pump power. The intersection with the x-axis indicates the laser threshold. The background color is the calculated thermal intensity generated inside the crystal. Below the threshold, the laser operates along the x-axis - no laser output with increasing the input pump power. The thermal intensity inside the crystal is negative (cooling) because only the cooling cycle is occurring inside the crystal. At the threshold, the laser light starts to oscillate, and the lasing cycle appears, which generates heat inside the crystal. After the threshold, the laser output power increases with increasing input pump power, following the solid black line. With the increase of the input pump power, the lasing cycle is enhanced and turns the initial cooling to heating. At the critical input pump power, the thermal intensity is zero, meaning the laser is operated at the radiation-balanced condition (RBC).

The red curve indicates the RBC where the thermal intensity is zero. The calculated threshold is 0.77 W, and the designed RBC is achieved at an input pump power of 1.16W with a laser output power of 371 mW. The designed laser efficiency is 32.5% at RBC.

The data points in Fig. 4.8b show experimentally measured laser output power versus input pump power. The blue circles (red triangles) indicate that the crystal temperatures at steady state were below (above) room temperature (Fig. 4.7b). The back square means the crystal temperature during lasing was the same as room temperature, and the laser was operated at radiation-balanced condition (RBC). The laser threshold was measured to be 0.7W. The RBC was achieved with an input pump power of 1.2 W, and the corresponding laser output power was 367 mW. The experimentally measured laser efficiency at RBC for 3% Yb:YAG was 30.5%. The experimental measurements output laser powers (data points) are in excellent agreement with the theoretical prediction (solid black line). What's more, the observed RBC (black square) falls on the estimated RBC curve (red), and the measured laser efficiency is in excellent agreement with the predicted efficiency of 32.5%.

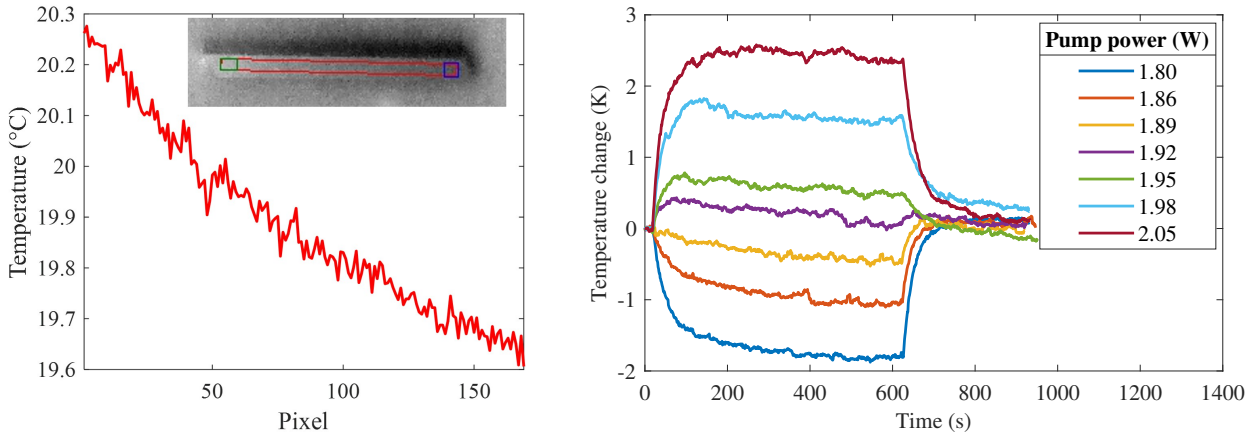

(a) (b)

Figure 4.9: (a) Longitudinal temperature distribution of 2% Yb:KYW crystal at steady state with an input pump power of 1.92 W at 1022.5 nm, which was at RBC. Inset shows the thermal camera image of the crystal with the pump beam introduced from the left. (b) Measured temperature change of 2% Yb:KYW crystal versus time at a series of input pump powers. The temperature was averaged over the rectangle region of interest (red box) shown in the inset thermal image. Zero temperature change was observed with an input pump power of 1.92 W.

For Yb:KYW, figure 4.9 plots the measured crystal temperature during lasing at various input pump powers. The inset in Fig. 4.9a shows the thermal image of the 2% Yb:KYW crystal at steady state with an input pump power of 1.92 W at 1022.5 nm. The red box indicates the region of interest, and the temperature readout is plotted versus pixels, showing the longitudinal temperature

distribution at steady state. The pump was introduced from the left into the crystal. The front part of the crystal was heating, with a temperature higher than the room temperature, while the rear part of the crystal was cooling, with a temperature lower than the room temperature. The average temperature in the region of interest was the same as room temperature, meaning the laser was operated at RBC. Fig. 4.9b plots the averaged crystal temperature change versus time at a series of input powers labeled in the legend. The pump was on at ∼20 s and was blocked at ∼600 s. For the input pump power increased from 1.80 W to 2.05 W, the steady state temperature change of the crystal was increased from −1.9 K to 2.5 K. The zero temperature change at steady-state was observed with an input pump power of 1.92 W, as plotted in purple, which means the laser was operated at RBC. Then the 2% Yb:KYW was operated at RBC with an input power of 1.92 W.

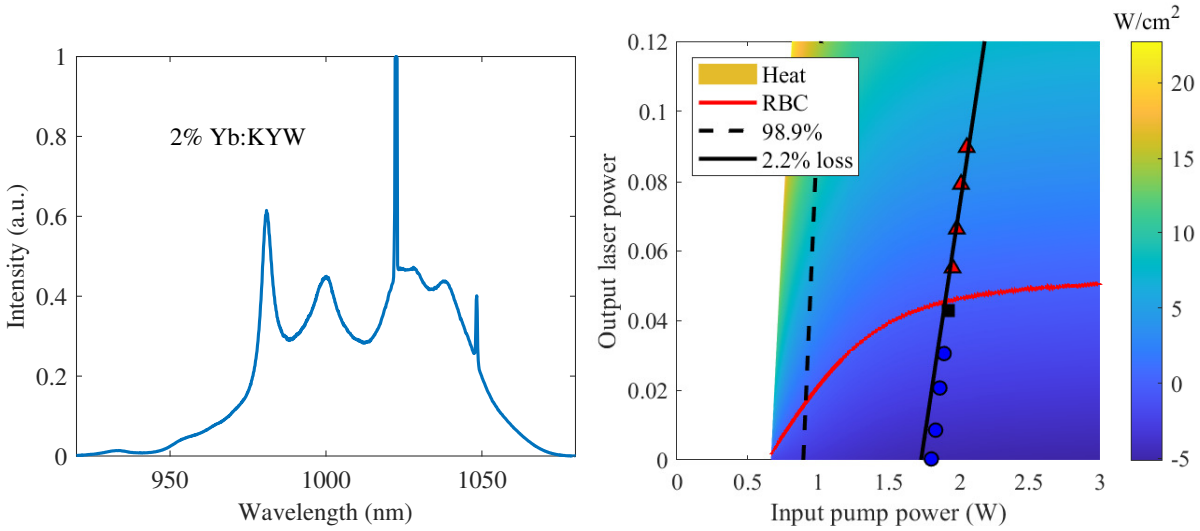

Figure 4.10: (a) Side-scattered fluorescence collected from the 2% Yb:KYW at RBC. The peaks at 1022.5 nm and 1050 nm are scattered pump and laser light. (b) The data points represent the measured output laser power versus input pump power. Blue circles are in the self-cooling regime ($\Delta T < 0$), red triangles are in the heating regime ($\Delta T > 0$), and the black square is the RBL point ($\Delta T \sim 0$). The dashed black curve, background color, and red curve are the theoretically predicted output power versus input power, thermal intensity, and RBC with 81.3% and 98.9% reflectance at 1022.5 nm and 1050 nm. The black curve is the calculated output power with an inclusion of 2.2% loss in the cavity. The other parameters are same as Fig. 3.25.

Figure 4.10a plots the scattered fluorescence collected from the 2% Yb:KYW crystal at RBC, and the peaks at 1022.5 nm and 1050 nm are scattered pump and laser light, which agrees with the predicted pump and laser wavelength in Subsection 3.6.2. The measured laser output power in the forward direction was multiplied by a factor of 2 to calculate the output laser power for both directions. In Fig. 4.10b, the dashed black line shows the theoretically predicted laser out-

put power versus input pump power, with 98.9% reflectance for the output coupler. The background color is the calculated thermal intensity generated inside the crystal. The red indicates the radiation-balanced operation. The 2% Yb:KYW crystal was post polished to have the Brewster angle surface in order to fit in the ring cavity. However, the polished surfaces were neither parallel to each other nor perpendicular to the crystal lateral sides. An 0.65% reflection from the Brewster angle and a deflection of the transmitted beam was observed experimentally when the cavity was aligned. Hence an additional 2.2% loss was included to recalculate the laser output power versus input pump power, which is plotted as the solid black line. The intersection with the x-axis is the laser threshold, and the intersection with the red curve is the radiation-balanced operation. The calculated threshold is 1.73 W, and the RBC is achieved at an input power of 1.9 W with an output laser power of 45 mW.

The data points in 4.10b show the experimentally measured laser output power versus input pump power. The blue circles (red triangles) indicate that the crystal temperature at steady state was below (above) room temperature (Fig. 4.7b). The back square means the crystal temperature during lasing was unchanged (RBC). The laser threshold was measured to be 1.8 W. The RBC was achieved with an input pump power of 1.92W, and the corresponding laser output power was 42.7 mW. The experimentally measured laser efficiency at RBC for 2% Yb:KYW was 2.2%. The experimental measurements output laser powers (data points) are in good agreement with the theoretical prediction with an additional 2.2% cavity loss (solid black line). The observed RBC (black square) falls on the estimated RBC curve (red), and the measured laser efficiency was 2.2%, which is in excellent agreement with the designed efficiency of 1.8%.

Due to the large temperature difference across the 2% Yb:KYW crystal at RBC, the temperature change at two ends of the crystal for radiation-balanced operation, together with the average, are plotted in Fig. 4.11. The input pump power was 1.92 W. The pump was on at $\sim$20 s and was blocked at $\sim$600 s. The inset shows the thermal image of the crystal, with the colored boxes indicating the region of averaging. The pump was introduced from the left. When the pump was on, the front part (green) heated while the rear portion cooled. The temperature difference remained during lasing, even at the steady state. When the pump was blocked, the temperature difference between the two ends disappeared, and the crystal returned to room temperature. This observed temperature difference agrees with the predicted thermal intensity tendency along the crystal (Fig. 2.7 in Subsection 2.3.2). As discussed in Subsection 2.3.2, when the light fields propagate through the RBL medium, thermal balanced is not maintained at every position of the crystal. One part is heating, and the other is cooling, but the overall thermal power is zero at RBC, leading to an average zero temperature change. This phenomenon is enhanced with a higher doping density [24] or a slower thermal diffusion rate in the longitudinal direction. For higher doped crystals, the intensities vary rapidly across the crystal, leading to a steep slope of the thermal density along the

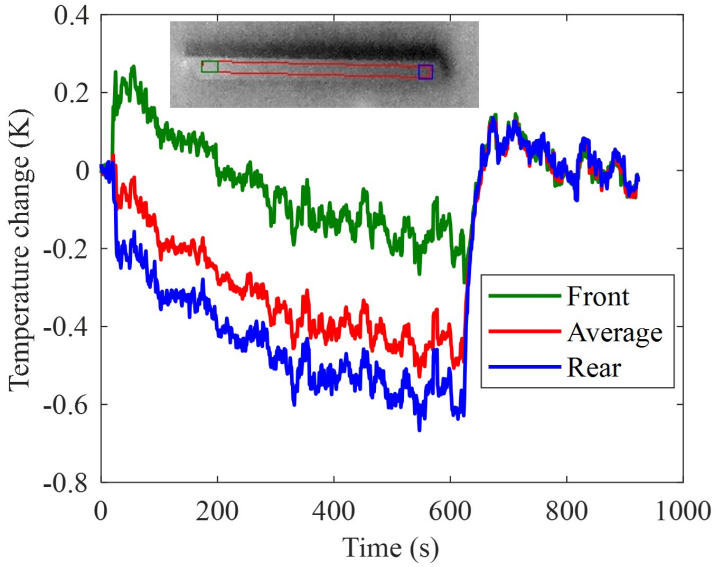

Figure 4.11: Temperature change of two ends of 2% Yb:KYW crystal at RBC. Inset shows the thermal image and pump beam was introduced from the left. The green, red and blue rectangular indicates the region of average.

crystal. The thermal conductivity and geometry cross section both limit the thermal diffusion rate in the longitudinal direction, which increases the temperature difference between the two ends. YAG has a higher thermal conductivity compared with KYW, so the temperature distribution is more uniform in Yb:YAG crystal (Fig. 4.7a and Fig. 4.9a). A less doped crystal or a larger cross sectional area can be used to achieve a more uniform temperature distribution across the Yb:KYW crystal.

The theoretical prediction, which includes the saturable absorption of impurities, agrees well with the experimental measurements, especially the thermal balanced condition. This agreement demonstrates the saturation of the background absorption in RBLs. The differential absorption saturation enables the inclusion of the background absorption in RBLs, providing an accurate prediction of radiation-balanced operation and unifying the treatment of background absorption in laser cooling and RBLs.

The laser efficiency for 2% Yb:KYW is 2.2%, which is much lower than Yb:YAG. There are several reasons for the low laser efficiency. First, the cooling power for 2% Yb:KYW is low because of the strong reabsorption of fluorescence and high background absorption coefficient (Section 4.2). Second, the pump wavelength was not ideal. The cooling power at 1022.5 nm is only half of the value at 1030 nm. leading to reduced cooling power. Third, the laser wavelength was large red-shifted. The laser wavelength for the achieved RBL was 1050 nm, not the on resonance 1039.6 nm, which dramatically reduces the laser efficiency. Finally, the cavity was not an

impedance-matched cavity. The reflectivity at the pump and laser wavelengths was not ideal, and a large portion of the input pump beam was reflected rather than absorbed. Though the achieved laser efficiency was low in lack of ideal 1% crystal and custom-designed mirror. Correction of these deficiencies should enable high quality Gaussian output at the 5 W level with 18% efficiency in existing commercial 1% Yb:KYW samples. Even better performance of this new self-cooled laser could result from improved crystal growth efforts.

The RBL was achieved in the impure 2% Yb:KYW crystal, with a background absorption of $(9.4 \pm 1.2) \times 10^{-4}$ cm^{-1}. This is the first time that RBL is achieved in Yb:KYW crystals, which was found to have the highest figure of merit among Yb^{3+} doped materials [15] for RBLs. What's more, this is an example that the differential absorption saturation theory extends RBL operation to impure materials, which expands the material selection for both laser cooling and RBLs.

By using the pump locking technique and impedance-matched cavity, the achieved laser efficiency for Yb:YAG is 30.5 %, which is the highest among all RBLs. Recall that the efficiency is only 4% for this crystal with a signal pass setup. This measured efficiency demonstrated the advantages of the pump locking technique. This pump-locked cavity dramatically increases the laser efficiency by a total absorption of the pump power and reduced the required input power to achieve RBL.

The efficiency of 30.5% was achieved for 3% Yb:YAG crystal with a 20 nm separation of the pump and laser wavelength. According to Eq. 3.8, the laser efficiency increased with reducing the separation. For example, an efficiency of more than 50% is predicted if the separation between the pump and laser wavelengths is reduced to 10 nm. By introducing a wavelength-dependent loss into the laser cavity, the output wavelength can be tuned, and a much higher laser efficiency at RBC can be achieved.

For the current cavity design, the beam radius inside the laser medium is below 100 μm. The RBL can be scaled to high power operation by increasing both the input power and beam radius while maintaining the required intensity. The pump locking technique used in this work can also be used in high power operation since the intensity is not increased with the power for RBL. What's more, when the cavity is designed to be a degenerate cavity [73], the total absorption can be achieved for a pump with an arbitrary wavefront. This means that the cavity can be pumped with multiple pump sources. Then the RBL can be used to convert multiple high power beams with arbitrary wavefront to a single wavelength-tunable beam with a fundamental mode and a high converting efficiency.

CHAPTER 5

Conclusion and Future work

This chapter presents the conclusions and future directions for this research. The first section summarizes the four main sets of experiments outlined in the Theory, Experiments, and Results Chapters: thermal isolation of supports, cooling with Yb-doped materials, improved cooling efficiency using optical saturation, and radiation-balanced lasers. The second section briefly outlines the potential extension of this work to lower temperature cooling and high power radiation-balanced operation.

5.1 Summary and Significance of Contributions

This research aimed to demonstrate improvement to the current anti-Stokes fluorescence (ASF) cooling method and investigate new materials for radiation-balanced lasers (RBLs). In this thesis, theoretical advances and experimental realizations have been presented for the improved performance of optical refrigeration through optical saturation and quantitative predictions of radiation-balanced operations by the inclusion of impurity absorption.

The heat transfer between the laser-cooled crystal and the surrounding environment, especially the support, was investigated. The combined experimental and simulated results (Figs. 4.1, 4.2 and 4.3) confirm that better thermal isolation and greater uniformity of temperature can be achieved with the use of aerogel supports despite the large contact area. The aerogel supports are suggested for both laser cooling and RBL experiments for thermal isolation and uniformity.

Initial experimental studies began with the Yb:YAG and Yb:KYW crystals. The results were summarized in Table 4.1 with a comparison of fitted values for external quantum efficiency η_{EQE} and background absorption coefficient α_b. The 3% Yb:YAG sample performed the best due to its high purity, and record cooling of 3.5 K/W was achieved in open-air lab conditions. Reduced cooling power was observed in Yb:KYW samples because of the high background absorption coefficient. For Yb:KYW samples of various doping concentrations, results verified that cooling power was reduced for higher concentrations of Yb^{3+} due to fluorescence re-absorption. Moreover,

net cooling in this material was shown for the first time, paving the way for radiation-balanced lasing in commercially-available tungstate crystals.

As the main limitation of ASF cooling, background impurity absorption is critical to minimize in order to reach lower temperatures with this method. Intensity-dependent theoretical and experimental analyses were performed for 10%Yb:YLF to reveal the advantages of differential absorption saturation. In Section 2.2.2, it was shown that lower minimum achievable temperatures are theoretically possible whenever the saturation intensity of background absorption is less than that of the coolant ions. Experimental results using (Fig. 4.6) showed that elevated cooling efficiencies are obtained in this situation at wavelengths longer than 1000 nm, consistent with the theoretical predictions. Measurements showed that the cooling efficiency doubled with increased pump intensity near 1035 nm, a phenomenon ascribed to the low saturation intensity of the dominant impurity, thought to be trivalent iron. A novel method was devised to measure the saturation intensities of background and coolant ions that confirmed an unexpectedly low value of background saturation intensity in the range of this wavelength. Thus, saturation accounted for the intensity-dependent cooling efficiencies observed in this work, consistent with the analysis. The results and model developed here also predict that stable RBL operation should be achievable in relatively impure laser materials, like Yb:KYW, including some that do not even show net cooling at low intensities. Hence this finding improves the prospects for RBLs in a much wider variety of laser hosts.

An original method was introduced to determine the saturation intensity of background absorption in a 10% Yb:YLF crystal. The technique makes use of systematic measurements of laser cooling efficiency by differential luminescence thermometry (DLT) as a function of wavelength and incident intensity. Results revealed a wavelength at which all cooling efficiency curves intersected, regardless of intensity. The crossing point observed at $\lambda_{cr} = 1000$ nm in 10% Yb:YLF indicated that the cooling efficiencies were independent of intensity at this wavelength. Consequently, the saturation intensity of Yb^{3+}, which varied strongly with detuning from resonance, had to be equal to the saturation intensity of the background species there. This meant that the background saturation intensity could be computed from the analytic expression for the coolant ions at the unique wavelength λ_{cr} (yielding $I_b = I_r(\lambda_{cr}) = 2.6 \times 10^4\ W/\mathrm{cm}^2$). For $\lambda > \lambda_{cr}$, higher pump intensities improved the cooling efficiency significantly. These results on the role of background impurity saturation affirmed that ASF cooling could be improved with higher pump intensity in some materials and demonstrated the first post-growth method to enhance the cooling efficiency of crystalline solids.

The pump locking technique was introduced when designing the radiation-balanced lasers (RBLs). The laser cavity is locked to the pump, and both the pump and laser lights oscillate inside the cavity, which improved the mode-match between the pump and laser. What's more, by recycling the unabsorbed pump inside the laser cavity, this technique reduced the required input

pump power and significantly improved the laser efficiency at radiation-balanced operation, which benefits from the total absorption of the impedance-matched resonant cavity.

The background impurity absorption, the key limitation of laser cooling, was included in the RBL theory, and quantitative predictions of the required conditions for radiation balance were presented. Radiation-balanced laser operation was achieved in Yb:YAG and this laser achieved the highest efficiency level (30.5%) of any self-cooled laser operated to date. Threshold levels, output power, and the input power at the radiation balance point are all shown to be in close agreement with the theory with the inclusion of saturable background impurity absorption. Radiation-balanced lasing is also achieved for the first time in the tungstate crystal Yb:KYW, despite having very high impurity content. This achievement further demonstrated the differential absorption saturation improved the performance of both laser cooling and RBLs, extending the material selection to impure materials.

5.2 Future Work

The background impurity absorption was found to saturate before the coolant Yb^{3+} ion in Yb:YLF crystal, leading to an improved cooling efficiency near room temperature. And Yb:YLF maintains the record temperature of 87 K [27]. The intensity-dependent background absorption at 87 K is a promising direction to investigate. If the background saturates before the Yb^{3+} at 87 K, a cooling temperature lower than that can be achieved by increasing the pump intensity.

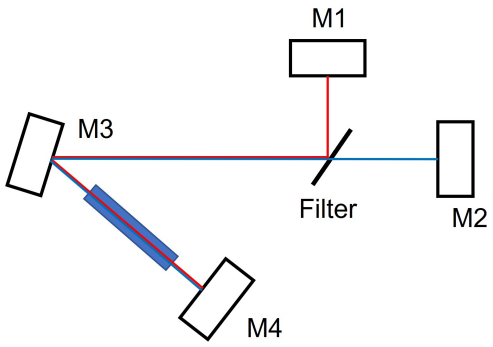

Figure 5.1: Modified four mirror cavity for radiation-balanced lasers. The blue line indicates the pump path, and red is the laser path. M1 and M2 are output and input couplers, respectively. M3 and M4 are curved mirrors to compensate for the aberration introduced by the Brewster angle.

The radiation-balanced laser presented in this work was operated at a low power level, since the beam waist inside the crystal was below 100 μm. The high power operation is another direction for further work by increasing the beam size inside the crystal. The four mirror ring cavity used in this work suffered from the lack of availability of custom mirror coatings. Instead of splitting the

pump and laser outside the cavity, a sharp filter can be placed inside the cavity, as shown in Fig. 5.1. Then, the filter separates the pump and laser paths inside the cavity, which lifts the restrictions for custom coated mirrors with wavelength-dependent reflectance. What's more, since the pump and laser are oscillating in the same cavity, the laser efficiency is still enhanced due to the pump locking technique. The laser wavelength can be tuned and stabled by inserting an etalon in the laser path and tuning the output mirror with a piezo.

Recently, the total absorption was achieved for a pump with arbitrary wavefront using a degenerated cavity [73]. This can be used in radiation-balanced laser to achieve total absorption of multiple pump sources with arbitrary wavefront. Then the RBL can be used to convert multiple high power beams with arbitrary wavefront to a single wavelength-tunable beam with a fundamental mode and a high converting efficiency.

APPENDIX A

Crystal Orientation of Yb:YLF

A Laue x-ray diffraction pattern was recorded to determine the orientation of the crystalline sample in this work. Figure A.1 shows the reflected diffraction pattern and the simulated pattern based on the lattice parameters of single crystal YLF. Excellent agreement was found between the measured and simulated patterns, confirming both the composition and orientation of the crystal. The lack of distortion in Laue spots confirmed the single crystal nature of the sample and the absence of internal stress. The orientation of crystal axes with respect to the faces of the cut and polished sample are illustrated in Figure A.2.

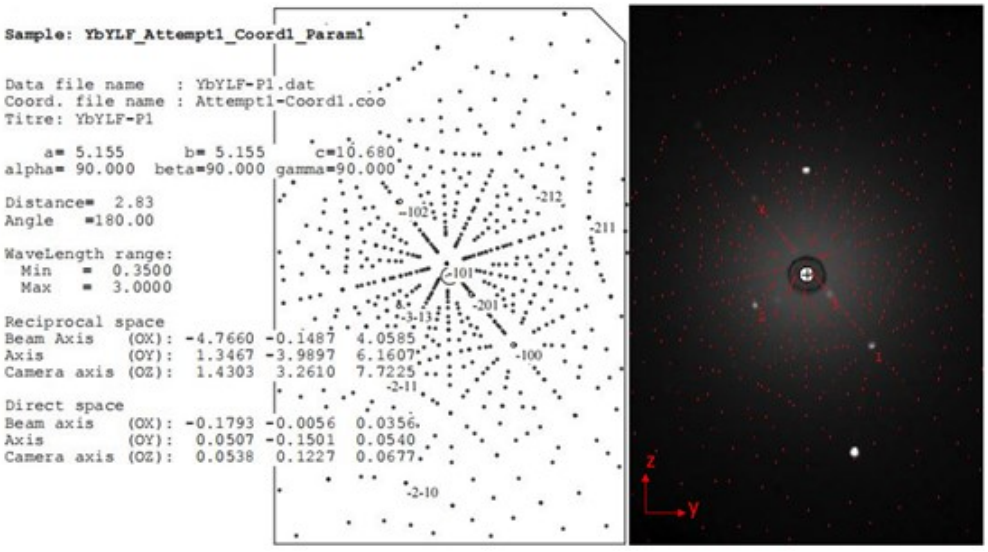

Figure A.1: Simulated and measured Laue diffraction pattern. The excellent agreement confirms the crystal type and orientation.

The sample was polished to maintain 3 pairs of parallel surfaces and the lab frame coordinates x, y, z correspond to normals to various surfaces as indicated in Fig. A.2. Axes x, y, and z were parallel to the 5.1 mm, 3.4 mm, 5.6 mm sample edges, respectively. The pump laser propagated along y, with a polarization parallel to x for laser cooling measurements. The unit vectors of axes

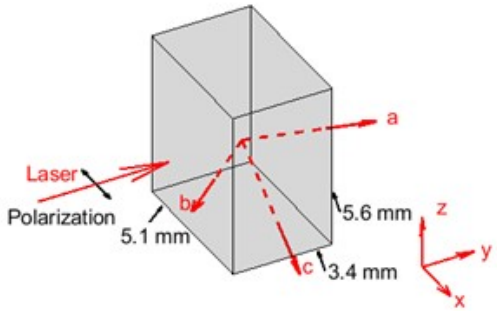

Figure A.2: The crystal orientation and crystal cut. The crystal axes are indicated by the rotation matrix.

x, y, and z are defined to be

$$\hat{\mathbf{x}} = \begin{bmatrix} 1 \\ 0 \\ 0 \end{bmatrix}, \hat{\mathbf{y}} = \begin{bmatrix} 0 \\ 1 \\ 0 \end{bmatrix}, \hat{\mathbf{z}} = \begin{bmatrix} 0 \\ 0 \\ 1 \end{bmatrix}. \tag{A.1}$$

The crystal axes are related to the lab frame by the rotation equation

$$\begin{bmatrix} a \\ b \\ c \end{bmatrix} = R \begin{bmatrix} x \\ y \\ z \end{bmatrix}, \tag{A.2}$$

where

$$R = R_z(\gamma) R_y(\beta) R_x(\alpha), \tag{A.3}$$

where

$$R_x(\alpha) = \begin{bmatrix} 1 & 0 & 0 \\ 0 & \cos(\alpha) & -\sin(\alpha) \\ 0 & \sin(\alpha) & \cos(\alpha) \end{bmatrix}, \tag{A.4}$$

$$R_y(\beta) = \begin{bmatrix} \cos(\beta) & 0 & \sin(\beta) \\ 0 & 1 & 0 \\ -\sin(\beta) & 0 & \cos(\beta) \end{bmatrix}, \tag{A.5}$$

$$R_z(\gamma) = \begin{bmatrix} \cos(\gamma) & -\sin(\gamma) & 0 \\ \sin(\gamma) & \cos(\gamma) & 0 \\ 0 & 0 & 1 \end{bmatrix} \tag{A.6}$$

represent rotations of α, β, γ about axes x, y, z. The Euler angles α, β, γ were 181.8°, 337.7°,

38.6°, respectively and the calculated rotation matrix was

$$R = \begin{bmatrix} 0.7231 & 0.6326 & 0.2774 \\ 0.5767 & -0.7739 & 0.2614 \\ 0.3802 & -0.0289 & -0.9245 \end{bmatrix}. \tag{A.7}$$

The unit vectors of crystal axes a, b, c were therefore

$$\hat{\mathbf{a}} = R \cdot \hat{\mathbf{x}} = \begin{bmatrix} 0.7231 \\ 0.5767 \\ 0.3802 \end{bmatrix}, \tag{A.8}$$

$$\hat{\mathbf{b}} = R \cdot \hat{\mathbf{y}} = \begin{bmatrix} 0.6326 \\ -0.7739 \\ -0.0289 \end{bmatrix}, \tag{A.9}$$

$$\hat{\mathbf{c}} = R \cdot \hat{\mathbf{z}} = \begin{bmatrix} 0.2774 \\ 0.2614 \\ -0.9245 \end{bmatrix}. \tag{A.10}$$

BIBLIOGRAPHY

[1] Peter Pringsheim. Zwei bemerkungen über den unterschied von lumineszenz-und temperaturstrahlung. *Zeitschrift für Physik*, 57(11):739–746, 1929.

[2] L Landau et al. On the thermodynamics of photoluminescence. *J. Phys.(Moscow)*, 10(503), 1946.

[3] Alfred Kastler. Quelques suggestions concernant la production optique et la détection optique d'une inégalité de population des niveaux de quantifigation spatiale des atomes. application à l'expérience de stern et gerlach et à la résonance magnétique. *J. phys. radium*, 11(6):255–265, 1950.

[4] Richard I Epstein, Melvin I Buchwald, Bradley C Edwards, Timothy R Gosnell, and Carl E Mungan. Observation of laser-induced fluorescent cooling of a solid. *Nature*, 377(6549):500–503, 1995.

[5] Seth D Melgaard, Alexander R Albrecht, Markus P Hehlen, and Mansoor Sheik-Bahae. Solid-state optical refrigeration to sub-100 kelvin regime. *Scientific reports*, 6(1):1–6, 2016.

[6] Markus P Hehlen, Junwei Meng, Alexander R Albrecht, Eric R Lee, Aram Gragossian, Steven P Love, Christopher E Hamilton, Richard I Epstein, and Mansoor Sheik-Bahae. First demonstration of an all-solid-state optical cryocooler. *Light: Science & Applications*, 7(1):1–10, 2018.

[7] Steven R Bowman. Lasers without internal heat generation. *IEEE journal of quantum electronics*, 35(1):115–122, 1999.

[8] Steven R Bowman, Shawn P O'Connor, Subrat Biswal, Nicholas J Condon, and Armand Rosenberg. Minimizing heat generation in solid-state lasers. *IEEE journal of quantum electronics*, 46(7):1076–1085, 2010.

[9] Zhou Yang, Junwei Meng, Alexander R Albrecht, and Mansoor Sheik-Bahae. Radiation-balanced Yb:YAG disk laser. *Optics express*, 27(2):1392–1400, 2019.

[10] J Knall, Magnus Engholm, T Boilard, M Bernier, P-B Vigneron, N Yu, PD Dragic, J Ballato, and MJF Digonnet. Radiation-balanced silica fiber laser. *Optica*, 8(6):830–833, 2021.

[11] Markus P Hehlen, Richard I Epstein, and Hiroyuki Inoue. Model of laser cooling in the Yb^{3+}-doped fluorozirconate glass zblan. *Physical Review B*, 75(14):144302, 2007.

[12] J Fernandez, A Mendioroz, AJ Garcia, R Balda, and JL Adam. Anti-stokes laser-induced internal cooling of Yb^{3+}-doped glasses. *Physical Review B*, 62(5):3213, 2000.

[13] Joaquin R Fernandez, A Mendioroz, Rolindes Balda, M Voda, M Al-Saleh, AJ Garcia-Adeva, Jean-Luc Adam, and Jacques Lucas. Origin of laser-induced internal cooling of Yb^{3+}-doped systems. In *Rare-Earth-Doped Materials and Devices VI*, volume 4645, pages 135–147. SPIE, 2002.

[14] A Mendioroz, J Fernandez, M Voda, M Al-Saleh, R Balda, and AJ Garcia-Adeva. Anti-stokes laser cooling in Yb^{3+}-doped KPb_2Cl_5 crystal. *Optics Letters*, 27(17):1525–1527, 2002.

[15] SR Bowman and CE Mungan. New materials for optical cooling. *Applied Physics B*, 71(6):807–811, 2000.

[16] CE Mungan, SR Bowman, and TR Gosnell. Solid-state laser cooling of ytterbium-doped tungstate crystals. Technical report, NAVAL ACADEMY ANNAPOLIS MD DEPT OF PHYSICS, 2001.

[17] James V Guiheen, Chris D Haines, George H Sigel, Richard I Epstein, Jared Thiede, and Wendy M Patterson. Yb^{3+} and Tm^{3+}-doped fluoroaluminate classes for anti-stokes cooling. *Physics and Chemistry of Glasses-European Journal of Glass Science and Technology Part B*, 47(2):167–176, 2006.

[18] Richard I Epstein, JJ Brown, Bradley C Edwards, and A Gibbs. Measurements of optical refrigeration in ytterbium-doped crystals. *Journal of Applied Physics*, 90(9):4815–4819, 2001.

[19] Mostafa Peysokhan, Saeid Rostami, Esmaeil Mobini, Alexander R Albrecht, Stefan Kuhn, Sigrun Hein, Christian Hupel, Johannes Nold, Nicoletta Haarlammert, Thomas Schreiber, et al. Laser-induced anti-stokes fluorescence cooling of ytterbium-doped silica glass by more than 6 kelvin. *arXiv preprint arXiv:2011.11224*, 2020.

[20] Stefano Bigotta, Daniela Parisi, Lucia Bonelli, Alessandra Toncelli, Alberto Di Lieto, and Mauro Tonelli. Laser cooling of Yb^{3+}-doped BaY_2F_8 single crystal. *Optical Materials*, 28(11):1321–1324, 2006.

[21] Bradley C Edwards, Johnny E Anderson, Richard I Epstein, Gary L Mills, and Allan J Mord. Demonstration of a solid-state optical cooler: an approach to cryogenic refrigeration. *Journal of Applied Physics*, 86(11):6489–6493, 1999.

[22] J Thiede, J Distel, SR Greenfield, and RI Epstein. Cooling to 208 k by optical refrigeration. *Applied Physics Letters*, 86(15):154107, 2005.

[23] Laura B Andre, Long Cheng, Alexander J Salkeld, Luis HC Andrade, Sandro M Lima, Junior R Silva, and Stephen C Rand. Laser cooling under ambient conditions in Yb^{3+}:KYW. In *Photonic Heat Engines: Science and Applications*, volume 10936, pages 32–39. SPIE, 2019.

[24] Long Cheng, Laura B Andre, Alexander J Salkeld, Luis HC Andrade, Sandro M Lima, Junior R Silva, Daniel Rytz, and Stephen C Rand. Laser cooling of Yb^{3+}:KYW. *Optics Express*, 28(3):2778–2788, 2020.

[25] Biao Zhong, Yongqing Lei, Hao Luo, Yanling Shi, Tao Yang, and Jianping Yin. Laser cooling of the Yb^{3+}-doped $LuLiF_4$ single crystal for optical refrigeration. *Journal of Luminescence*, 226:117472, 2020.

[26] Aram Gragossian, Mohammadreza Ghasemkhani, Junwei Meng, AR Albrecht, Mauro Tonelli, and Mansoor Sheik-Bahae. Optical refrigeration inches toward liquid-nitrogen temperatures. *SPIE newsroom*, pages 2–4, 2017.

[27] Azzurra Volpi, Junwei Meng, Aram Gragossian, Alexander R Albrecht, Saeid Rostami, Alberto Di Lieto, Richard I Epstein, Mauro Tonelli, Markus P Hehlen, and Mansoor Sheik-Bahae. Optical refrigeration: the role of parasitic absorption at cryogenic temperatures. *Optics Express*, 27(21):29710–29718, 2019.

[28] Chad William Hoyt. *Laser cooling in thulium-doped solids*. The University of New Mexico, 2003.

[29] Saeid Rostami. *Mid-IR Optical Refrigeration and Radiation Balanced Lasers*. PhD thesis, The University of New Mexico, 2020.

[30] Joaquin Fernandez, Angel J Garcia-Adeva, and Rolindes Balda. Anti-stokes laser cooling in bulk erbium-doped materials. *Physical review letters*, 97(3):033001, 2006.

[31] Saeid Rostami, Alexander R Albrecht, Azzurra Volpi, and Mansoor Sheik-Bahae. Observation of optical refrigeration in a holmium-doped crystal. *Photonics Research*, 7(4):445–451, 2019.

[32] Saeid Rostami and Mansoor Sheik-Bahae. Observation of optical refrigeration in ho: Byf crystal. In *Photonic Heat Engines: Science and Applications III*, volume 11702, page 1170205. SPIE, 2021.

[33] Bradley C Edwards, Melvin I Buchwald, Richard I Epstein, Timothy R Gosnell, and Carl E Mungan. Development of a fluorescent cryocooler. Technical report, Los Alamos National Lab.(LANL), Los Alamos, NM (United States), 1995.

[34] Denis V Seletskiy, Richard Epstein, and Mansoor Sheik-Bahae. Laser cooling in solids: advances and prospects. *Reports on Progress in Physics*, 79(9):096401, 2016.

[35] GL Mills, AJ Mord, and PA Slaymaker. Design and predicted performance of an optical cryocooler for a focal plane application. In *Cryocoolers 11*, pages 613–620. Springer, 2002.

[36] Erin Pettyjohn. Cryocoolers for microsatellite military applications. Georgia Institute of Technology, 2008.

[37] Rémi Vicente, Gilles Nogues, Jean-Michel Niot, Thierry Wiertz, Pierre Contini, and Arnaud Gardelein. Impacts of laser cooling for low earth orbit observation satellites: An analysis in terms of size, weight and power. *Cryogenics*, 105:103000, 2020.

[38] Giovanni Cittadino, Eugenio Damiano, Alberto Di Lieto, and Mauro Tonelli. First demonstration of optical refrigeration efficiency greater than 4% at room temperature. *Optics Express*, 28(10):14476–14489, 2020.

[39] Simon Nagel, Bernd Metzger, Tina Gottwald, Vincent Kuhn, Alexander Killi, and Sven-Silvius Schad. Thin disk laser operating in fundamental mode up to a power of 4kw. In *The European Conference on Lasers and Electro-Optics*, page ca_5_4. Optical Society of America, 2019.

[40] Simon Nagel, Bernd Metzger, Dominik Bauer, Johanna Dominik, Tina Gottwald, Vincent Kuhn, Alexander Killi, Thomas Dekorsy, and Sven-Silvius Schad. Thin-disk laser system operating above 10 kw at near fundamental mode beam quality. *Optics Letters*, 46(5):965–968, 2021.

[41] Baolai Yang, Peng Wang, Hanwei Zhang, Xiaoming Xi, Chen Shi, Xiaolin Wang, and Xiaojun Xu. 6 kw single mode monolithic fiber laser enabled by effective mitigation of the transverse mode instability. *Optics Express*, 29(17):26366–26374, 2021.

[42] Jay W Dawson, Michael J Messerly, Raymond J Beach, Miroslav Y Shverdin, Eddy A Stappaerts, Arun K Sridharan, Paul H Pax, John E Heebner, Craig W Siders, and CPJ Barty. Analysis of the scalability of diffraction-limited fiber lasers and amplifiers to high average power. *Optics express*, 16(17):13240–13266, 2008.

[43] Tino Eidam, Christian Wirth, Cesar Jauregui, Fabian Stutzki, Florian Jansen, Hans-Jürgen Otto, Oliver Schmidt, Thomas Schreiber, Jens Limpert, and Andreas Tünnermann. Experimental observations of the threshold-like onset of mode instabilities in high power fiber amplifiers. *Optics express*, 19(14):13218–13224, 2011.

[44] Denis V Seletskiy, Seth D Melgaard, Stefano Bigotta, Alberto Di Lieto, Mauro Tonelli, and Mansoor Sheik-Bahae. Laser cooling of solids to cryogenic temperatures. *Nature Photonics*, 4(3):161–164, 2010.

[45] SR Bowman. Optimizing average power in low quantum defect lasers. *Applied Optics*, 54(31):F78–F84, 2015.

[46] Mansoor Sheik-Bahae and Zhou Yang. Optimum operation of radiation-balanced lasers. *IEEE Journal of Quantum Electronics*, 56(1):1–9, 2019.

[47] Nouredine Zettili. Quantum mechanics: concepts and applications, 2003.

[48] Hendrik Antoon Kramers. Théorie générale de la rotation paramagnétique dans les cristaux. *Proc. Acad. Amst*, 33(6), 1930.

[49] NV Kuleshov, AA Lagatsky, AV Podlipensky, VP Mikhailov, and G Huber. Pulsed laser operation of Yb-doped $KY(WO_4)_2$ and $KGd(WO_4)_2$. *Optics letters*, 22(17):1317–1319, 1997.

[50] Laura B Andre, Long Cheng, and Stephen C Rand. Saturation, allowed transitions and quantum interference in laser cooling of solids. *Applied Sciences*, 12(3):953, 2022.

[51] Long Cheng, Laura B Andre, Gabriela L Almeida, Luis HC Andrade, Sandro M Lima, Junior R Silva, Tomaz Catunda, Yannick Guyot, and Stephen C Rand. Differential absorption saturation in laser cooled Yb: $LiYF_4$. *Optical Materials*, 128:112404, 2022.

[52] Stefan Püschel, Sascha Kalusniak, Christian Kränkel, and Hiroki Tanaka. Temperature-dependent radiative lifetime of Yb:YLF: refined cross sections and potential for laser cooling. *Optics Express*, 29(7):11106–11120, 2021.

[53] Seth Melgaard, Denis Seletskiy, Victor Polyak, Yemane Asmerom, and Mansoor Sheik-Bahae. Identification of parasitic losses in Yb:YLF and prospects for optical refrigeration down to 80k. *Optics Express*, 22(7):7756–7764, 2014.

[54] GB Scott, DE Lacklison, and JL Page. Absorption spectra of $Y_3Fe_5O_{12}$ (YIG) and $Y_3Ga_5O_12$:Fe^{3+}. *Physical Review B*, 10(3):971, 1974.

[55] JR Silva, LHC Andrade, SM Lima, Y Guyot, N Giannini, and M Sheik-Bahae. Investigation of allowed and forbidden electronic transitions in rare earth doped materials for laser cooling application by thermal lens spectroscopy. *Optical Materials*, 95:109195, 2019.

[56] DE McCumber. Einstein relations connecting broadband emission and absorption spectra. *Physical Review*, 136(4A):A954, 1964.

[57] Elton Soares de Lima Filho, Galina Nemova, Sébastien Loranger, and Raman Kashyap. Laser-induced cooling of a Yb:YAG crystal in air at atmospheric pressure. *Optics Express*, 21(21):24711–24720, 2013.

[58] Denis V Seletskiy, Seth D Melgaard, Alberto Di Lieto, Mauro Tonelli, and Mansoor Sheik-Bahae. Laser cooling of a semiconductor load to 165 k. *Optics Express*, 18(17):18061–18066, 2010.

[59] RL Aggarwal, DJ Ripin, JR Ochoa, and TY Fan. Measurement of thermo-optic properties of $Y_3Al_5O_{12}$, $Lu_3Al_5O_{12}$, $YAlO_3$, $LiYF_4$, $LiLuF_4$, BaY_2F_8, $KGd(WO_4)_2$, and $KY(WO_4)_2$ laser crystals in the 80–300 k temperature range. *Journal of Applied Physics*, 98(10):103514, 2005.

[60] Andreas Freise and Kenneth Strain. Interferometer techniques for gravitational-wave detection. *Living Reviews in Relativity*, 13(1):1–81, 2010.

[61] PW Smith and EH Turner. A bistable fabry-perot resonator. *Applied Physics Letters*, 30(6):280–281, 1977.

[62] H Kogelnik, E Ippen, Andrew Dienes, and C V Shank. Astigmatically compensated cavities for cw dye lasers. *IEEE Journal of Quantum Electronics*, 8(3):373–379, 1972.

[63] Herwig Kogelnik and Tingye Li. Laser beams and resonators. *Applied optics*, 5(10):1550–1567, 1966.

[64] Marcos A de Araújo, Rubens Silva, Emerson de Lima, Daniel P Pereira, and Paulo C de Oliveira. Measurement of gaussian laser beam radius using the knife-edge technique: improvement on data analysis. *Applied optics*, 48(2):393–396, 2009.

[65] Robert V Pound. Electronic frequency stabilization of microwave oscillators. *Review of Scientific Instruments*, 17(11):490–505, 1946.

[66] RWP Drever, John L Hall, FV Kowalski, J_ Hough, GM Ford, AJ Munley, and H Ward. Laser phase and frequency stabilization using an optical resonator. *Applied Physics B*, 31(2):97–105, 1983.

[67] Eric D Black. An introduction to pound–drever–hall laser frequency stabilization. *American journal of physics*, 69(1):79–87, 2001.

[68] Marcelo Alejandro Luda, Martin Drechsler, Christian Tomás Schmiegelow, and Jorge Codnia. Compact embedded device for lock-in measurements and experiment active control. *Review of Scientific Instruments*, 90(2):023106, 2019.

[69] Benjamin I Greene and R Wolfe. Femtosecond relaxation dynamics in magnetic garnets. *JOSA B*, 2(4):600–605, 1985.

[70] Nimai Pathak, Santosh K Gupta, Kaushik Sanyal, Mithlesh Kumar, RM Kadam, and V Natarajan. Photoluminescence and epr studies on Fe^{3+} doped $ZnAl_2O_4$: an evidence for local site swapping of Fe^{3+} and formation of inverse and normal phase. *Dalton Transactions*, 43(24):9313–9323, 2014.

[71] ZV Gareyeva and RA Doroshenko. Optical absorption of octahedral ions Fe^{2+}, Fe^{4+} and photoinduced effect in yig single crystals. *Journal of magnetism and magnetic materials*, 268(1-2):1–7, 2004.

[72] J Ma, J Dong, K-i Ueda, and AA Kaminskii. Optimization of Yb:YAG/Cr^{4+}:YAG composite ceramics passively q-switched microchip lasers. *Applied Physics B*, 105(4):749–760, 2011.

[73] Yevgeny Slobodkin, Gil Weinberg, Helmut Hörner, Kevin Pichler, Stefan Rotter, and Ori Katz. Massively degenerate coherent perfect absorber for arbitrary wavefronts. *arXiv preprint arXiv:2205.05478*, 2022.